

THERMAL TRANSPORT IN SELECTED CERAMIC MATERIALS FOR POTENTIAL
APPLICATION AS INERT MATRIX FUEL OR THERMAL BARRIER COATING USING
ATOMIC LEVEL SIMULATION

By

PRIYANK SHUKLA

A DISSERTATION PRESENTED TO THE GRADUATE SCHOOL
OF THE UNIVERSITY OF FLORIDA IN PARTIAL FULFILLMENT
OF THE REQUIREMENTS FOR THE DEGREE OF
DOCTOR OF PHILOSOPHY

UNIVERSITY OF FLORIDA

2010

© 2010 PRIYANK SHUKLA

With love to my whole family

ACKNOWLEDGMENTS

After reaching at this important milestone of my life, I would like to express my gratitude and thanks to all the people who made my PhD journey a wonderful and memorable one.

First and foremost, I would like to thank and express my deepest gratitude to my mentor Prof. Phillipot. His passion for science, willingness to help; offer advice on anything, insightful remarks and a great sense of humor made my PhD a very enjoyable learning experience. He is my role model. Without his guidance and critical remarks and constant push to bring out the best of you, this work would not have seen the day. I cannot thank enough to my supervisory committee members Prof. Sinnott, Prof. Nino, Prof. Baney and Prof. Tulenko for their constant support, suggestions and guidance.

I was fortunate enough to work with the great group of students and post docs of Computational Materials Science Focus Group. The group is very supportive and helpful. There are many, whose friendship and support, I cherished and enjoyed during these years. They know who they are and they have my gratitude. Special thanks to Dr. Rakesh Behera for his unconditional help, insightful remarks and delicious food.

This journey wouldn't have been possible without the constant support, love and encouragement from my family. Although they are physically far away, weekly phone calls, yahoo messenger and e-mails have changed the distance to a few clicks away. I consider myself fortunate to have such a great family. In the end, I would like to say my special thanks to my wife, Monika. Thanks for bearing me for past three years, when I cannot tolerate myself for more than a few minutes.

This work was funded by DOE-NERI Award DE-FC07-051D14647.

TABLE OF CONTENTS

	<u>page</u>
ACKNOWLEDGMENTS.....	4
LIST OF TABLES.....	8
LIST OF FIGURES.....	9
ABSTRACT	13
CHAPTER	
1 BACKGROUND	15
1.1 Energy Sources.....	15
1.2 Greenhouse Effect and Global Warming	17
1.2.1 Carbon Dioxide (CO ₂) Emission	19
1.2.2 Global Warming Potential.....	20
1.3 Carbon Emission-Free Energy.....	20
1.4 Nuclear Energy	23
1.5 Thermal Conductivity: An Important Property	25
1.6 Motivation for This Work	25
1.7 Objective of This Work.....	26
1.8 Organization of Dissertation.....	28
2 THERMAL TRANSPORT AND SIMULATION METHODOLOGY	29
2.1 Basics of Thermal Transport.....	29
2.2 Modes of Heat Transport	32
2.3 Heat Transport in Non-metallic Solids.....	33
2.4 Simulation Methods	39
2.5 Molecular Dynamics Basics	40
2.6 Integration Algorithms.....	40
2.7 Periodic Boundary Condition	43
2.8 Interatomic Interactions.....	45
2.8.1 Long-range Interactions.....	45
2.8.2 Short-range Interactions	51
2.9 Ensembles	54
2.9.1 Pressure Control	57
2.9.2 Temperature Control	59
2.10 Thermal Expansion Simulation	60
2.11 Thermal Conductivity Simulation	60
3 CRYSTALLOGRAPHY OF RELEVANT MATERIAL SYSTEMS.....	65
3.1 General Introduction	65

3.2	MgO: Rocksalt Crystal Structure.....	66
3.3	Nd ₂ Zr ₂ O ₇ : Pyrochlore Crystal Structure	68
3.4	MgAl ₂ O ₄ : Spinel Crystal Structure.....	71
3.5	Bi ₄ Ti ₃ O ₁₂ : Aurivillius Crystal Structure.....	75
4	THERMAL TRANSPORT PROPERTIES OF MgO-Nd ₂ Zr ₂ O ₇	84
4.1	Introduction	84
4.2	Simulation Set-ups.....	85
4.2.1	Thermal Expansion.....	85
4.2.2	Thermal Conductivity.....	85
4.3	Results.....	86
4.3.1	Thermal Expansion.....	86
4.3.2	Anharmonic Analysis.....	87
4.3.3	Thermal Conductivity.....	89
4.3.4	Finite Size Analysis	90
4.3.5	MgO: Thermal Conductivity	91
4.3.6	NDZ: Thermal Conductivity	92
4.4	MgO-NDZ: Polycrystals and Composite	93
4.4.1	Polycrystal Structure.....	94
4.4.2	Composite Structure.....	96
4.4.3	Interfacial Effect on Thermal Conductivity	98
4.4.4	Grain Size Dependence on Thermal Conductivity	102
4.4.5	Thermal Conductivity of MgO-NDZ Composite	103
4.5	Discussion	105
5	THERMAL TRANSPORT PROPERTIES OF MgAl ₂ O ₄	106
5.1	Introduction	106
5.2	Selection of Inverted Structure.....	107
5.3	Effects of Inversion on Properties	112
5.3.1	Lattice Parameter	112
5.3.2	Anti-site Formation Energy	114
5.3.3	Bulk Modulus.....	118
5.3.4	Thermal Expansion.....	122
5.3.5	Thermal Conductivity.....	125
5.4	Conclusion	132
6	THERMAL TRANSPORT PROPERTIES OF Bi ₄ Ti ₃ O ₁₂	134
6.1	Introduction: Thermal Barrier Coating.....	134
6.2	Selection of Potential Parameter	139
6.3	Thermal Expansion	140
6.4	Thermal Conductivity	146
6.5	Conclusion and Future Study.....	155
7	GENERAL CONCLUSIONS	156

7.1 MgO-NDZ	156
7.2 MgAl ₂ O ₄	157
7.3 Bi ₄ Ti ₃ O ₁₂	158
LIST OF REFERENCES	160
BIOGRAPHICAL SKETCH.....	175

LIST OF TABLES

<u>Table</u>	<u>page</u>
1-1 GWP (100 year time-horizon) of greenhouse gases	21
1-2 Types of commercial nuclear reactors.....	24
2-1 The ZBL parameters.....	53
2-2 Potential parameters for the description of MgO-Nd ₂ Zr ₂ O ₇ system	53
2-3 Short range potential parameters for MgAl ₂ O ₄	53
2-4 Short range potential parameters for Bi ₄ Ti ₃ O ₁₂	54
2-5 Summary of the eight statistical ensembles.....	57
3-1 Rocksalt AX crystal structure.....	68
3-2 Pyrochlore A ₂ B ₂ X ₆ X' crystal structure with origin at B cation.....	71
3-3 Fractional coordinates for atomic positions and vacancies for spinel	73
3-4 Various Aurivillius structures for different n values	75
3-5 Fractional coordinates for tetragonal structure (I4/mmm) of BIT.....	77
3-6 Fractional coordinates for monoclinic structure (B1a1) of BIT	77
3-7 Historical preview for structures of BIT	78
4-1 Coefficient of thermal expansion for MgO and NDZ	87
4.2 Comparison of Debye temperature and C _p	88
5-1 Comparison of thermal expansion and bulk modulus	126
6-1 Different forms of layered perovskites	137
6-2 Short range potential parameters for Bi ₄ Ti ₃ O ₁₂	139
6-3 Comparison of interaction parameters for BIT	140
6-4 Comparison of thermal expansion values.....	142
6-5 Thermal conductivity variation for all 4 systems	154

LIST OF FIGURES

<u>Figure</u>	<u>page</u>
1-1 Energy demand and supply for the US	15
1-2 Energy distribution among major sectors	16
1-3 Primary energy consumption by source and sector.....	16
1-4 Difference in average global temperature from 1961-1990	17
1-5 US greenhouse gas emission.....	18
1-6 CO ₂ concentration in the atmosphere for past 10000 years	19
1-7 Regions of restructured fuel pellet.....	27
2-1 Moore's law for microprocessor.....	29
2-2 Power consumption of a microprocessor.....	30
2-3 Schematic of TBC system	31
2-4 Three modes of Heat Transfer.....	32
2-5 Three-phonon processes.....	34
2-6 N and U processes	34
2-7 Debye temperature and thermal conductivity (in W/cm-K) at 300 K	38
2-8 Temporal and Spatial resolution of simulation methods	39
2-9 Schematic representation of a 2-D periodic system.	44
2-10 Coulomb energy per ion as a function of cut-off in NaCl	47
2-11 Energy per ion against net system charge	48
2-12 Schematic of dipolar shell of NaCl Bravais Lattice.	48
2-13 Comparison of the Coulomb energy between charged and charge neutral.....	49
2-14 Comparison between the Madelung energy and the approximate ones.....	50
2-15 Schematic of flash diffusivity measurement and temperature rise curve.	61

2-16	Schematics representation of simulation set-up for direct method	62
3-1	Conventional cubic unit cell of MgO.	66
3-2	Schematics showing three different symmetry operations.....	67
3-3	Pyrochlore sub unit (1/8) and Fluorite unit cell	69
3-4	Two types of subcells, that forms the unit cell of pyrochlore.....	70
3-5	Cubic spinel unit cell with Mg, Al and O atoms.....	72
3-6	Unit cell of $\text{Bi}_4\text{Ti}_3\text{O}_{12}$	76
3-7	Group-subgroup graph connecting $I4/mmm$ to $B1a1$	80
3-8	Octahedra tilt of 6x6x1 supercell of BIT.....	82
4-1	Simulation set-up to simulate thermal conductivity.....	86
4-2	Lattice parameter variation with temperature for MgO and NDZ	86
4-3	System size effect on thermal conductivity MgO and NDZ.....	91
4-4	Thermal conductivity data of MgO.....	92
4-5	Thermal conductivity of $\text{Nd}_2\text{Zr}_2\text{O}_7$	93
4-6	MgO polycrystal ~ 3 nm grain size	94
4-7	Different connectivity patterns for two-component composite system	96
4-8	MgO-NDZ composite (2-1 composite)	97
4-9	Comparison of thermal conductivity of MgO.....	99
4-10	Comparison of thermal conductivity of NDZ	100
4-11	Temperature dependence of the interfacial conductance, G and Kapitza length.....	101
4-12	Predicted grain-size dependence of the normalized thermal conductivity of MgO and NDZ polycrystals compared with experimental results of YSZ.....	103
4-13	Comparison of thermal conductivity of 60-40 MgO-NDZ composite with predicted value	104
5-1	Distribution of energy as a function of cation arrangement.....	108

5-2	PDF for normal spinel and comparison of Al-Mg PDF	109
5-3	Comparison of PDFs for inverted structures.....	110
5-4	Decrease of lattice parameter with inversion.....	113
5-5	Structural energy as a function of inversion for $MgAl_2O_4$	115
5-6	Cation antisite formation energy as a function of inversion.	116
5-7	Formation energy as a function of inversion site distance.	118
5-8	Bulk modulus as a function of inversion	119
5-9	Comparison of normalized bulk modulus with MD study by Chartier.....	120
5-10	Separating out various effects on bulk modulus	121
5-11	Variation of lattice parameter with temperature for $i=0$	123
5-12	Coefficient of thermal expansion as a function of inversion.....	124
5-13	Dependence of the Grüneisen coefficient on inversion.	124
5-14	Variation of thermal conductivity for $MgAl_2O_4$ with temperature	126
5-15	System size analysis for different inversion values for $MgAl_2O_4$	127
5-16	Dependence of thermal conductivity variation on inversion.....	128
5-17	Density effect on thermal conductivity	130
5-18	Combinatoric analysis	131
6-1	Simple schematic view of turbofan gas turbine engine.....	134
6-2	Idealized Brayton cycle	135
6-3	Schematic of a TBC.....	136
6-4	6x6x1 super cell of BIT viewed along x and y axes	141
6-5	Coefficient of thermal expansion of BIT along x,y and z axes	142
6-6	Temperature variation of tilt angles of	144
6-7	Temperature profile of nearest Ti-Ti distance in BIT structure.....	145
6-8	Temperature profile of Bi-Bi cation distance in Bi_2O_2 layer.....	146

6-9	System size analysis for $T = 300$ K in all the direction.....	147
6-10	Temperature and direction dependence of thermal conductivity for BIT.....	148
6-11	Thermal conductivity of BIT by experiment.....	149
6-12	Schematic of method to investigate the density effect on thermal conductivity of BIT	152
6-13	System size and density dependence of thermal conductivity for BIT	153

Abstract of Dissertation Presented to the Graduate School
of the University of Florida in Partial Fulfillment of the
Requirements for the Degree of Doctor of Philosophy

THERMAL TRANSPORT IN SELECTED CERAMIC MATERIALS FOR THEIR
POTENTIAL APPLICATION AS INERT MATRIX FUEL OR THERMAL BARRIER
COATING BY ATOMIC LEVEL SIMULATION

By

PRIYANK SHUKLA

August 2010

Chair: Simon R. Phillpot

Major: Materials Science and Engineering

Thermal management is a critical issue in nuclear reactor and thermal barrier coating applications. Current research for next-gen nuclear fuel is looking into materials to provide uranium-free alternate with high thermal conductivity, whereas thermal barrier coating research is in need of low thermal conductivity materials. In this work, an understanding of various structural factors on thermal conductivity using atomic level simulation, is presented

Thermal conductivity is a key parameter in the selection of nuclear fuel. Next gen nuclear fuel is suggested as to improve the efficiency of the nuclear fuel and make it environment friendly. Next-gen nuclear fuel is called as inert matrix fuel. Thermal conductivity of two potential materials ($\text{MgO-Nd}_2\text{Zr}_2\text{O}_7\text{:NDZ}$ and MgAl_2O_4) is characterized using molecular dynamics simulation.

In a composite system, interfaces play a dominant role in governing thermal conductivity of the system. To characterize the interface effects, very fine 2-D textured grains (<10 nm) are build. Homogeneous interface simulations showed the dominance

of interface effects on grains. Extension to bigger grain sizes showed good compatibility of the simulation data with the experimental dependence of grain size.

In addition, MgAl_2O_4 , a spinel system, has been characterized also for its potential application as an inert matrix. Since system undergoes cation anti-site inverted state under irradiation, thermal conductivity as a function of inversion is characterized. It has been shown that, thermal conductivity remains invariant under inversion. In the process of characterizing thermal conductivity, thermal expansion, bulk modulus and elastic properties are also illustrated.

Another key area for heat management is thermal barrier coating application. Thermal conductivity of a layered perovskite material, $\text{Bi}_4\text{Ti}_3\text{O}_{12}$ (BIT) belonging to Aurivillius family, is characterized. The effect of layers (Bi_2O_2 layer and perovskite layer) on the thermal transport of BIT is characterized by changing the mass of the layers under selected scenarios. The findings of the study suggested an effect of disparity between layers on the thermal conductivity of BIT in the through direction but limited role in the other directions.

CHAPTER 1 BACKGROUND

1.1 Energy Sources

Energy is the driving tool for the development of human civilization. The United States was self sufficient in energy until the 1950s. Since then, energy consumption has outpaced production, with the result that the deficit in energy continues to increase (Fig.1-1).

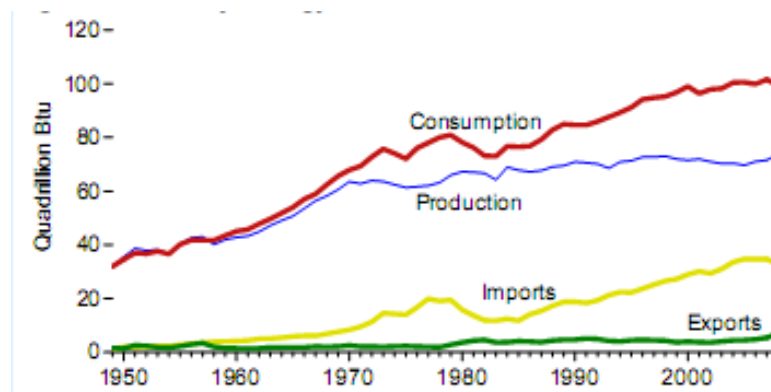


Figure 1-1. Energy demand and supply for the US [1]

Energy is given in the units of Btu, acronym for British thermal unit, which is a traditional energy unit. One Btu is the energy needed to heat up 1 pound of water by 1 degree Fahrenheit. It is approximately equivalent to 1.06 kJ. If the energy deficit continues, we will face an energy crisis in very near future. To overcome this deficit and regain energy independence, energy production needs to be increased and/or usage has to be reduced.

Figure 1-2 shows the energy consumption among various sectors. As it clearly depicts, the industrial sector has leveled off in energy consumption but all other sectors are linearly increasing. This brings us to the question: how do different energy sources contribute towards meeting our demand of energy?

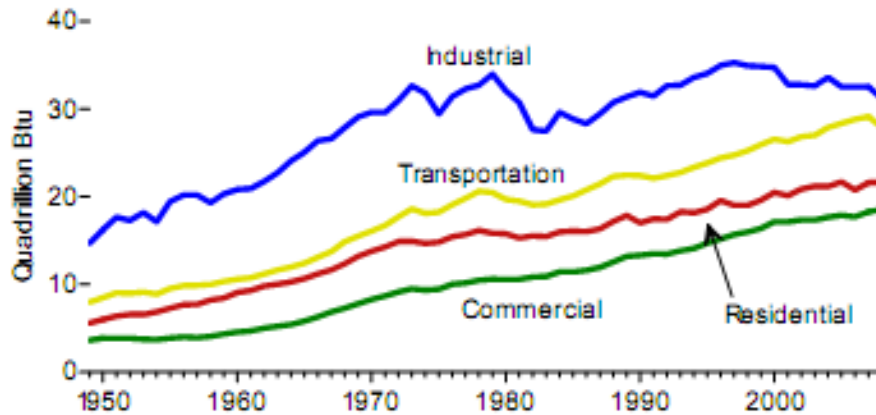
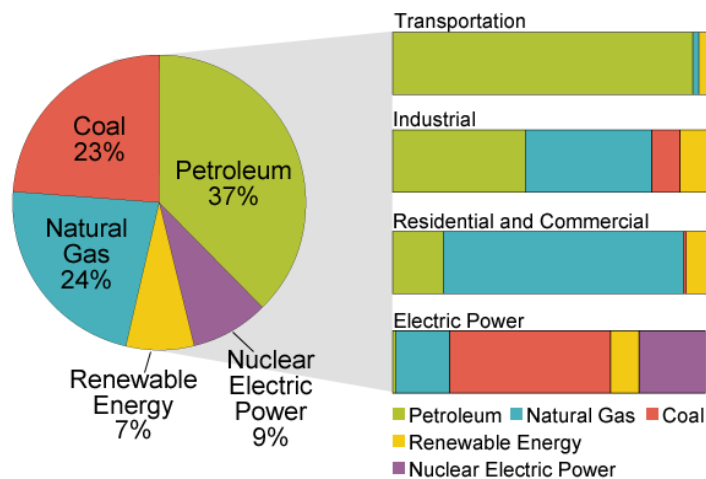


Figure 1-2. Energy distribution among major sectors [1]

The contribution from five different energy sources is shown in Fig. 1-3. It can be seen clearly that carbon-emission free energy sources (renewable and nuclear) contribute only 16% of the total share. With coal, petroleum and natural gas as the leading contributors of the energy sources the biggest concern is: what is the effect on the environment of these energy sources?



Total U.S. Energy = 99.3 Quadrillion Btu
 Source: Energy Information Administration, *Annual Energy Review 2008*, Tables 1.3, 2.1b-2.1f.

Figure 1-3. Primary energy consumption by source and sector [1]

1.2 Greenhouse Effect and Global Warming

Carbon dioxide (CO₂) is the leading contributor to the greenhouse effect and global warming. The greenhouse effect is the absorption of infrared radiation in the Earth's environment. In the total absence of greenhouse effect, the Earth's surface temperature would be 255 K instead of 288 K [2]. The "greenhouse effect" of current concern is the further rise in temperature of Earth's surface from man's activities.

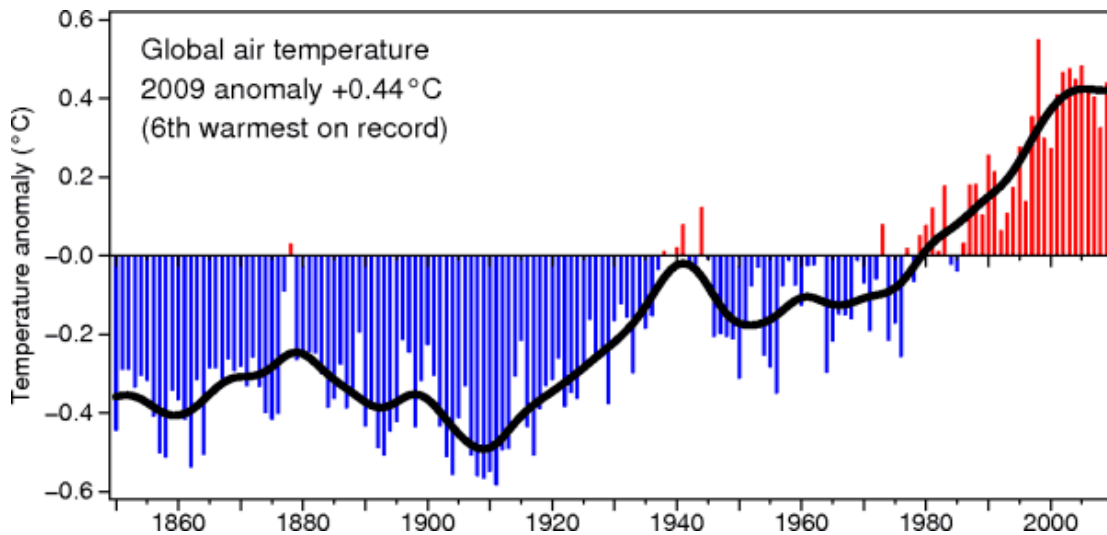


Figure 1-4. Difference in average global temperature from 1961-1990 (best coverage period) [3]

Figure 1-4 shows the trend in the Earth's surface temperature from 1850. Over 3000 stations all over the world recorded monthly temperature. The average is taken and the deviation from the period of 1961-1990 (best coverage period) is plotted here as the "Temperature anomaly". The increase over the past 30 years is the highest temperature rise seen in the past 10,000 years. To keep track of climate changes and these potential environmental and socio-economic effects, The Intergovernmental Panel on Climate Change (IPCC) was formed by the United Nations Environment Program (UNEP) and the World Meteorological Organization (WMO). In its fourth Assessment Report, it is stated that the planet is warming rapidly due to the increase in greenhouse

gases (GHGs) [4]. Gases which act in a similar fashion to CO₂ and absorb the infrared radiation from the earth's surface are collectively referred as GHGs. Although most of the GHGs are naturally present in the atmosphere, human activities have increased their levels manyfold over pre-industrial era levels. This imbalance has caused the rise in global temperature and has given birth to today's biggest challenge: Global Warming. The GHGs can be classified as three types:

1. *Natural*: CO₂, methane (CH₄), nitrous oxide (N₂O), water vapor and ozone (O₃).
2. *Man made*: Chlorofluorocarbons (CFCs), hydrochlorofluorocarbons (HCFCs), perfluorocarbons (PFCs), hydrofluorocarbons (HFCs), bromofluorocarbons (halons) and sulfur hexafluoride (SF₆).
3. *Indirect*: Carbon monoxide (CO), nitrogen oxides (NO_x), aerosols and non-methane volatile organic compounds. They influence the formation of other forms of GHGs and contribute in global warming indirectly.

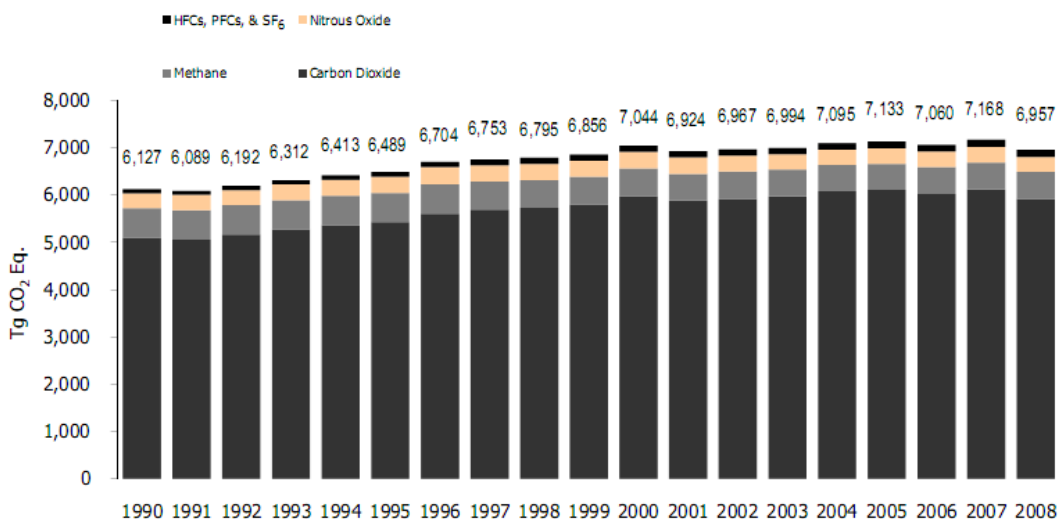


Figure 1-5. US greenhouse gas emission [5]

Even though contributions of these other GHGs are individually less than that of CO₂, their total collective contribution is of about the same magnitude. That is why their contribution in global warming is termed as “effective doubling”. Figure 1-5 captures the contribution of various GHGs since 1990.

1.2.1 Carbon Dioxide (CO₂) Emission

Being the largest contributor among GHGs, CO₂ becomes of utmost importance to understand the emission of CO₂. In the equilibrium carbon cycle there will be no buildup of CO₂ in the environment and thus no global temperature rise. Because of technical advancements, dependence on energy has increased and consequently the emission of CO₂ has risen. Figure 1-6 shows the concentration of CO₂ in the atmosphere for the past 10,000 years.

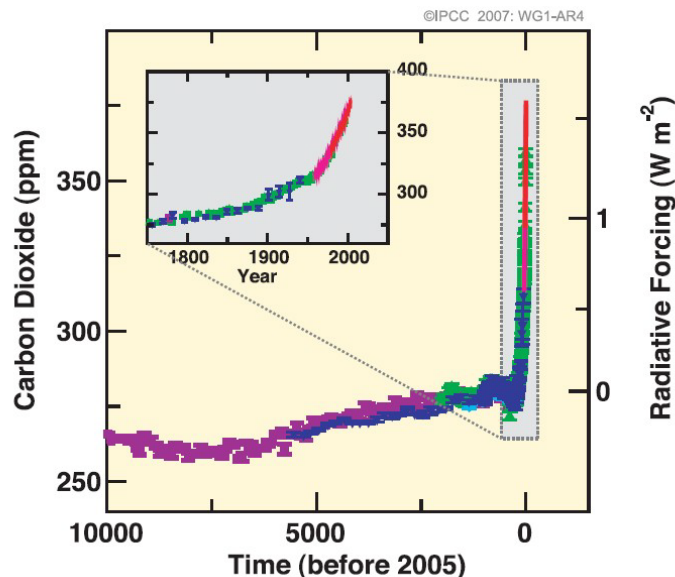


Figure 1-6. CO₂ concentration in the atmosphere for past 10000 years [6]

As shown in Fig. 1-6, the concentration of CO₂ has increased markedly since the beginning of industrialization. The right axis label of Fig. 1-6: “Radiative Forcing” is a measure of the difference in net irradiance at the boundary of troposphere and the

stratosphere. In simple terms, positive radiative forcing means a warming effect on the climate. By comparing Figs. 1-4 and 1-6, a linear relation between CO₂ emission and global temperature is found. All GHGs have different warming effects (radiative forcing) on the climate. A common metric system is used to measure the effect on climate by all these GHGs and is quantified as the global warming potential (GWP).

1.2.2 Global Warming Potential

The GWP of any GHG is a quantified measure of its global time averaged relative radiative forcing impact. Conventionally the GWP of CO₂ is taken as 1. The GWP of any gas is defined as the equivalent mass of CO₂ to produce the same effect in global warming. A GWP is always specified over a time-period. A comparison between different GHGs is shown in Table1-1.

1.3 Carbon Emission-Free Energy

In order to build a safer environment for coming generations, global warming needs to be eliminated. To achieve this goal, carbon-free energy is required. As discussed, carbon-free energy sources form a minor 16% share of the total energy resources. There are three ways to achieve the carbon-free environment:

1. Energy conservation by efficient usage
2. CO₂ separation and sequestration
3. Advancement of carbon-free energy sources (nuclear, solar, wind etc.)

Efficient usage of energy does play an important role in contributing towards carbon free environment by lowering the gap between energy demand and supply. That, in effect, lowers the consumption of fossil fuels. But in the long run, it does not alleviate the global warming problem.

Table 1-1. GWP (100 year time-horizon) of greenhouse gases [5]

Gas	Chemical formula	GWP	Atmospheric lifetime (Years)
Carbon dioxide	CO ₂	1	50-200
Methane	CH ₄	21	12 ± 3
HFC-152a	C ₂ H ₄ F ₂	140	1.5
Nitrous Oxide	N ₂ O	310	120
HFC-32	CH ₂ F ₂	650	5.6
HFC-134a	CH ₂ FCF ₃	1,300	14.6
HFC-4310mee	C ₅ H ₂ F ₁₀	1,300	17.1
HFC-125	C ₂ HF ₅	2,800	32.6
HFC-227ea	C ₃ HF ₇	2,900	36.5
HFC-143a	C ₂ H ₃ F ₃	3,800	48.3
HFC-236fa	C ₃ H ₂ F ₆	6,300	209
Perfluoromethane	CF ₄	6,500	50,000
Perfluorobutane	C ₄ F ₁₀	7,000	2,600
Perfluorohexane	C ₆ F ₁₄	7,400	3,200
Perfluoroethane	C ₂ F ₆	9,200	10,000
HFC-23	CHF ₃	11,700	264
Sulphur hexafluoride	SF ₆	23,900	3,200

CO₂ separation and sequestration has the potential to be very efficient in abating global warming problem but has serious challenges. Turner [7] compared the global warming and CO₂ separation and sequestration solution to a smoker who is exercising. Even though the smoker is exercising, it will be of no effect if he continues to smoke. Similarly, CO₂ storage and sequestration cannot be the final solution. Besides, the

sequestration process is very expensive and the risk is associated with the failure of CO₂ storage pose a great danger [7]. This limits the prospect of using CO₂ separation and sequestration technology as a solution to global warming.

That makes the third alternative to be the most attractive. A very good review of the ways to solve the current energy problem is given by Lior [8]. The following steps are suggested for the future energy solution:

1. The immediate challenge is to meet the energy demand. Thus, fossil fuel will still be used until other energy sources become large share-holders in the energy resource family.
2. CO₂ separation and sequestration methods are needed to accompany the CO₂ releasing energy sources.
3. Build more combined cycle power plants.
4. Where wind is economically available, wind power generation needs to be deployed.
5. Develop less expensive and more efficient solar cells.
6. Even with the issue of long term radioactive waste storage and safety issues, nuclear power plants need to be built and alternate nuclear fuels need to be developed.

It is evident that all carbon-free energy sources will play a vital role in resolving the energy crisis/global warming problem. Nuclear energy is clearly recognized by scientists and technologists as environment friendly [9]. This view is now also shared by some environmentalists [10]. This view is further strengthened by the fact that according to

ONU-IPCC AR4 Synthesis Report, nuclear energy is considered as an effective GHG mitigation option [1].

1.4 Nuclear Energy

Nuclear energy is a way to generate energy from the splitting of nucleus. Heavier atoms release more energy in the process of the splitting of the nucleus. Controlled fission reaction forms the basis of nuclear energy. UO_2 is the most common nuclear fuel used in nuclear plants in USA. Naturally occurring uranium contains 99.3% ^{238}U , 0.7% ^{235}U , and $< 0.01\%$ ^{234}U . ^{235}U is fissionable and most of the current reactors use enriched uranium, which contains ~4% of ^{235}U in the fuel. Fissile ^{235}U and fertile ^{238}U both are used in the fission process. Slow moving neutrons are captured by ^{235}U to start fission reaction. Whereas, fast moving neutrons are absorbed by ^{238}U and converts into ^{239}Pu , which is fissionable by slow as well as fast moving neutrons. Various kinds of nuclear reactors are used worldwide to produce the nuclear energy. Some of them are shown in Table 1-2.

As shown in Table 1-2, enriched UO_2 is the main nuclear fuel in US. The nuclear fuel cycle starts from the mining of uranium and ends at the burial of spent fuel. The whole process contributes towards radioactive waste. During mining and enrichment, waste of ^{238}U , ^{226}Ra and ^{222}Rn and ^{230}Th is generated. During the fission reaction, neutron capture and difference decay schemes leads to the formation of transuranic nuclides (atomic number >92), including ^{239}Pu , ^{237}Np , ^{241}Am and ^{244}Cm . In addition to the nuclear reactors, dismantling of nuclear warheads also increases the stockpile of Pu. The presence of these transuranic nuclides make the spent fuel radioactive and a period of more than 100,000 years is required to bring down the radioactivity level of this spent fuel to the level of mined uranium. Handling and keeping safe the Pu

stockpile and transuranic nuclides poses a great environment challenge. An innovative fuel approach, termed inert matrix fuel (uranium free), has been suggested as a way to alleviate the problem by embedding Pu and minor actinides in a material matrix of non-fissile or fertile material and incinerate in nuclear reactors. The stable matrix, after burning in a reactor will be directly disposed of in a once through fuel cycle concept.

Table 1-2. Types of commercial nuclear reactors [11]

Reactor type	Main fuel	Main countries
Pressurized Water Reactor (PWR)	Enriched UO_2	US, France, Japan, Russia, China
Boiling Water Reactor (BWR)	Enriched UO_2	US, Japan, Sweden
Pressurized Heavy Water Reactor 'CANDU' (PHWR)	Natural UO_2	Canada
Gas-cooled Reactor (AGR & Magnox)	Natural U (metal), enriched UO_2	UK
Light Water Graphite Reactor (RBMK)	Enriched UO_2	Russia
Fast Neutron Reactor	PuO_2 and UO_2 (MOX)	Japan, France, Russia

Some key parameters in the selection of the inert matrix fuel (IMF) include high temperature stability, good irradiation behavior, high thermal conductivity, good

mechanical properties, and low neutron capture and cross-sections [12, 13]. Based on these criteria, MgAl_2O_4 , $\text{ZrO}_2\text{-MgO}$ and $\text{MgO- Nd}_2\text{Zr}_2\text{O}_7$ (NDZ), among others have been suggested as possible inert matrix materials [14-16].

1.5 Thermal Conductivity: An Important Property

A nuclear fuel pellet experiences a temperature drop of ~ 800 K from the centerline of the fuel pellet to the edge. This large temperature difference is due to the low thermal conductivity of UO_2 . At high temperature, center region of the pellet expands more than the rim. Because of the thermal stress thus formed, the microstructure of the grain changes and the fuel cracks and degrades. Efficient removal of heat from the fuel will maintain a more uniform temperature across the fuel and increase the fuel life time. This makes high thermal conductivity a desirable property for a nuclear fuel. The Thermal conductivity of materials depends on various parameters including but not limited to bulk modulus, density, and microstructure.

The thermal conductivity is also an important parameter in the selection of thermal barrier coating (TBC) materials. In contrast to nuclear fuel, TBC applications demand low thermal conductivity materials. A detailed description of TBCs and their applications are given in Chapter-6.

Being important for both, nuclear fuel and TBC materials, thermal conductivity becomes an important material property for investigation. That raises an important question: *What controls thermal conductivity?*

1.6 Motivation for This Work

A good understanding of the physics governing thermal conductivity in non-metals is essential to answer the question, asked in Sec. 1.5. Phonons are the heat carriers in non-metals/ceramic materials and are defined as lattice vibrations. Analysis of thermal

transport is performed in phonon space (momentum space or frequency space). While phonon space is convenient for analysis, design and synthesis of the materials is performed in real space. It is difficult to move conceptually from phonon space to real space. For example, the position of the atoms in the unit cell and the relaxation times of the associated phonon modes are not related to each other in an obvious way. Molecular dynamics (MD) simulations are a suitable tool for the analysis of thermal conductivity at a finite temperature and for the bridging of real and phonon space analysis.

Having total control over the system, simulation provides easy access to capture the effects of structural features affecting the thermal conductivity. In the following chapters, the effects of interface, structure and mass on material's thermal transport properties are presented and analyzed in detail.

1.7 Objective of This Work

This work is primarily focused on understanding the thermoelastic properties of MgO, $\text{Nd}_2\text{Zr}_2\text{O}_7$ (NDZ), MgAl_2O_4 and $\text{Bi}_4\text{Ti}_3\text{O}_{12}$ (BIT). The thermal properties of MgO-NDZ and MgAl_2O_4 are studied in the light of their potential application as IMF systems, whereas BIT is studied for its potential application as TBC material.

The effects of interfaces on the thermal properties of MgO-NDZ system are very important to understand. During burn-up, large temperature and steeper temperature gradient causes the morphological changes of the nuclear fuel during power operation, as shown in Fig. 1-7.

Although fuel pellet starts with all solid, a sizable void develops in the center. The void forms by the movement of the porosity to the center. Immediately adjacent to void region, columnar grains are formed. The radial boundaries of the columnar grains are formed by the trails of the pores and/or by the movement of fission-gas bubbles. Moving

outward from the columnar region, a region of large textured grains is formed (Equiaxed grains) [17].

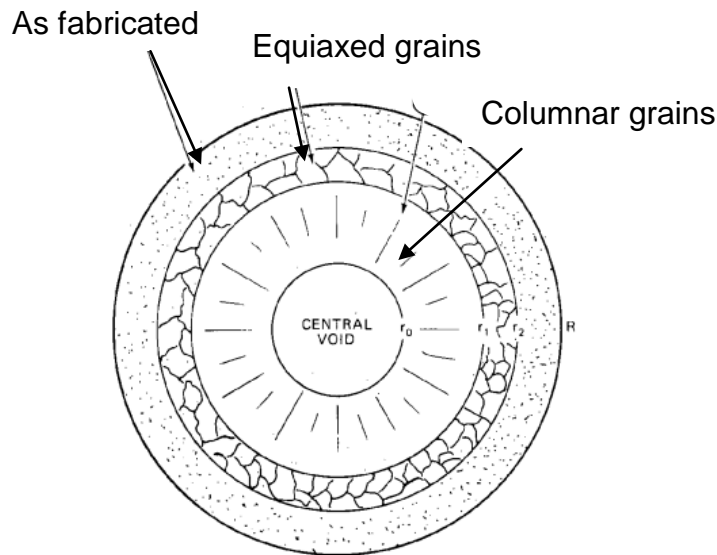


Figure 1-7. Regions of restructured fuel pellet [17]

The outermost part of the pellet experiences more radiation damage and contains more fission damage than the bulk due to neutron resonance capture by ^{238}U in this “rim” region to form fissile ^{239}Pu . This leads to the formation of smaller grain sizes ($\sim 0.2 \mu\text{m}$) from the as-fabricated grain sizes of $\sim 10 \mu\text{m}$ [18]. This effect is termed as “rim effect” and changes thermoelastic properties of the fuel. These morphological changes of the fuel, makes it essential to characterize the interface effects. Similar to experimental investigation of the interfacial effects on thermal transport for YSZ [19], MgO-NDZ composite system is investigated. To characterize the effect of interfaces for MgO-NDZ system, single crystal and polycrystals MgO and NDZ material system results are used.

Thermal and elastic properties of another candidate inert matrix material, MgAl_2O_4 are also characterized. The ability of MgAl_2O_4 to resist radiation damage comes from its

ability to withstand cation anti site disorder (inversion) without structural damage. Thus characterization of the thermal and elastic properties of MgAl_2O_4 as a function of inversion becomes very important for the potential application as an IMF matrix. In this work, effects of inversion on thermal as well as elastic properties are investigated.

Another material, $\text{Bi}_4\text{Ti}_3\text{O}_{12}$ (BIT), is characterized for its potential application as thermal barrier coating (TBC) material. The anisotropic structure of BIT is determined; Intrinsic density difference between layers has been identified as the reason of its low thermal conductivity [20]. In this work, characterization of the effect of the density difference on thermal conductivity is extended.

1.8 Organization of Dissertation

Chapter 2 lays out the foundation of thermal conductivity theory for ceramic materials and how it is implemented in molecular dynamics simulation. It covers important aspects of simulation and thermal conductivity. Chapter 3 contains crystallographic information of the materials discussed in this dissertation. Chapters 4, 5 and 6 focus on thermal transport properties of $\text{MgO-Nd}_2\text{Zr}_2\text{O}_7$, MgAl_2O_4 and $\text{Bi}_4\text{Ti}_3\text{O}_{12}$. Chapter 7 summarizes the results and the impact of this work.

CHAPTER 2
THERMAL TRANSPORT AND SIMULATION METHODOLOGY

2.1 Basics of Thermal Transport

In many aspects of technological developments, better management of heat is a key for improvement. In all sections of technology, heat flow is in the heart of many systems. Control over heat flow is necessary for the performance, life time and reliability of the devices.

Performance, reliability and life-time of electronic devices depend greatly on the efficiency of heat management. Intel co-founder Gordon Moore made the prediction in 1965 that number of transistors on a chip will double in every two years. Figure 2-1 captures the development in logic circuit industry. With each year, numbers of transistors are increasing while chip size decreases. This evolution corresponds to increasing energy density and the need for better heat management.

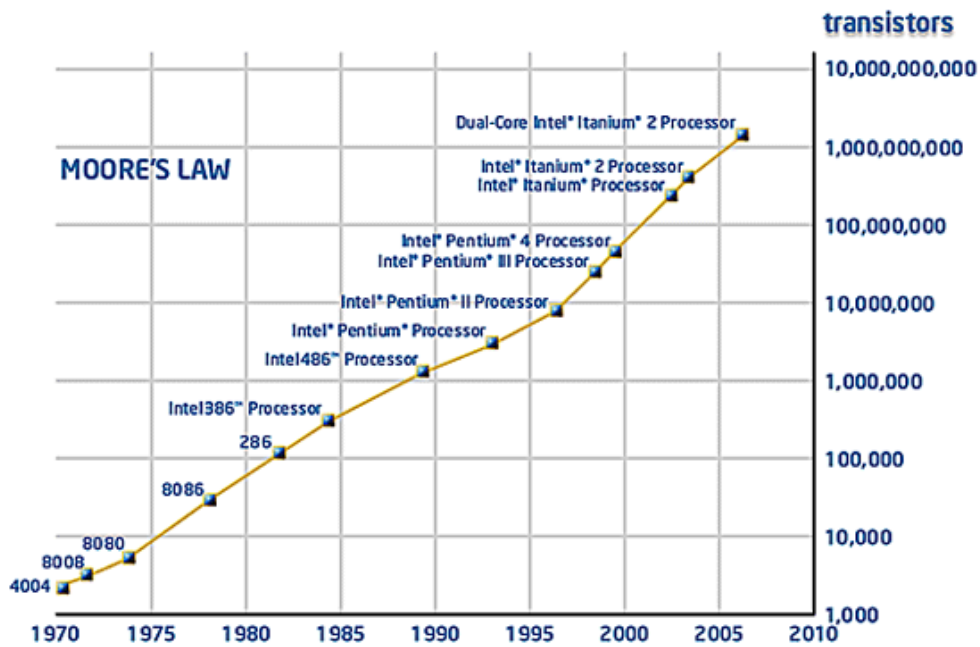


Figure 2-1. Moore's law for microprocessor [21].

The feature sizes in microelectronics is decreasing very fast and even outpacing Moore's law. Already by 2008, 35 nm Logic technology has been achieved [22]. With the increasing number of transistors on an integrated circuit and the decreasing size, power density increases. Figure 2-2 shows the implication of Moore's law on power consumption in microprocessor [23]. Figure 2-2 clearly suggests that one of the key issues is proper channeling of heat in the microprocessor.

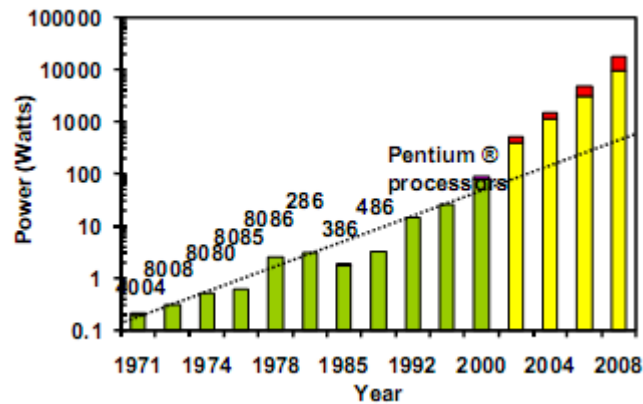


Figure 2-2. Power consumption of a microprocessor, dashed line represents Moore's Law [23]

Another area in which heat management is vital is nuclear energy. A nuclear fuel pellet experiences a temperature range of ~800 K from fuel pellet center to the rim within a distance of ~0.5 cm. Even though the heat generated during fission reaction inside the fuel is released to the coolant, this large temperature gradient often leads to structural deterioration of the fuel material. The high temperature and large temperature gradient causes physical and chemical changes in the fuel pin that often result in the deformation and cracking of the fuel pellet and possible interaction with the coolant [24]. To release heat from the fuel, higher thermal conductivity than current nuclear fuel (UO_2) is a desirable property of nuclear fuel. Therefore understanding heat transport mechanisms is important for the next generation nuclear fuel: IMF.

Heat management is critical issue for the thermal barrier coatings (TBC) also. Research is primarily focused on finding low thermal conductivity materials for the application of TBC. TBCs act as a thermal barrier between hot gas stream and engine component thus reducing thermally activated oxidation and in effect delaying failure. TBC also increases the life-time of the part by reducing thermal fatigue [25]. Figure 2-3, captures the temperature profile across the gas turbine engine and TBC.

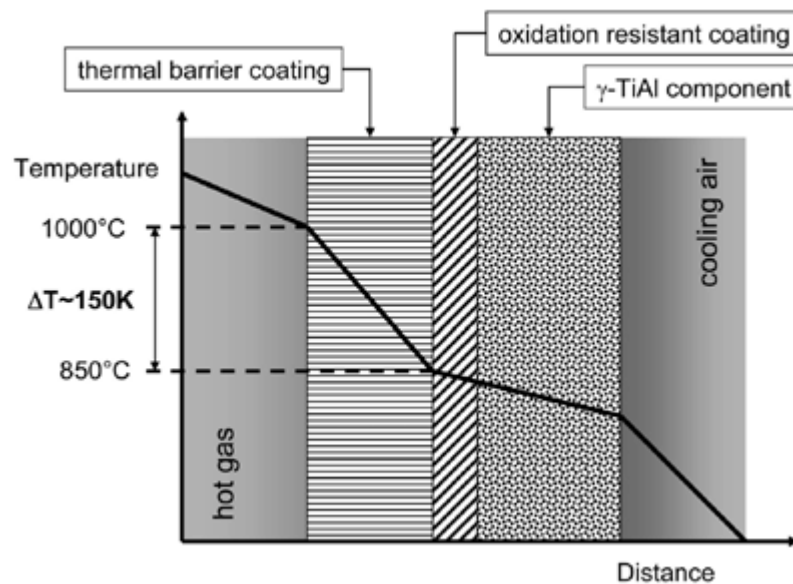


Figure 2-3. Schematic of TBC system [25]

All these examples points to the importance of heat management. A better understanding of thermal conductivity provides a greater control on materials. To capture the effects on thermal conductivity in ceramics, atomic-level simulation is used. After gaining insight into the mechanisms of thermal transport, better selection of materials will be possible. Mechanisms of heat transfer in solids and the simulation methods used to capture the heat transport mechanisms will be discussed in detail in the following sections.

2.2 Modes of Heat Transport

There are three modes of heat transfer relevant to materials: conduction, radiation and convection (Fig. 2-4). Conduction heat transfer involves heat carriers such as electrons, phonons (lattice vibrations); radiation involves electromagnetic waves and does not need any medium for heat transfer, convection involves movements of mass within fluids. Convection does not occur in solids, so this will not be discussed further.

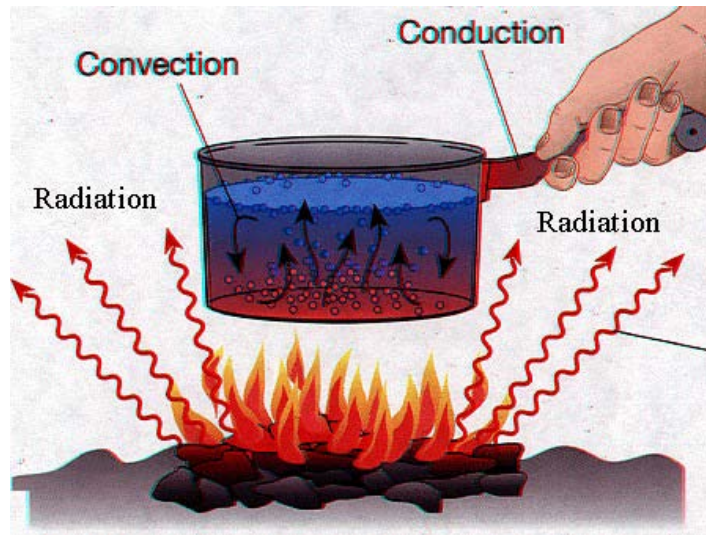


Figure 2-4. Three modes of Heat Transfer [26]

In looking at heat transfer, it is useful to place solid materials in three distinct categories: metals, semiconductors and insulators. The major heat carriers in metals are electrons. Electrons in metals are very mobile and are not held tightly by the nucleus. Thus metals are generally described as having a communal sea of valence electrons.

For metals the electrical conductivity (σ) and thermal conductivity (κ) are related by the famous Wiedemann-Franz Law [27]:

$$\frac{\kappa}{\sigma} = LT \quad (2-1)$$

T is temperature and L, a constant called the Lorentz number, is given by

$$L = \frac{\pi^2}{3} \left(\frac{k_B}{e} \right)^2 = 2.44 \times 10^{-8} \text{ W}\Omega\text{K}^{-2} \quad (2-2)$$

Where, k_B is Boltzmann constant and e is the electron charge. This empirical law states that κ/σ has same value for all the metals at the same temperature. The proportionality of κ/σ on temperature was discovered by Danish mathematician and physicist Ludvig Lorenz in 1872. While this law generally holds, L is not exactly same for all the metals. Rosenberg stated that this law holds true at low and high temperatures but fails at intermediate temperatures [28].

In semiconductors and insulators, phonons (lattice vibrations) are the major heat carriers. This mechanism will be discussed in detail in this work.

2.3 Heat Transport in Non-metallic Solids

Phonons are the major heat carriers in non-metals. The following discussion is based on standard presentations from various solid state texts [29-32].

Heat transport in non-metallic solids takes place through lattice vibrations. These are termed as phonons and are the major heat carriers in non metals. Harmonic potential treatment of phonons gives zero thermal expansion and infinite thermal conductivity of the material. Since materials do have finite value of thermal conductivity and non-zero thermal expansion, anharmonic terms are included in the discussion of phonons and heat transport. These anharmonic terms are labeled as three-phonon (3rd order term in interaction potential) and four-phonon (4th order term in potential) processes. Other higher order terms are also possible but contribution to thermal conductivity is mostly dominated by three-phonon processes. During heat transports

two kinds of three-phonon processes may occur, which are shown in Fig. 2-5 and are described below:



Figure 2-5. Three-phonon processes A) creation of one phonon from 2 phonons B) creation of two phonons from one phonon.

1. Annihilation of two phonons with the creation of one phonon (Fig. 2-5A)

$$\omega(k_1) + \omega(k_2) \rightarrow \omega(k_3), k_1 + k_2 \rightarrow k_3$$

2. Annihilation of one phonon with the creation of two phonons (Fig. 2-5B)

$$\omega(k_1) \rightarrow \omega(k_2) + \omega(k_3), k_1 \rightarrow k_2 + k_3$$

Both of the three phonon processes shown in Fig. 2.5 conserve momentum and are called normal (N) processes. In N-process, the total momentum is conserved and thus the phonon distribution is not changed. Another three phonon process is also possible in which momentum is not conserved, as shown in Fig. 2-6.

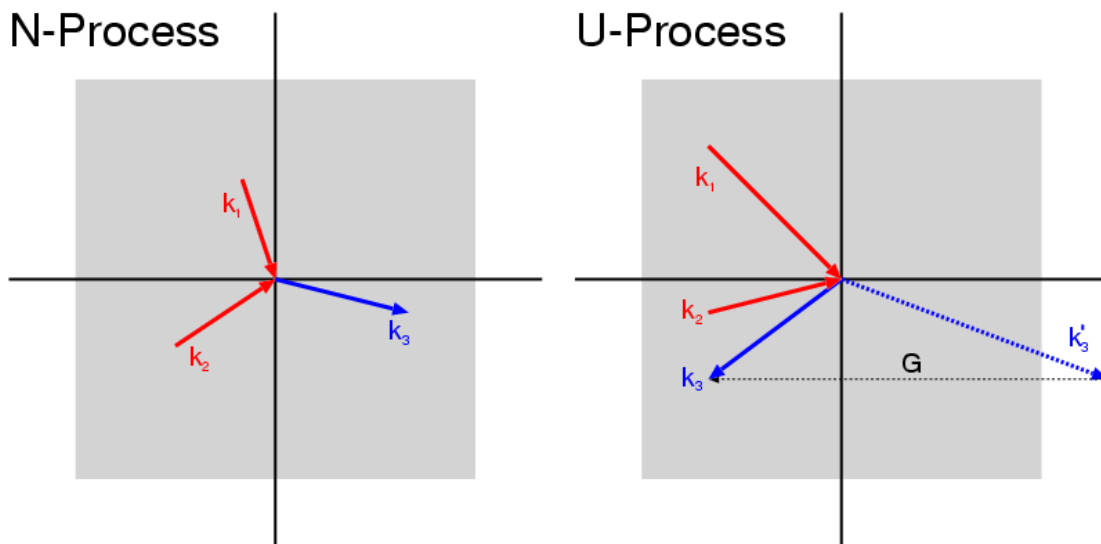


Figure 2-6. N and U processes, k_1 , k_2 , k_3 , and k_3' represent phonon-momenta and G reciprocal vector [33]

Figure 2-6 shows both the N and U processes. G is a reciprocal lattice vector and based on the value of G , two processes are possible: normal (N) for $G=0$ and umklapp (U) for $G \neq 0$. The shaded region in Fig. 2-6 is first Brillouin zone. In the N-process, as expected phonon momenta lies in the first Brillouin zone and so no further operation is needed. U-processes do need an additional operation of the addition of reciprocal vector G to bring back the phonon momenta to first Brillouin zone. The N-processes contribute to thermal conductivity indirectly as explained in detail by Callaway [34]. The dominant contribution to the heat resistance comes from U-processes, *i.e.* momentum non-conserving processes. There are a number of theoretical approaches to understand phonon conductivity in solids, including:

1. Relaxation time approach
2. Variational approach
3. Green's function approach (density matrix approach)

The relaxation time and variation approaches assume that the thermal conductivity can be calculated from the linearized Boltzmann equation, whereas the Green's function approach takes the route of quantum statistics. A very good discussion of these methods is given by Srivastava [32]. From the kinetic theory of gases, the thermal conductivity of phonon gas can be expressed as

$$\kappa = \frac{1}{3} C v \lambda \quad (2-3)$$

where C is the specific heat, v is group velocity and λ is mean free path of the phonons. In a phonon gas, C can be approximated well by using the Debye model, v can be taken as the speed of sound; the real problem is in the calculation of λ .

The specific heat is defined by the amount of heat required to raise the temperature by 1 K per unit mass. It is one of the easiest thermodynamic quantities to measure experimentally. Depending on which system parameter is kept constant, the specific heat can be of two types: C_p for constant pressure and C_v for constant volume. Since for a solid, it is experimentally unrealistic to keep volume constant while changing temperature, C_p is of more experimental relevance. There is a simple relationship between C_v and C_p for solids [35]:

$$C_p = C_v + TV \frac{\alpha^2}{K_T} \quad (2-4)$$

where α is coefficient of thermal expansion and K_T is isothermal compressibility. At high temperatures, all solids obey Dulong-Petit result for the heat capacity, which gives the value as:

$$C_v = 3N_A k_B \quad (2-5)$$

where N_A is Avogadro's number and k_B is the Boltzmann constant. This gives fairly good value at high temperatures but is qualitatively incorrect at lower temperatures; in particular $T = 0$ K, the specific heat value goes to zero.

Einstein proposed a crude but simple approximation that all vibrations have the same frequency and are set to the value ω_E . The heat capacity then can be given as:

$$C_v = 3NZk_B \left(\frac{\hbar\omega_E}{k_B T} \right)^2 \frac{\exp(\hbar\omega_E/k_B T)}{[\exp(\hbar\omega_E/k_B T) - 1]^2} \quad (2-6)$$

Equation 2-6 is known as the Einstein model for heat capacity. It correctly converges to zero at 0 K but gives the wrong temperature dependence, decreasing faster than experiment near 0 K. Debye proposed a model in 1912 that overcame the problem of the Einstein model. Debye approximated a linear relation for phonon

frequencies $\omega = ck$ and treated phonons in a similar fashion as a particle in a box. Instead of infinite possible values of ω , Debye suggested an upper limit on frequency as ω_D . Density of states under the Debye approximation is defined as:

$$D(\omega) = \begin{cases} \frac{V\omega^2}{2\pi^2v^3}, & \omega < \omega_D \\ 0 & \omega > \omega_D \end{cases} \quad (2-7)$$

where V is the volume of the solid. The maximum frequency ω_D is determined by the number density of atoms n and given as:

$$\omega_D = 2\pi^2v^3n \quad (2-8)$$

The specific heat in Debye model is given as:

$$C_V = 3N \int_0^{\omega_D} 3\hbar \left(\frac{\omega}{\omega_D} \right)^3 \frac{\partial n(\omega, T)}{\partial T} d\omega \quad (2-9)$$

At low temperatures, Eq. 2-9 become $C_V = \frac{12\pi^4 Nk_B}{5} \left(\frac{T}{\Theta_D} \right)^3$, where Θ_D is Debye temperature, defined as $\Theta_D = \frac{\hbar\omega_D}{k_B} = \frac{c\hbar}{k_B} \left(\frac{6\pi^2 N}{V} \right)^{1/3}$. At high temperatures, it reaches the Dulong-Petit limit of $3N_Ak_B$.

The Debye temperature is the temperature above which material behaves classically and quantum effects to thermal conduction are negligible. As explained above, Debye model imposes a condition as maximum allowable phonon frequency to achieve finite number of modes in a solid (Eq. 2-8). That maximum frequency corresponds to the Debye temperature. Figure 2-7 shows the Debye temperature for various materials. The simplicity or complexity of Eq. 2-3 lies in the understanding of phonon mean free path. Based on the phonon model (Debye or Einstein), the

temperature dependence of thermal conductivity can be easily described. At high temperatures, the specific heat of a solid is a constant, given by the Dulong-Petit law (Eq. 2-5). The group velocity of phonons in a solid has a weak temperature dependence [36]. Although the exact solution is not known, Peierls showed phonon mean free path has $\frac{1}{T}$ dependence at high temperatures [37]. More sophisticated analysis has shown that temperature dependence is not $\frac{1}{T}$ but $\frac{1}{T^n}$, where n lies between 1 and 2 and confirmed by experiments [29, 38].

Li		Be		Debye temperature and thermal conductivity										B	C	N	O	F	Ne	
344		1440		Low temperature limit of Debye temperature in Kelvin										...	2230	75
0.85		2.00		Thermal conductivity at 300K, in W/cmK										0.27	1.29	
Na		Mg		...										Al	Si	P	S	Cl	Ar	
158		400		...										428	645	92	
1.41		1.56		...										2.37	1.48	
K	Ca	Sc	Ti	V	Cr	Mn	Fe	Co	Ni	Cu	Zn	Ga	Ge	As	Se	Br	Kr			
91	230	360	420	380	630	410	470	445	450	343	327	320	374	282	90	...	72			
1.02	...	0.16	0.22	0.31	0.94	0.08	0.80	1.00	0.91	4.01	1.16	0.41	0.6	0.50	0.02			
Rb	Sr	Y	Zr	Nb	Mo	Tc	Ru	Rh	Pd	Ag	Cd	In	Sn	Sb	Te	I	Xe			
56	147	280	291	275	450	...	600	480	274	225	209	108	200	211	153	...	64			
0.58	...	0.17	0.23	0.54	1.38	0.51	1.17	1.50	0.72	4.29	0.97	0.82	0.67	0.24	0.02			
Cs	Ba	La	Hf	Ta	W	Re	Os	Ir	Pt	Au	Hg	Tl	Pb	Bi	Po	At	Rn			
38	110	142	252	240	400	430	500	420	240	165	71.9	78.5	105	119	64			
0.36	...	0.14	0.23	0.58	1.74	0.48	0.88	1.47	0.72	3.17	...	0.46	0.35	0.08			
Fr	Ra	Ac	...																	
...																	
...																	
...			Ce	Pr	Nd	Pm	Sm	Eu	Gd	Tb	Dy	Ho	Er	Tm	Yb	Lu	...			
...			200	...	210	120	210	...			
...			0.11	0.13	0.16	...	0.13	...	0.11	0.11	0.11	0.16	0.14	0.17	0.35	0.16	...			
...			Th	Pa	U	Np	Pu	Am	Cm	Bk	Cf	Es	Fm	Md	No	Lr	...			
...			163	...	207			
...			0.54	...	0.28	0.06	0.07			

Figure 2-7. Debye temperature and thermal conductivity (in W/cm-K) at 300 K for selected elements [30]

At low temperatures, the phonon mean free path becomes extremely long and thermal conductivity is limited by the system size, because scattering is dominated by the surfaces. In low temperature limit, the temperature dependence of thermal conductivity comes from the specific heat. Because the specific heat shows T^3

dependence, the thermal conductivity does also. In the intermediate temperature range,

Peierls showed $\kappa \sim \left(\frac{T}{\Theta_D}\right)^n \exp\left(\frac{\Theta_D}{bT}\right)$, where n, and b can be determined by fitting to

experimental results. Typical values of nb lie in the range of 15-35.

2.4 Simulation Methods

There are number of ways to simulate materials. Based on the desired properties, an appropriate simulation method can be selected based on the length and time scale. Figure 2-8 captures different simulation methods based on time and length scales.

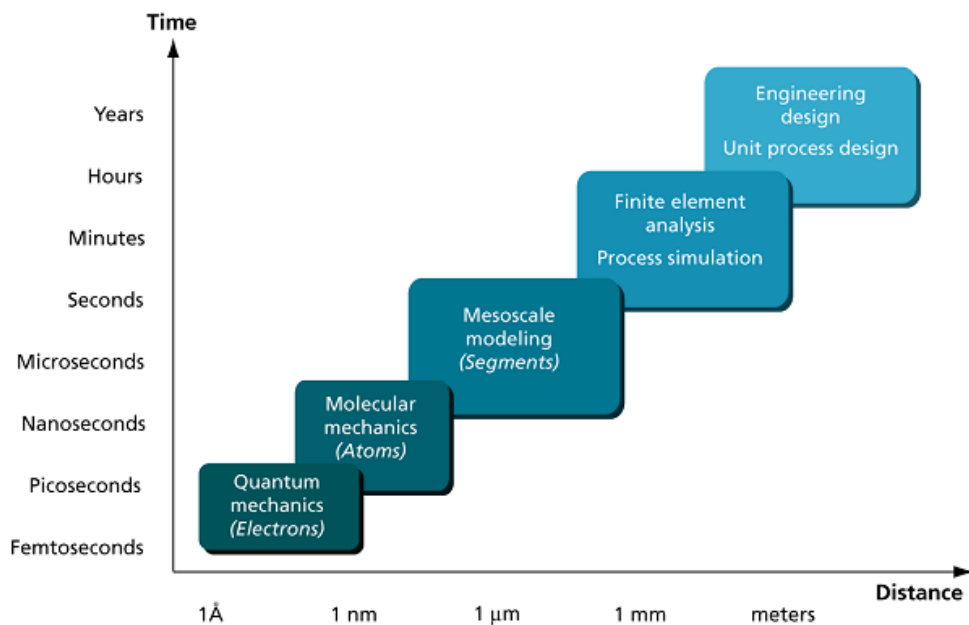


Figure 2-8. Temporal and Spatial resolution of simulation methods [39]

For example, to investigate the electronic structure of a material, quantum mechanical simulation methods (density functional theory and Hartree-Fock) are appropriate [40]; to simulate a material of the size of mm, finite element methods are appropriate [41]. With current technological improvements, μm size length system have been simulated using molecular dynamics (MD) simulation with trillion atoms [42]. In this

case the limiting factor is the huge amount of data and its analysis and the possible time devotion for the simulation. A 10 ps MD simulation of trillion atoms took a couple of days to finish and 40 TB hard disk space to store position, velocity and force data [42].

MD simulation is deterministic in nature and is a useful tool in the study of non-equilibrium processes at the atomic level. Atoms are the basic units of MD simulation and are generally treated as having no internal electronic structure. Each atom has a specified mass and charge. It is classical in nature and every atom follows Newton's equation of motion (Eq. 2-10).

$$\vec{F} = m \frac{d^2 \vec{r}}{dt^2} \quad (2-10)$$

The key physical input required for MD simulations is the interatomic potential. Since there is no interatomic potential that can exactly describe all the properties of any material, MD simulations can capture the properties of material only with limited fidelity.

2.5 Molecular Dynamics Basics

As explained in the previous section, the trajectory of each atom is calculated in MD simulation using Newton's equation of motion. Based on the trajectory as a function of time, the average values of properties can be determined. For any atom i , the equation of motion can be written as follows:

$$F_i = m_i \frac{d^2 r_i}{dt^2} = -\nabla U_i \quad (2-11)$$

2.6 Integration Algorithms

There are various integration algorithms [43, 44]. All the algorithms expand the position (r), velocity (v) and acceleration (a) into Taylor series around the time t :

$$\begin{aligned}
 r(t + \delta t) &= r(t) + v(t)\delta t + \frac{1}{2} \ddot{r}(t)\delta t^2 + \dots \\
 v(t + \delta t) &= v(t) + a(t)\delta t + \frac{1}{2} \ddot{v}(t)\delta t^2 + \dots
 \end{aligned}
 \tag{2-12}$$

$$a(t + \delta t) = a(t) + \dot{a}(t)\delta t + \dots$$

The Verlet Algorithm: The Verlet algorithm uses position and acceleration at time t and $t - \delta t$ to calculate position at $t + \delta t$ [45]. Because of its simplicity and low memory usage, it is a very common algorithm. According to Verlet algorithm, the position at $t + \delta t$ is given by

$$r(t + \delta t) = 2r(t) - r(t - \delta t) + a(t)\delta t^2 \tag{2-13}$$

The Leap-Frog Algorithm: The leap-frog algorithm is a modified version of Verlet algorithm. It computes velocities at half time-step intervals and uses these velocities to calculate positions at time $t + \delta t$

$$r(t + \delta t) = r(t) + v\left(t + \frac{\delta t}{2}\right)\delta t \tag{2-14}$$

The Beeman's Algorithm: The position prediction is similar to the Verlet algorithm but velocities are determined more precisely.

$$\begin{aligned}
 r(t + \delta t) &= r(t) + v(t)\delta t + \frac{2}{3}a(t)\delta t^2 - \frac{1}{6}a(t - \delta t)\delta t^2 \\
 v(t + \delta t) &= v(t) + \frac{1}{3}a(t + \delta t)\delta t + \frac{5}{6}a(t)\delta t - \frac{1}{6}a(t - \delta t)\delta t
 \end{aligned}
 \tag{2-15}$$

The Predictor-Corrector Algorithm: The Beeman's algorithm is modified into the predictor-corrector algorithm.

$$\begin{aligned}
\vec{r}(t + \delta t)_{predicted} &= \vec{r}(t) + \vec{v}(t)\delta t + \frac{2}{3}\vec{a}(t)\delta t^2 - \frac{1}{6}\vec{a}(t - \delta t)\delta t^2 \\
\vec{v}(t + \delta t)_{predicted} &= \vec{v}(t) + \frac{3}{2}\vec{a}(t)\delta t - \frac{1}{2}\vec{a}(t - \delta t)\delta t \\
\vec{v}(t + \delta t)_{corrected} &= \vec{v}(t) + \frac{1}{3}\vec{a}(t + \delta t)\delta t + \frac{5}{6}\vec{a}(t)\delta t - \frac{1}{6}\vec{a}(t - \delta t)\delta t
\end{aligned} \tag{2-16}$$

The 5th order Gear predictor-corrector method [44] is used in this work for numerical integration. The predicted new position of an atom is calculated using 5th order derivative of current position.

$$\begin{aligned}
\vec{r}^p(t + \delta t) &= \vec{r}(t) + \delta t \vec{v}(t) + \frac{1}{2} \delta t^2 \vec{a}(t) + \frac{1}{6} \delta t^3 \vec{b}(t) + \frac{1}{24} \delta t^4 \vec{c}(t) + \frac{1}{120} \delta t^5 \vec{d}(t) \\
\vec{v}^p(t + \delta t) &= \vec{v}(t) + \delta t \vec{a}(t) + \frac{1}{2} \delta t^2 \vec{b}(t) + \frac{1}{6} \delta t^3 \vec{c}(t) + \frac{1}{24} \delta t^4 \vec{d}(t) \\
\vec{a}^p(t + \delta t) &= \vec{a}(t) + \delta t \vec{b}(t) + \frac{1}{2} \delta t^2 \vec{c}(t) + \frac{1}{6} \delta t^3 \vec{d}(t) \\
\vec{b}^p(t + \delta t) &= \vec{b}(t) + \delta t \vec{c}(t) + \frac{1}{2} \delta t^2 \vec{d}(t) \\
\vec{c}^p(t + \delta t) &= \vec{c}(t) + \delta t \vec{d}(t) \\
\vec{d}^p(t + \delta t) &= \vec{d}(t)
\end{aligned} \tag{2-17}$$

Where \vec{r} , \vec{v} , and \vec{a} are the position, velocity, acceleration of each atom respectively. \vec{b} , \vec{c} and \vec{d} are third, fourth and fifth derivatives of the position with time of each atom respectively. The superscript 'p' corresponds to the 'predicted' values.

Using these predicted positions, forces on atoms are calculated thence the corrected accelerations. The difference between the corrected and predicted acceleration gives the error from the prediction step that is used to calculate the trajectory:

$$\Delta \vec{a}(t + \delta t) = \vec{a}^c(t + \delta t) - \vec{a}^p(t + \delta t) \tag{2-18}$$

$$\begin{aligned}
\vec{r}^c(t + \delta t) &= \vec{r}^p(t + \delta t) + c_0 \Delta \vec{a}(t + \delta t) \\
\vec{v}^c(t + \delta t) &= \vec{v}^p(t + \delta t) + c_1 \Delta \vec{a}(t + \delta t) \\
\vec{a}^c(t + \delta t) &= \vec{a}^p(t + \delta t) + c_2 \Delta \vec{a}(t + \delta t) \\
\vec{b}^c(t + \delta t) &= \vec{b}^p(t + \delta t) + c_3 \Delta \vec{a}(t + \delta t) \\
\vec{c}^c(t + \delta t) &= \vec{c}^p(t + \delta t) + c_4 \Delta \vec{a}(t + \delta t) \\
\vec{d}^c(t + \delta t) &= \vec{d}^p(t + \delta t) + c_5 \Delta \vec{a}(t + \delta t)
\end{aligned} \tag{2-19}$$

The coefficients for a fifth order predictor-corrector are $c_0 = 3/16$, $c_1 = 251/360$, $c_2 = 1$, $c_3 = 11/18$, $c_4 = 1/6$, and $c_5 = 1/60$ [44, 46]. These corrected values are used as an input for the next simulation step. The procedure is repeated for all the atoms to determine their trajectories for the duration of the simulation.

The time-step is an important factor in sampling the atom trajectory during simulation. The time step must be smaller than the fastest vibrational frequency in the system. Typical time steps for MD simulations are of the order of 1fs (10^{-15} s). This constraint comes from the fact that higher time step leads to errors in the trajectory and unreliable simulation results. Smaller time steps might capture more accurate trajectory but will limit the total simulation time. There are several ways developed to increase the time step and maintain the accuracy level, e.g. multiple time scale [47, 48] and stochastic dynamics [49].

2.7 Periodic Boundary Condition

The application of periodic boundary conditions (PBC) is a very useful technique to mimic large system by simulating smaller systems. Depending upon the requirements, PBC can be applied to replicate the system in one, two or three dimensions. When applied in three dimensions, the system is extended to mimic bulk material. A schematic of PBC is shown in Fig. 2-9. Original simulation cell (cell # 5) is in the center of the

simulation system and other 8 cells surrounding it are the outcome of PBC. Arrows represent the movement of atoms.

During simulation, all the image cells follow the actual cell. Therefore, during simulation if any atom moves in the actual cell, its periodic images follow its motion. For example, if atom moves from cell 5 to cell 6. All its images, also move to the next cell and in this process, atom from cell 4 enters cell 5. That way the total numbers of atoms in the cell are always conserved.

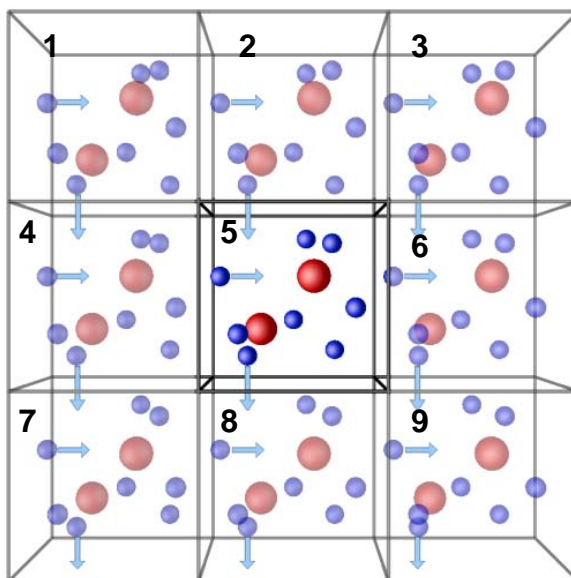


Figure 2-9. Schematic representation of a 2-D periodic system. Simulation is performed with the highlighted box. Arrows shows how atoms are affected under PBC [50]

When PBC is applied, one needs to be careful as it can lead to unphysical interactions (self interaction: between atom and its image). All the interactions are taken to be zero after a specified distance (known as cut-off). Typically, to avoid self interactions, system size needs to be at least twice the cut off.

2.8 Interatomic Interactions

Newton's equation of motion forms the basis of MD simulation and the interaction potential is the most important input for MD simulation. The quality of any simulation depends merely on the quality of the interatomic potential. In ionic systems, atoms are made of charged ions and interactions between the ions can be separated into a long range, Coulombic part, and a short range part.

2.8.1 Long-range Interactions

The long-range interaction between two charged species is given by Coulomb's law:

$$U_{Coul} = \frac{q_i q_j}{r_{ij}} \quad (2-20)$$

Where, q_i and q_j are the charges on atom i and j respectively, and r_{ij} is the distance between them. For a crystal structure with N ions, the total Coulombic energy is

$$U_{Coul} = \sum_{i=1}^{N-1} \sum_{j>i}^N \frac{q_i q_j}{r_{ij}} \quad (2-21)$$

The $1/r$ dependence of the energy makes the summation conditionally convergent. Conventionally, the Ewald summation is used to compute the long-range electrostatic interactions [51]. A more recent direct summation method is used to compute the summation [52]. Both methods are described below.

Ewald Sum: The Ewald method is the standard technique to calculate electrostatic interaction in a periodic system. It was introduced by P. Ewald in 1921 [51]. In this technique, Eq. 2-19 is rewritten as two rapidly converging parts plus a constant term.

$$U_{Ewald} = U^r + U^m + U^0 \quad (2-22)$$

Where U^r is the short range term that sums quickly in real space, U^m is a long range term that sums quickly in reciprocal (Fourier) space and U^0 is the constant (self) term. These terms are given as:

$$\begin{aligned}
 U^r &= \frac{1}{2} \sum_{i,j}^N q_i q_j \frac{\text{erfc}(\alpha r_{ij})}{r_{ij}} \\
 U^m &= \frac{1}{2\pi V} \sum_{i,j}^N q_i q_j \sum_{m \neq 0} \frac{\exp\left(-\left(\frac{\pi m}{\alpha}\right)^2 + i2\pi m \cdot (r_i - r_j)\right)}{m^2} \\
 U^0 &= \frac{-\alpha}{\sqrt{\pi}} \sum_{i=1}^N q_i^2
 \end{aligned} \tag{2-23}$$

V is the volume of the simulation cell, $m = (l,j,k)$ is a reciprocal-space vector. There are a few disadvantages of the Ewald sum. Firstly, it is not straightforward and fairly complicated to code, secondly it scales as $O(N^{3/2})$ [53].

Direct Sum: A powerful alternative to the Ewald summation was developed by Wolf *et al.* [52] and is referred to as the direct summation. It is inspired by the fact that the Coulombic interactions in ionic crystals are short ranged, as demonstrated by both, theories [30, 54] and simulations [55, 56]. The only factor not allowing Coulomb sum to converge is the lack of charge neutrality over spherical crystal-lattice shell. This can be best illustrated with the help of an example. Consider a simple rocksalt structure of NaCl. The NaCl unit cell can be viewed as interpenetrating FCC lattices of anions and cations with half unit cell length displacement. The rocksalt structure will be discussed in detail in Chapter 3. As different cut-off distances are set for the potentials (cut-off distance is defined as the distance beyond which atoms do not interact Eq 2-26), the total system will be either cation deficient or anion deficient or rarely charge neutral. Figure 2-10 shows the variation of energy with cut-off radius.

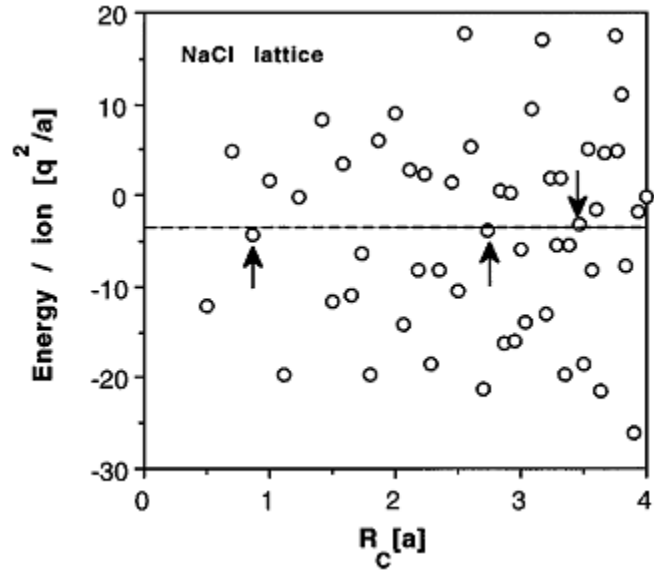


Figure 2-10. Coulomb energy per ion as a function of cut-off in NaCl [52]

Figure 2-10 straightforwardly captures the non-convergence of the Coulomb energy. The dashed line in the Fig. 2-10 is the actual value of the Coulomb energy for $R_c \rightarrow \infty$ of NaCl which is also known as the Madelung energy. The arrow in the Fig. 2-10 shows the points where the energy value converges to the actual value, however no relationship can be deduced between the cut-off (R_c) and convergence. When the same energy graph is viewed against the net system charge (Fig. 2-11), a clear trend is captured for the convergence. Figure 2-11 renders the convergence criterion: charge neutral system. Fluctuations in Fig. 2-10 around the dashed line show that NaCl system never achieves charge neutrality when it is spherically terminated.

To overcome this charge neutrality problem, initially a dipolar solution was suggested by Wolf [57]. A schematic is shown in Fig. 2-12, where a NaCl crystal is built of $\text{Na}^+\text{-Cl}^-$ dipoles. In the evaluation of the Coulomb energy for a truncated crystal shell, counter dipoles are created at the surface for each dipole present in the shell and the expression for the Coulomb energy is given below:

$$E = \left(\frac{7q^2}{8b} \right) \sum_{r_s} N(r_s) \left(\frac{b}{r_s} \right)^5 \left(1 - 5 \langle \cos^4 \vartheta \rangle_{r_s} \right) \quad (2-24)$$

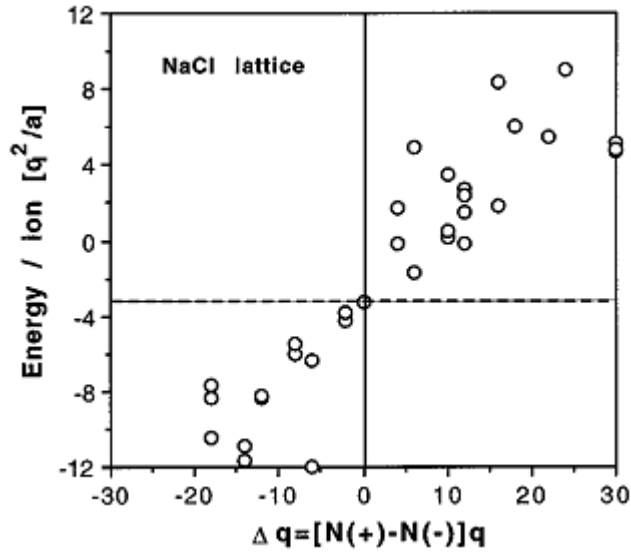


Figure 2-11. Energy per ion against net system charge [52]

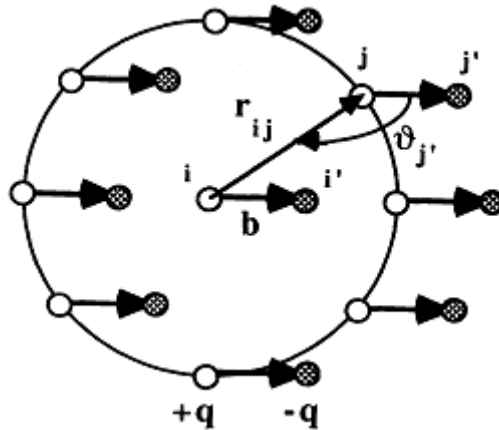


Figure 2-12. Schematic of dipolar shell of NaCl Bravais Lattice. Adapted from Ref. [57]

This dipole approach solves the problem of charge neutrality but leaves the system polarized. To overcome the polarization effect in the energy calculation, the polarization energy per unit volume is subtracted to achieve the correct Coulomb energy

value. The whole problem of polarization energy can be avoided altogether, if the basic unit is taken without a dipole moment. For the NaCl crystal system, instead of $\text{Na}^+\text{-Cl}^-$ as a basic unit, a sub-unit cell consisting of 4 Na^+ and 4 Cl^- ions, is taken as a basis. Charge neutrality is achieved by adding countercharges at the terminated sphere. If $\Delta q(R_c)$ is the net charge within the cutoff sphere of radius R_c for ion i , the Coulomb energy can be written as:

$$E_i^{Mad}(R_c) \approx \sum_{\substack{i \neq j \\ (r_{ij} < R_c)}} \frac{q_i q_j}{r_{ij}} - \frac{q_i \Delta q(R_c)}{R_c} \quad (2-25)$$

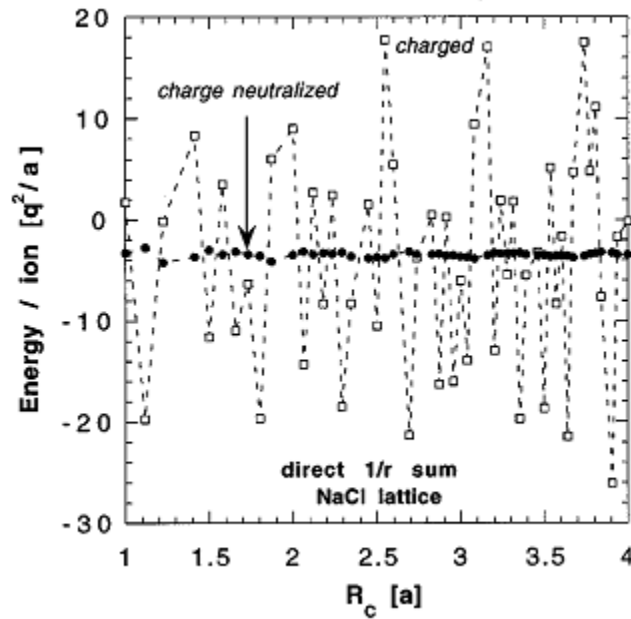


Figure 2-13. Comparison of the Coulomb energy between charged (open circle) and charge neutral (filled circle) systems as a function of R_c . Adapted from reference [52]

A comparison between the charge neutral crystal shell and charged one is shown in Fig. 2-13. Figure 2-13 shows the effect of charge neutrality on the energy calculation and all the fluctuations of the charged system go away. Comparison with real Madelung energy is shown in Fig. 2-14 and it shows a damping effect in the energy calculation by

the direct sum. Energy converges by $1/r$ in the direct sum as seen in Fig. 2-14. This $1/r$ damping effect on energy makes the potential practically very slow and useless for practical uses. That calls for some improvement in the potential.

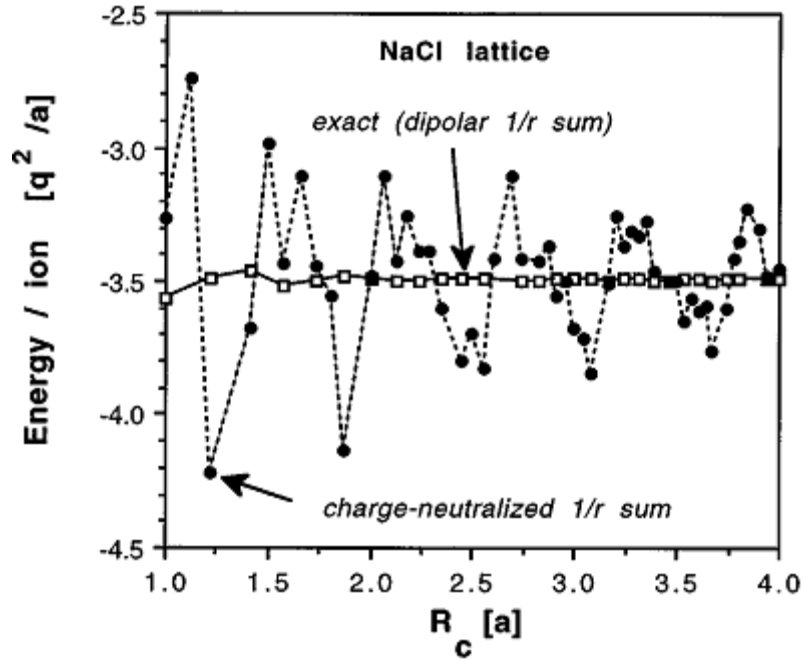


Figure 2-14. Comparison between the Madelung energy (open square) and the approximate ones (filled circle) as a function of R_c . Adapted from reference [52]

Before suggesting improvement to iron out the damping effect in energy, potential energy in itself needs to be rectified for the direct sum. By terminating energy calculation at R_c , forces and stresses beyond R_c become zero, which makes these otherwise physically continuous functions, discontinuous. To retain the continuity of energy, forces and stress, a shifted potential is used instead of the actual potential. Form of this shifted potential is given in Eq. 2-26.

$$V_{sh}^C(r_{ij}) = \frac{q_i q_j}{r_{ij}} - \lim_{r_{ij} \rightarrow R_c} \left\{ \frac{q_i q_j}{r_{ij}} \right\}$$

(2-26)

By introducing damping term in the shifted potential (Eq. 2-26), fluctuations in the Madelung energy calculation can be flattened out at smaller R_c . Damping is introduced in the potential by error function because of its i) simplicity and ii) similarity to the Ewald summation method. After all these modifications, Eq. 2-22 is expressed as follows:

$$E_{toi}^{Mad}(R_c) \approx \frac{1}{2} \sum_{i=1}^N \sum_{\substack{j \\ (i \neq j \\ r_{ij} < R_c)}} \left(\frac{q_i q_j \operatorname{erfc}(\alpha r_{ij})}{r_{ij}} - \lim_{r_{ij} \rightarrow R_c} \left\{ \frac{q_i q_j \operatorname{erfc}(\alpha r_{ij})}{r_{ij}} \right\} \right) - \left(\frac{\operatorname{erfc}(\alpha R_c)}{2R_c} + \frac{\alpha}{\sqrt{\pi}} \right) \sum_i^N q_i^2 \quad (2-27)$$

Where α is a damping constant. It has been shown for NaCl that the Madelung energy is almost independent of α all the way up to $1.5/a$ for $R_c=1.5a$. Here a is the lattice parameter of NaCl [52]. This method also works very well with disordered systems including liquids and defects.

2.8.2 Short-range Interactions

The need for short range interaction comes from the $1/r$ dependence of the Coulomb energy. In the limit “ r ” approaches zero, the long range interactions diverge which certainly is not the case in a real system. Without any other interactions, two oppositely charged ions would fall into each other and the system energy will become infinite. Various functional forms of short-range interactions have been developed for years, based on the material and properties under investigation. For example, to define characteristics of inert gases or neutral atoms or molecules Lennard-Jones [58] potential is used, for semiconductors Stillinger-Weber [59] potential is used.

The Buckingham potential [60] is used in this work, which is widely used to describe ionic materials. The functional form of the Buckingham potential is given by,

$$V_{Buck}(r_{ij}) = A_{ij} \exp(-r_{ij}/\rho_{ij}) - C_{ij}/r_{ij}^6 \quad (2-28)$$

where r_{ij} is the distance between ions i and j and A_{ij} , ρ_{ij} and C_{ij} are ion pair (i,j) dependent parameters. The first term of Eq 2-28, embeds the quantum mechanical exchange interaction effect into classical description of interaction. Exchange interaction in simple terms, takes care of the fact that no two electrons can have the same four quantum numbers (n,l,m_l,m_s) . Second term of Eq. 2-28 describes the Van der Waals attractive interaction due to dipole interaction. These empirical potentials are developed by fitting to the bulk material properties. That limits its use under extreme conditions such as high energy collisions. A more realistic model to capture the effect at very short range is described by Ziegler, Biersak and Littmark (ZBL) [61]. The ZBL interaction is a screened electrostatic potential of the nucleon-nucleon interaction:

$$V(r) = \frac{Z_1 Z_2 e}{r} \phi(r) \quad (2-29)$$

where Z_1 and Z_2 are the atomic numbers of the interacting atoms, e is the electron charge and r is the interatomic distance. $\phi(r)$ is the screening function,

$$\phi(r) = \sum_{i=1,4} A_i \exp\left(-b_i r / a_u\right) \quad (2-30)$$

where A_i and b_i are pre-defined parameters and are given in Table 2-1 and a_u is:

$$a_u = \frac{0.8854}{Z_1^{0.23} + Z_2^{0.23}} a_o \quad (2-31)$$

where a_o is the Bohr radius, 0.539177 Å.

Table 2-1. The ZBL parameters

i	A	b
1	0.1818	3.2000
2	0.5099	0.9423
3	0.2802	0.4028
4	0.02817	0.2016

The potential parameters for the MgO-Nd₂Zr₂O₇ system are summarized in Table 2-2. To incorporate the covalent nature of the crystal in case of MgO and Nd₂Zr₂O₇, partial charges are assigned to ions and are shown as superscripts.

Table 2-2. Potential parameters for the description of MgO-Nd₂Zr₂O₇ system [62, 63]

Species	A (eV)	$\rho(\text{\AA})$	C (eV \AA^6)
O ^{-1.7} -O ^{-1.7}	35686.18	0.20100	32.00
Nd ^{+2.55} -O ^{-1.7}	2148.14	0.32270	22.59
Zr ^{+3.4} -O ^{-1.7}	1402.57	0.33120	5.10
Mg ^{+1.7} -O ^{-1.7}	929.69	0.29909	0.00

Table 2-3 summarizes the interaction parameters for MgAl₂O₄. Every ion is assigned formal charges in this case.

Table 2-3. Short range potential parameters for MgAl₂O₄ from Ball *et al.* [64]

Species	A (eV)	$\rho(\text{\AA})$	C (eV \AA^6)
Mg ⁺² -O ⁻²	1279.69	0.2997	0.00
O ⁻² -O ⁻²	9547.96	0.2240	32.0
Al ⁺³ -O ⁻²	1361.29	0.3013	0.00

Table 2-4 summarizes the interaction parameters for $\text{Bi}_4\text{Ti}_3\text{O}_{12}$. Every ion is assigned a formal charge in $\text{Bi}_4\text{Ti}_3\text{O}_{12}$. Three different Ti-O interaction parameters are investigated and labeled by their A parameter values.

Table 2-4. Short range potential parameters for $\text{Bi}_4\text{Ti}_3\text{O}_{12}$ [65-67]

Species	A (eV)	$\rho(\text{\AA})$	C (eV \AA^6)
$\text{Bi}^{+3}-\text{O}^{-2}$	49529.4	0.2223	0.00
$\text{O}^{-2}-\text{O}^{-2}$	9547.96	0.2192	32.00
2131	2131.04	0.3038	0.00
$\text{Ti}^{+4}-\text{O}^{-2}$	760	760.47	0.3879
2549	2549.4	0.2989	0.00

Even though the interactions for $\text{Bi}_4\text{Ti}_3\text{O}_{12}$ were defined for core-shell model, the shell part is neglected interaction parameters for core-core only are used in this work. In a core-shell model, the electrons of an ion are divided into two parts: core and shell. Core electrons are combined with nucleus and assigned a +ve charge and the shell having all electrons, is given a -ve charge. The charge on each ion is described by the sum of the respective core and shell charges. The core and shell of each ion are connected by either a harmonic or anharmonic spring. For more details, please refer to the article by Dick and Overhauser [68].

2.9 Ensembles

Statistical mechanics is a useful method to study a system with large number of particles. It converts microscopic properties of the collections of individual atoms

(positions, velocities, etc.) or molecules to macroscopic bulk properties of materials that can be observed experimentally. The ensemble is simply a statistical equivalent of repeating the same experiment under the same macroscopic conditions but different microscopic ones and expects to observe a range of outcomes. A thermodynamic state of the system can be defined using various state variables: pressure (P), temperature (T), total number of atoms (N). Other thermodynamic properties (density, chemical potential, heat capacity etc.) may be derived using the equation of state and fundamental relations of thermodynamics. Even other microscopic properties, like diffusion coefficient, structure factor which clearly depicts microscopic structure and dynamics at the atomic level are dictated by the variables characterizing the thermodynamic state and not by microscopic properties.

The atomic positions and momenta are coordinates in the phase space (Γ). For a single particle, its phase space has 3 positions and 3 momenta totaling 6 dimensions. Let us assume, the instantaneous value of a property ζ can be written as $\zeta(\Gamma)$. Since system evolves with time and macroscopic property ζ is a time average of all these instantaneous value, and can be written as:

$$\zeta_{obs} = \langle \zeta \rangle_{time} = \lim_{t_{obs} \rightarrow \infty} \frac{1}{t_{obs}} \int_0^{t_{obs}} \zeta(\Gamma(t)) dt \quad (2-32)$$

As stated earlier, time evolution of the phase space is governed by the Newton's equation of motion. As the number of atoms increase in the system, solving Eq. 2-32 becomes a formidable task. Another concern is also the infinite time limit to perform the time average of Eq. 2-32. That can be resolved by taking a long enough time τ and

solving Newton's equation of motion in smaller time steps (δt). Replacing infinite time by τ and δt , Eq. 2-32 can be rewritten as:

$$\zeta_{obs} = \langle \zeta \rangle_{time} = \frac{1}{\tau} \sum_{i=1}^{\tau/\delta t} \zeta(\Gamma(i)) \quad (2-33)$$

Equation 2-33 provides a simulated value of the macroscopic property ζ by taking its time average. Instead of time evolution of the bulk properties, Gibbs suggested replacing time averages by the ensemble average. The ensemble is regarded as a collection of points Γ in the phase space. The points are distributed according to a probability density $\rho(\Gamma)$. This density function depends on the chosen fixed macroscopic parameters (NPT, NVE etc). These points are selected from

- i) Pair of extensive and intensive quantities including N (total no of particles) or μ (chemical potential)
- ii) The volume (V) or pressure (P)
- iii) The energy (E) or related thermodynamic potential or temperature (T)

In general, ensembles are categorized as microcanonical, canonical and grand-canonical based on different macroscopic constraints [44].

The microcanonical ensemble is used to describe the properties of an isolated system with fixed N, V and E and is also referred to as the NVE ensemble.

The canonical ensemble is a set of systems which can share its energy and maintains a constant temperature. They are in constant contact with a heat bath or reservoir and exchange energy to maintain a constant temperature. It is referred as NVT ensemble.

The grand canonical ensemble is a collection of systems which are in thermal contact with a heat bath or reservoir and can exchange particles. It can be viewed as an

extension of a canonical ensemble with the addition of particle exchange. The chemical potential μ is introduced to define the fluctuations in the number of particles. These three ensembles are not sufficient to cover all the experimental constraints. A list of all the statistical ensembles is given in Table 2-5.

Table 2-5. Summary of the eight statistical ensembles. For specific conditions the internal energy E is modified as the enthalpy ($H = E + PV$), the Hill energy ($L = E - \sum \mu_i N_i$), and the Ray enthalpy ($R = E + PV - \sum \mu_i N_i$) [69].

Fixed Variable	Ensemble
NVE	Microcanonical
NVT	Canonical
NPT	Isothermal-Isobaric (Gibbs)
NPH	Isoenthalpic-Isobaric
μ VT	Grand-canonical
μ VL	Grand-microcanonical
μ PR	Grand Isothermal-Isobaric
μ PT	Generalized

A generalized ensemble is not physical as its size is not specified [69]. Since in the simulations, mostly NPT and NVE ensembles are applied, it becomes important to briefly discuss the implementation of constant temperature and pressure in the simulation.

2.9.1 Pressure Control

The pressure control procedure developed by Andersen [70] and subsequently extended by Parrinello-Rahman [71], is now a standard tool. In a constant pressure simulation, the volume of the system fluctuates. Atom co-ordinates are redefined as

$$\rho_i = \frac{r_i}{V^{1/3}} \quad (2-34)$$

where, V is the box volume. Let us imagine the fluid to be simulated is in a container of variable volume V and is compressed by a piston. M is the mass of the piston and P is the pressure applied. Let us also assume that the volume change is isotropic or, equivalently an equal pressure is applied from all the directions (hydrostatic pressure).

This scenario can be represented by a Lagrangian given as follows:

$$L = \frac{1}{2} m V^{2/3} \sum_{i=1}^N \dot{\rho}_i \cdot \dot{\rho}_i - \sum_{i<j=1}^N u\left(V^{1/3} \rho_{ij}\right) + \frac{1}{2} M \dot{V}^2 - PV \quad (2-35)$$

The first two terms of Eq. 2-35 are the Lagrangian of the fluid in the container, third term corresponds to the kinetic energy of the piston and the last term refers to the potential energy of the piston. After constructing the Hamiltonian and forming equation of motions, the trajectory of each atom can be derived as follows:

$$\frac{Md^2V_i}{dt^2} = -P + \frac{1}{V} \left(\frac{2}{3} \sum_{i=1}^N \frac{p_i \cdot p_i}{2m} - \frac{1}{3} \sum_{i<j=1}^N \hat{r}_{ij} u'(r_{ij}) \right) \quad (2-36)$$

where, p_i is defined as $\frac{\pi_i}{V^{1/3}}$ and π is the conjugate momentum of ρ (atomic coordinates, as defined in Eq. 2-34). This method was extended by Parrinello and Rahman (PR) [71] to anisotropic stress. These methods are not good to capture first order phase transitions [72] for non periodic systems [73]. First order phase transition in PR scheme does not take place via nucleation and growth. Instead it takes place as a collective transformation which might result in an overestimation of the energy barrier for the phase transition. This can result in missing intermediate phases and lowers the predictive power of the PR scheme. To overcome these issues, a new method has been

developed by Martoňák, Laio and Parrinello [74]. Another scheme has been developed for finite system sizes by Sun and Gong [73]

2.9.2 Temperature Control

Most experiments are carried out at constant pressure and temperature. Usually, temperature is related to the average kinetic energy of the system as

$$\langle KE \rangle = \left\langle \sum_i \frac{mv_i^2}{2} \right\rangle = \frac{3}{2} Nk_B T \quad (2-37)$$

This issue is resolved by implementing a thermostat in MD. A simulated system is in constant contact with a heat bath or reservoir that acts as a thermostat.

The first and simplest method to implement constant temperature in MD simulation is a momentum-scaling algorithm proposed by Woodcock in 1971 [75]. In this method, at each simulation step, the velocity of each particle is rescaled to keep the average kinetic energy at the desired constant value calculated by Eq 2-37. It is also known as velocity rescaling method. Rescaled velocity is given by:

$$v_i (rescaled) = \sqrt{\frac{T_{target}}{T}} v_i \quad (2-38)$$

Various other methods to implement constant temperature in MD simulation have been reviewed here [44, 76]. They are proposed by Nosé [77], Hoover *et al.*[78] and Evans and Morriss [79], Haile and Gupta [80] and an extension to the extended system method of Nosé [76] by Hoover [81] that is known as Nosé-Hoover algorithm. Because of its simplicity, velocity rescaling method is used for the simulations.

2.10 Thermal Expansion Simulation

As a starting point in the simulation of thermal conductivity, coefficient of thermal expansion is computed using simulation. Thermal expansion is related to the lattice parameter to the first order, as follows:

$$\frac{a}{a_0} = 1 + \alpha T \quad (2-39)$$

where “a” is lattice parameter at temperature T and a_0 is the lattice parameter of the system at T = 0 K and α is the linear thermal expansion. To the first order approximation α can be computed by plotting a/a_0 as a function of temperature.

In the simulation, a cubic system is generated to calculate thermal expansion in all the directions. To compute thermal expansion, NPT ensemble is used and simulations are run at various temperatures to get a good profile between lattice parameter and temperature.

2.11 Thermal Conductivity Simulation

Fourier law relates the heat flux to the temperature gradient on a material:

$$J_i = -\kappa_{ij} \frac{\partial T}{\partial x_j} \quad (2-40)$$

where J_i , is the i^{th} component of heat flux (energy per unit area per unit time), κ_{ij} is an element of conductivity tensor and $\partial T/\partial x_j$ is the temperature gradient along j direction.

Experimentally, the thermal conductivity is measured using thermal diffusivity and the following relation

$$\kappa = \alpha \rho C_p \quad (2-41)$$

where α is the thermal diffusivity, ρ is the density and C_p is the specific heat capacity at constant pressure. Laser flash is the most widely used method to calculate thermal

diffusivity and is described in detail by Parker *et al.* [82]. In brief, A few millimeters thick thermally insulated sample is irradiated with a high-intensity short-duration light pulse and temperature history of the rear surface is measured. The thermal diffusivity is measured from the shape of temperature evolution with time curve at the rear surface. A schematic of flash method is shown in Fig. 2-15. In simulation, it can be determined by two ways: Non equilibrium MD (NEMD: direct method) [63, 79, 83-91] or equilibrium MD (EMD: Green-Kubo method) [83, 92-97].

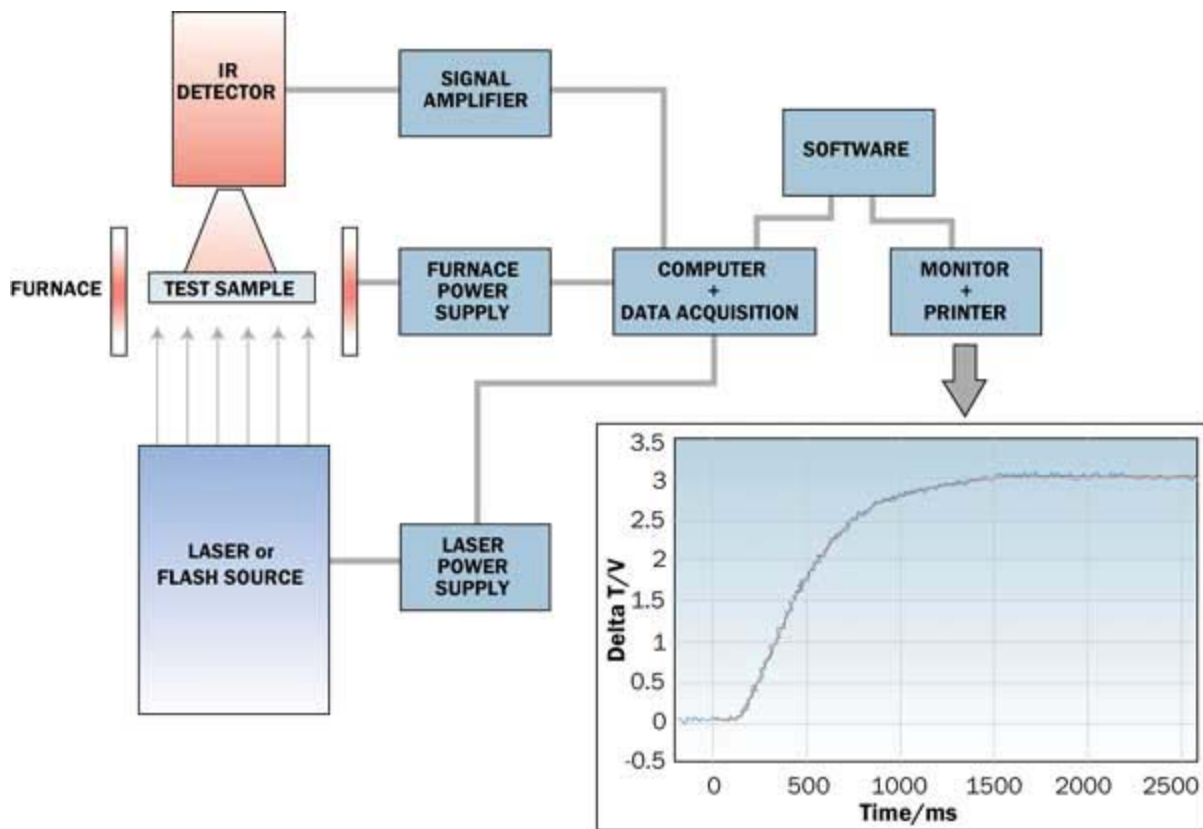


Figure 2-15. Schematic of flash diffusivity measurement and temperature rise curve. Adapted from the Ref [98].

The simulation set-up to measure thermal conductivity for direct method is shown in Fig. 2-16. System in direct method is set-up in a way that it is of cylindrical shape.

This size constraint (longer in one direction: z compared to other two: x and y) transforms Eq. 2-41 into scalar form as given below:

$$J = -\kappa \frac{\partial T}{\partial z} \quad (2-42)$$

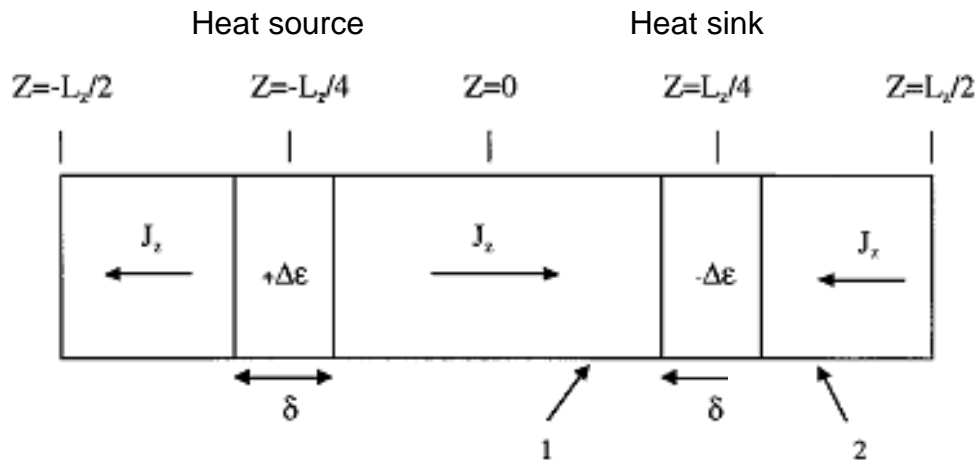


Figure 2-16. Schematics representation of simulation set-up for direct method (NEMD). Simulation cell has length L_z and heat source and sink both have thickness δ and at a distance $L_z/4$ from the edge/center of the cell. $\Delta\epsilon$ energy is added and removed at the source and sink respectively. Figure is adapted from reference [99].

To simulate the thermal conductivity, the system set-up follows these steps

1. Coefficient of thermal expansion is calculated at the desired temperature (Section 2-10).
2. System is equilibrated at 0 K.
3. Expansion coefficient is applied to the relaxed structure and equilibrated at the set temperature
4. Once the system reaches equilibrium at the set temperature, the temperature gradient is generated by giving extra energy to the atoms at the heat source and removing the same amount of energy from the atoms at the heat sink region.

5. This sets up a temperature gradient and its average over time is used to compute the thermal conductivity using Eq. 2-42.

The size of the simulation cell strongly affects the value of thermal conductivity determined, as illustrated in the case of Si [99]. When the simulation cell is smaller than the phonon mean free path, thermal conductivity is limited by system size. This is known as the Casimir limit. To account for this effect, the thermal conductivity is calculated as a function of system size and then extrapolated to infinite system size. Following is the physics behind this phenomena and methodology to overcome the issue.

By applying the kinetic theory of gases, the thermal conductivity was shown to be equal to:

$$\kappa = \frac{1}{3} cvl \quad (2-43)$$

where, c is the specific heat, v is the group velocity and l is the effective mean free path of the phonons. Specific heat above the Debye temperature is given by the Dulong-Petit value for a non-interacting gas:

$$c = \frac{3}{2} k_B n \quad (2-44)$$

where, k_B is the Boltzmann constant and n is the number density of the ions. For a unit cell of volume V and total number of ions N , n is given as N/V . Group velocity v can

be expressed as: $v = \frac{(v_L + 2v_T)}{3}$, where v_L and v_T are the longitudinal and transverse

sound velocities. For a simulation cell of length L_z , the phonon mean free path is $L_z/4$ (As shown in Fig. 2-16, heat source and heat sink are at $L_z/4$). If l_∞ is the phonon mean

free path for infinite system, then the effective mean free path for system size with L_z length is given by [99]:

$$l_{eff}^{-1} = l_{\infty}^{-1} + 4/L_z \quad (2-45)$$

The final expression for thermal conductivity is:

$$\kappa = \frac{1}{3} \left(\frac{3}{2} k_B \frac{N}{V} \right) \left(\frac{v_L + 2v_T}{3} \right) \left(\frac{1}{l_{\infty}} + \frac{4}{L_z} \right)^{-1} \quad (2-46)$$

For a cubic system, the thermal conductivity and system size relation reduces to:

$$\frac{1}{\kappa} = \frac{2a^3}{k_B Nv} \left(\frac{1}{l_{\infty}} + \frac{4}{L_z} \right) \quad (2-47)$$

Equation 2-47 shows a linear relation between the inverse of thermal conductivity and inverse of system size. The methodology to infer thermal conductivity for infinite system size can be simply achieved by extrapolating the thermal conductivity values at $1/L_z=0$. This approach has been applied to Si and diamond single crystals [99] and will be used here.

In case of thermal conductivity, the coefficient of thermal expansion and elastic properties are calculated first. "Anharmonic analysis" is used to correct simulated thermal conductivity values based on the fidelity of interaction parameters with experimental thermal expansion and bulk modulus values. Details of the analysis are presented in chapter-4 with MgO-Nd₂Zr₂O₇ results.

CHAPTER 3 CRYSTALLOGRAPHY OF RELEVANT MATERIAL SYSTEMS

3.1 General Introduction

Crystallography is formed from two Greek words, *crystallon* meaning frozen drop/cold drop, and *grapho* meaning write. Crystallography refers to the science of determining the arrangement of atoms in solids. Crystallography also provides insight into material properties and plays a major role in many subjects, including mineralogy, physics, materials science, chemistry, geology, geophysics and medicine. In essence, it encompasses various areas of science and engineering.

Materials with the same chemical composition exhibit different properties based upon their crystal structures. For example, graphite and diamond both are forms of carbon but differ in crystal structure and show disparity in almost all physical properties. Another example is PbTiO_3 , which is cubic at room temperature and paraelectric but as it changes to the tetragonal structure at 763 K shows ferroelectricity [100].

The structure of a material can be understood as a description of the arrangement of the components that make up the material. All the atoms/ions can be taken as building blocks of the materials, especially solids. The limiting factor here is the sheer number of atoms to describe a small piece of material. For example a tiny cube of salt (NaCl) has approximately 10^{20} atoms. If a material is perfectly ordered, then by exploiting periodicity, a smaller representative unit of NaCl can be used to describe NaCl for any length scale. The smallest representative unit of any structure is called its unit cell. Standard descriptions of all the space groups are given in The *International Tables for Crystallography* [101]. Both Hermann-Mauguin and Schönflies notations are used to describe the symmetry of the materials investigated. Schönflies notation is

adequate only to describe the point group and thus generally used in spectroscopy. Hermann-Mauguin notation is generally used in crystallography because it includes space group symmetry also in the notation.

3.2 MgO: Rocksalt Crystal Structure

The rocksalt structure is named after NaCl (halite). Almost every alkali halide, sulfide, selenide and telluride form rocksalt structure [102]. Almost one third of all MX type compounds crystallize to the rock-salt structure, where M is the cation and sits at $(0, 0, 0)$ and X is an anion and sits at $(0, 0, 1/2)$. MgO has the rocksalt crystal structure. The equal number of cations and anions in the rocksalt structure are arranged as interpenetrating FCC sublattices. The unit cell of rocksalt crystal structure with MgO as an example is shown in Fig. 3-1, with O as large ions and Mg as smaller ions. The conventional cubic unit cell contains 4 formula units of MgO ($Z=4$).

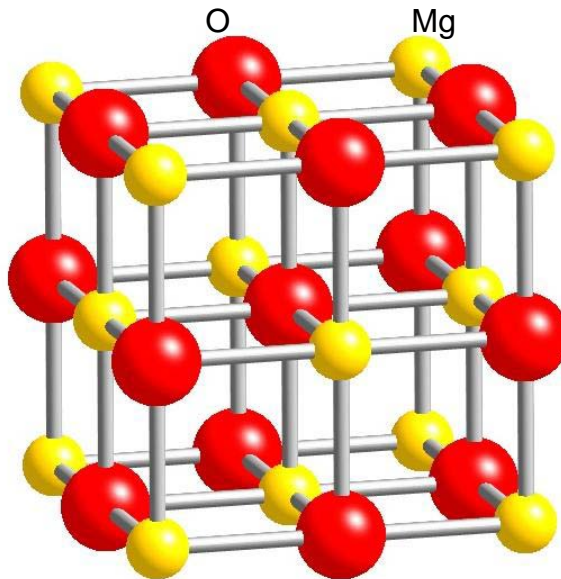


Figure 3-1. Conventional cubic unit cell of MgO. Mg (small circle) and O (big circle)

The rocksalt structure belongs to the $Fm\bar{3}m$ (O_h^5 , No. 225 in the international table) space group, where $Fm\bar{3}m$ is space group representation in Hermann-Mauguin and O_h^5 is in Schönflies notation. O_h^5 represents octahedral symmetry (four 3-fold axes along body diagonals with three 4-fold axes along the faces) and mirror planes. In Hermann-Mauguin notation, F represents a face center cubic structure and $m\bar{3}m$, a short form for $\frac{4}{m}\frac{3}{m}\frac{2}{m}$ point group represents operations along the primary $\langle 001 \rangle$, secondary $\langle 111 \rangle$ and tertiary $\langle 110 \rangle$ direction of the cubic system.

For MgO, the $4/m$ represents four-fold rotational symmetry at the corners and the cell center, and a mirror perpendicular to the rotational axis $[100]$ (Fig. 3-2(a)). The $\bar{3}$ symmetry represents the roto-inversion along the body diagonal $[111]$ of the unit cell (Fig. 3-2(b)). The $2/m$ symmetry operation represents the two-fold rotation along the edges of the unit cell, and a mirror plane perpendicular to the axis of rotation (Fig. 3-2(c)).

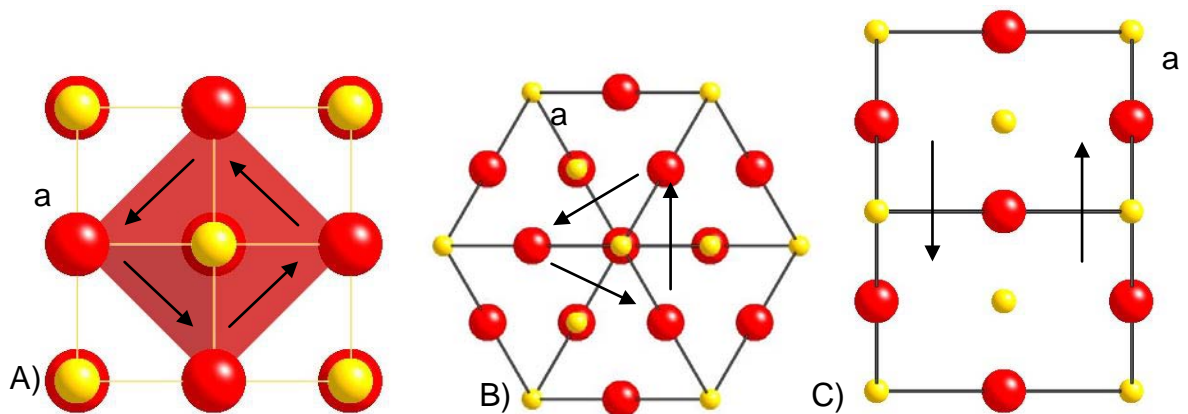


Figure 3-2. Schematics showing three different symmetry operations represented by MgO A) A four-fold rotation symmetry along $[100]$. B) A three-fold inversion symmetry along $[111]$. C) A two-fold rotation symmetry along $[110]$.

The lattice parameter of MgO unit cell is 4.191 Å [103]. Table 3-1 lists the site symmetry, the Wyckoff position and coordinates of the atoms for rocksalt structure AX.

Table 3-1. Rocksalt AX crystal structure

Ion	Wyckoff position	Site symmetry	Coordinates (0,0,0; 0,1/2,1/2; 1/2, 0, 1/2; 1/2, 1/2, 0)+
A	4a	O _h	0,0,0
X	4b	O _h	1/2,1/2,1/2

The first column of Table 3-1 lists the ions present in the system (for example, AX has cation A and anion X). The second column gives information about Wyckoff position that represents a total number of equivalent points. The letter in the Wyckoff position goes in alphabetic order from high to low symmetry, for example 'a' is assigned to the equipoint having the least number of equivalent points. The third column contains information about the point symmetry of the corresponding position. The last column gives the coordinates of the ions. The positions under the "coordinates" title are called the generators. All the positions of atoms/ions are calculated by adding the coordinates to the generators. For example, from Table 3-1, ion A has 4 multiplicity and all 4 positions are calculated by adding (0,0,0) to (0,0,0), (0,1/2,1/2), (1/2,0,1/2) and (1/2,1/2,0). Similarly, coordinates of X can be calculated by adding (1/2,1/2,1/2) to (0,0,0), (0,1/2,1/2), (1/2,0,1/2).

3.3 Nd₂Zr₂O₇: Pyrochlore Crystal Structure

Nd₂Zr₂O₇ (NDZ) belongs to the pyrochlore family and has general formula A₂B₂O₇ [104]. The space group for pyrochlore structure is $Fd\bar{3}m$ ($F\frac{4}{d}\bar{3}2/m$, O_h⁷ No. 227 in the international table [101]). Similar to the rocksalt crystal symmetry, pyrochlore also has 3-fold roto-inversion along (111) and 2-fold rotation axis with perpendicular

mirror along (110). Instead of 4-fold rotation axis with perpendicular mirror plane, this has 4_1 screw axis with diamond glide. A screw axis (helical axis or twist axis) is a combination of rotation plus translation symmetry. 4_1 screw axis represents a rotation of 90° ($360^\circ/4$) and translation of $\frac{1}{4}$ of the lattice vector parallel to the rotation axis.

The crystal structure of pyrochlore materials is closely related to the fluorite structure. There are two main differences between the fluorite and pyrochlore crystal structures: anions occupy all 8 tetrahedral sites in fluorite and only 7 in pyrochlore, and pyrochlores have approximately twice the lattice spacing of fluorite structures, i.e. one unit cell of pyrochlore structure can be divided into 8 sub units with each sub unit similar to a fluorite structure [105]. Figure 3-3 shows one-eighth of the pyrochlore structure and the fluorite structures side by side.

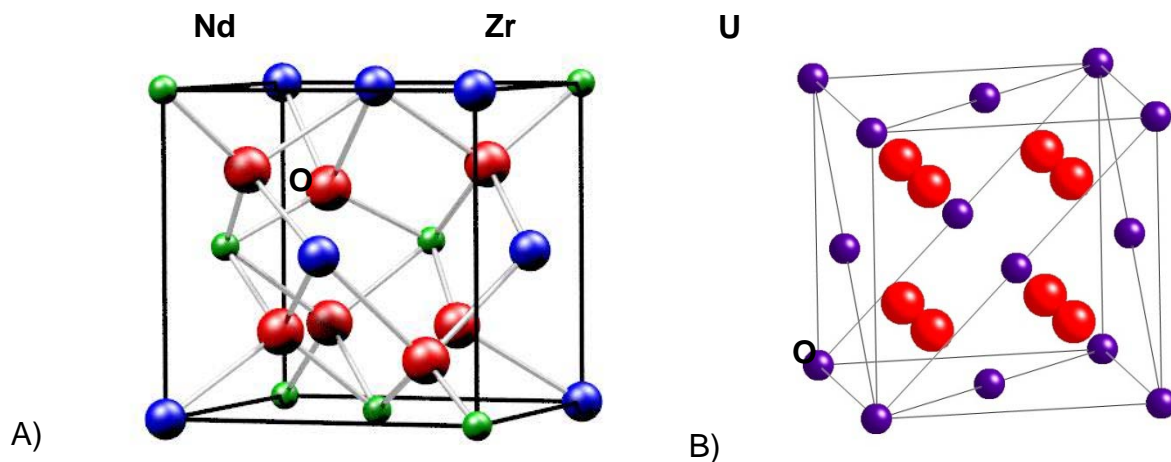


Figure 3-3. A) Pyrochlore sub unit (1/8) B) Fluorite unit cell

Cations A and B are 8- and 6-fold coordinated respectively, and can have either +3 and +4 or +2 and +5 oxidation states. Based on the charge and oxidation state, the ionic radius of cation A should lie within 0.087-0.151 nm [105]. Similarly ionic radius of B should lie in the range of 0.040-0.078 nm [105]. Furthermore, the radius ratio of r_A/r_B

should lie between 1.29-2.30 [105, 106]. Generally for the +3/+4 pyrochlores, lanthanides (3+) occupy A sites and 4+ cations take the B sites.

As seen in Fig. 3-3, cations sit at the corner and face center positions; while anions occupy tetrahedral sites. In pyrochlore, the cations form face centered cubes and are ordered in alternate (110) and $(\bar{1}10)$ rows (face diagonals). The anions are located in all of the tetragonal sites except the ones which are surrounded by the A cations only [104]. The unit cell of pyrochlore is composed of two types of sub-unit cells, arranged in alternate manner.

Type I. The A cations form face diagonal at the upper right-hand corner and missing anion is at the lower left-hand. (Fig. 3-4A)

Type II. The A cations form face diagonal at the lower left-hand corner and missing anion is at the opposite corner. (Fig. 3-4B)

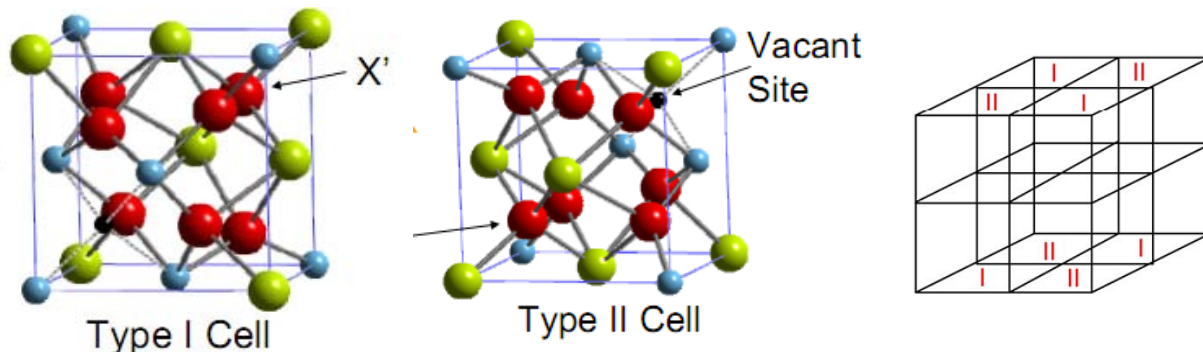


Figure 3-4. Two types of subcells, that forms the unit cell of pyrochlore with alternate mixing [107]

The structural difference of one less anion to complete the cube inside the cell identifies two types of cations in the system. They are denoted by X and X', where X' is the diagonally situated cation from the vacant site and rest are defined by X. The unit cell of pyrochlore contains equal number of Type-I and Type-II subcells and is arranged

in a manner that only different types of subcells become neighbors. Figure 3-4 shows one typical arrangement of both types of subcells. Due to this structural feature,

The lattice parameter of NDZ is ($a = 8.089 \text{ \AA}$) which is almost double that of MgO ($a = 4.202 \text{ \AA}$). This difference becomes important when composite structures of MgO and NDZ are built for the simulations. The polycrystalline structures of MgO and NDZ are used to separate out the interface effects of each individual component of the proposed inert matrix system. Structural information for pyrochlore crystal structure including location, site symmetry and coordinates with origin fixed at Zr cation, are given in Table 3-2.

Table 3-2. Pyrochlore $A_2B_2X_6X'$ crystal structure with origin at B cation [104]

Ion	Wyckoff position	Site symmetry	Coordinates (0,0,0; 0,1/2,1/2; 1/2, 0, 1/2; 1/2, 1/2, 0)+
A	16d	D_{3d}	1/2,1/2,1/2; 1/2,1/4,1/4; 1/4,1/2,1/4; 1/4,1/4,1/2
B	16c	D_{3d}	0,0,0; 0,1/4,1/4; 1/4,0,1/4; 1/4,1/4,0
X	48f	C_{2v}	x,1/8,1/8; -x,7/8,7/8; 1/4-x,1/8,1/8; 3/4+x,7/8,7/8 1/8,x,1/8; 7/8,-x,7/8; 1/8,1/4-x,1/8; 7/8,3/4+x,7/8 1/8,1/8,x; 7/8,7/8,-x; 1/8,1/8,1/4-x; 7/8,7/8,3/4+x
X'	8b	T_d	3/8,3/8,3/8; 5/8,5/8,5/8 x for regular tetrahedral = 5/16 (0.3125) x for regular cube = 3/8 (0.375)

From Table 3-2, value of x ranges from 0.3125 to 0.375 and depend on the specific composition. Exact value of x can be determined by experimentally characterizing the sample using for example X-ray diffraction, neutron diffraction.

3.4 $MgAl_2O_4$: Spinel Crystal Structure

The general formula for the spinel compounds is AB_2O_4 , where A is usually a divalent cation and B is a trivalent cation. In this thesis, A is Mg^{2+} and sits on 8a tetrahedral sites, and B is Al^{3+} and occupies the 16b octahedral sites. The cubic unit cell contains 8 formula units for a total of 24 cations (8 Mg ions and 16 Al ions) and 32

anions (all O ions). This unit cell can be considered as consisting of 8 cubic subunits, as shown in Fig. 3.5. Bragg [108] and Nishikawa [109] determined the crystal structure of spinel in the early 1900s. The majority of spinels belong to space group $Fd\bar{3}m$ (O_h^7 , No. 227 in the international table [101]).

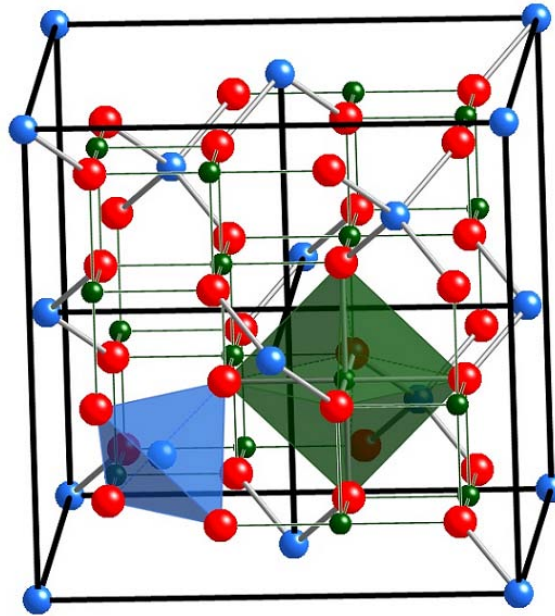


Figure 3-5. Cubic spinel unit cell with Mg (blue, medium sized), Al (green, small) and O (red, large) atoms. The unit cell can be considered as being divided into 8 subunits with Mg tetrahedral (blue) and Al octahedral (green) in alternating sub cells

There are total 64 octahedral and 32 tetrahedral interstices between anions in the spinel unit cell. Among these, 8 tetrahedral interstices are occupied by A cation and 16 octahedral interstices by B cation in the normal spinel structure. The atomic positions in the spinel structure depend largely on the choice of origin in the $Fd\bar{3}m$ space group. Two different points with point symmetries $\bar{4}3m$ and $\bar{3}m$ are possible choices for the origin. Table 3-3 lists the atomic positions for normal spinel structure with both origin choices.

Table 3-3. Fractional coordinates for atomic positions and vacancies for spinel [110]

Lattice Site	Wyckoff Position	Point Symmetry	Fractional coordinates (0,0,0; 0,1/2,1/2; 1/2, 0, 1/2; 1/2, 1/2, 0)+	
			Origin	
			$\bar{4}3m$	$\bar{3}m$
A-site	8a	$\bar{4}3m$	$0,0,0; \frac{1}{4}, \frac{1}{4}, \frac{1}{4}$	$\frac{1}{8}, \frac{1}{8}, \frac{1}{8}; \frac{7}{8}, \frac{7}{8}, \frac{7}{8}$
B-site	16d	$\bar{3}m$	$\frac{5}{8}, \frac{5}{8}, \frac{5}{8}; \frac{5}{8}, \frac{7}{8}, \frac{7}{8};$ $\frac{7}{8}, \frac{5}{8}, \frac{7}{8}; \frac{7}{8}, \frac{7}{8}, \frac{5}{8};$	$\frac{1}{2}, \frac{1}{2}, \frac{1}{2}; \frac{1}{2}, \frac{1}{4}, \frac{1}{4};$ $\frac{1}{4}, \frac{1}{2}, \frac{1}{4}; \frac{1}{4}, \frac{1}{4}, \frac{1}{2};$
X	32e	$3m$	$u, u, u; u, \bar{u}, \bar{u}; \bar{u}, u, \bar{u}; \bar{u}, \bar{u}, u;$ $(\frac{1}{4}-u), (\frac{1}{4}-u), (\frac{1}{4}-u);$ $(\frac{1}{4}+u), (\frac{1}{4}+u), (\frac{1}{4}-u);$ $(\frac{1}{4}+u), (\frac{1}{4}-u), (\frac{1}{4}+u);$ $(\frac{1}{4}-u), (\frac{1}{4}+u), (\frac{1}{4}+u)$	$u, u, u; \bar{u}, \bar{u},$ $u, (\frac{1}{4}-u), (\frac{1}{4}-u); (\frac{1}{4}-u), u, (\frac{1}{4}-u);$ $(\frac{1}{4}-u), (\frac{1}{4}-u), u; \bar{u}, (\frac{3}{4}+u), (\frac{3}{4}+u);$ $(\frac{3}{4}+u), \bar{u}, (\frac{3}{4}+u); (\frac{3}{4}+u), (\frac{3}{4}+u), \bar{u};$
Tetrahedral vacancy	8b	$\bar{4}3m$	$\frac{1}{2}, \frac{1}{2}, \frac{1}{2};$ $\frac{3}{4}, \frac{3}{4}, \frac{3}{4}$	$\frac{3}{8}, \frac{3}{8}, \frac{3}{8};$ $\frac{5}{8}, \frac{5}{8}, \frac{5}{8}$
Octahedral vacancy	16c	$\bar{3}m$	$\frac{1}{8}, \frac{1}{8}, \frac{1}{8}; \frac{1}{8}, \frac{3}{8}, \frac{3}{8};$ $\frac{3}{8}, \frac{1}{8}, \frac{3}{8}; \frac{3}{8}, \frac{3}{8}, \frac{1}{8};$	$0,0,0; 0, \frac{1}{4}, \frac{1}{4};$ $\frac{1}{4}, 0, \frac{1}{4}; \frac{1}{4}, \frac{1}{4}, 0$
Tetrahedral vacancy	48f	mm	$\frac{1}{4}, 0, 0; 0, \frac{1}{4}, 0; 0, 0, \frac{1}{4};$ $-\frac{1}{4}, 0, 0; 0, -\frac{1}{4}, 0; 0, 0, -\frac{1}{4};$ $\frac{1}{2}, \frac{1}{4}, \frac{1}{4}; \frac{1}{4}, \frac{1}{2}, \frac{1}{4}; \frac{1}{4}, \frac{1}{4}, \frac{1}{2};$ $0, \frac{1}{4}, \frac{1}{4}; \frac{1}{4}, 0, \frac{1}{4}; \frac{1}{4}, \frac{1}{4}, 0;$	$\frac{3}{8}, \frac{1}{8}, \frac{1}{8}; \frac{1}{8}, \frac{3}{8}, \frac{1}{8}; \frac{1}{8}, \frac{1}{8}, \frac{3}{8};$ $-\frac{3}{8}, \frac{7}{8}, \frac{7}{8}; \frac{7}{8}, -\frac{3}{8}, \frac{7}{8}; \frac{7}{8}, \frac{7}{8}, -\frac{3}{8};$ $-\frac{1}{8}, \frac{1}{8}, \frac{1}{8}; \frac{1}{8}, -\frac{1}{8}, \frac{1}{8}; \frac{1}{8}, \frac{1}{8}, -\frac{1}{8};$ $\frac{1}{8}, \frac{7}{8}, \frac{7}{8}; \frac{7}{8}, \frac{1}{8}, \frac{7}{8}; \frac{7}{8}, \frac{7}{8}, \frac{1}{8}$

The oxygen atoms sit at (u, u, u) where u is approximately $\frac{1}{4}$. For each spinel structure, permissible values of u can be calculated based on the cations radii and charges. The value of u changes with inversion and that in effect changes the lattice

parameter of the structure. The relation between bond lengths and lattice parameter is given as [111]:

$$a = \frac{40d_T + 8\sqrt{33d_O^2 \pm 8d_T^2}}{11\sqrt{3}} \quad (3-1)$$

where, a = unit cell edge or lattice parameter

d_O = bond length of cation-O at octahedral site

d_T = bond length of cation-O at tetrahedral site

Cation Arrangement: It has long been established that spinel crystals can accommodate significant amount of cation disorder or so called “variate atom equipoints” [112, 113]. The structure with cation disorder is termed as “inverse spinel”, introduced by Verwey and Heilmann [114]. Inversion is traditionally denoted by i and is given as:

$$i = \frac{\text{No. of Al on tetrahedral sites}}{\text{Total no. of Mg}} \quad (3-2)$$

The value of i ranges from 0 to 1, where 0 has all the cations on their normal crystal sites (Mg at tetrahedral and Al on octahedral) and 1 refers to the structure with all the Mg on octahedral sites and Al equally divided on octahedral and tetrahedral sites. Based on inversion, disorder in the spinel structure is described by Q , which is defined as [115, 116]:

$$Q = 1 - \frac{3i}{2} \quad (3-3)$$

The value of Q , ranges from 1 ($i=0$) to -0.5 ($i=1$). Q is 0 for randomly disordered structure ($i=2/3$). The modified structural formula is used to project cation disorder in the

system $\left[M(2)_i^{q+} M(1)_{1-i}^{p+} \right]^{A_{IV}} \left[M(1)_{\frac{i}{2}}^{p+} M(2)_{1-\frac{i}{2}}^{q+} \right]_2^{B_{VI}} X_4$ where $M(1)^{p+}$ refers to divalent and $M(2)^{q+}$ to trivalent cations. The first bracket represents the cation arrangement on tetrahedral sites. Similarly the second bracket represents cation arrangement on octahedral sites.

3.5 Bi₄Ti₃O₁₂: Aurivillius Crystal Structure

Bismuth layer compounds belong into the Aurivillius family of layered perovskite and are denoted by $(\text{Bi}_2\text{O}_2)^{2+}(\text{A}_{n-1}\text{B}_n\text{O}_{3n+1})^{2-}$ [117]. The crystal structure can be visualized as alternate stacking of $(\text{A}_{n-1}\text{B}_n\text{O}_{3n+1})^{2-}$ perovskite layers and $(\text{Bi}_2\text{O}_2)^{2+}$ fluorite-like layers along the c-axis, where n represents the number of perovskite layers between Bi₂O₂ layers. Various compounds with different n values have been prepared and are presented in Table 3-4.

Table 3-4. Various Aurivillius structures for different n values

n value	Material	Reference
1	Bi ₂ WO ₆	Rae <i>et al.</i> [118]
2	Bi ₂ SrNb ₂ O ₉	Ismunandar <i>et al.</i> [119, 120]
3	Bi ₄ Ti ₃ O ₁₂	Aurivillius [117]
4	Bi ₅ Ti ₃ MnO ₁₅	Kumar <i>et al.</i> [121]
5	Bi ₂ Ba ₂ Ti ₅ O ₁₈	Aurivillius and Fang [122]

Bismuth titanate Bi₄Ti₃O₁₂ (BIT) belongs to Aurivillius structure family with n=3 value. The crystal structure of BIT in ferroelectric phase (T >950 K) is tetragonal with I4/mmm symmetry and has a~3.85 Å and c ~ 32.832 Å [118]. As temperature is lowered, the system undergoes structural changes and forms a lower symmetry

structure with “a” and “b” lattice constants elongated by $\sim\sqrt{2}$ of their tetragonal structure values.

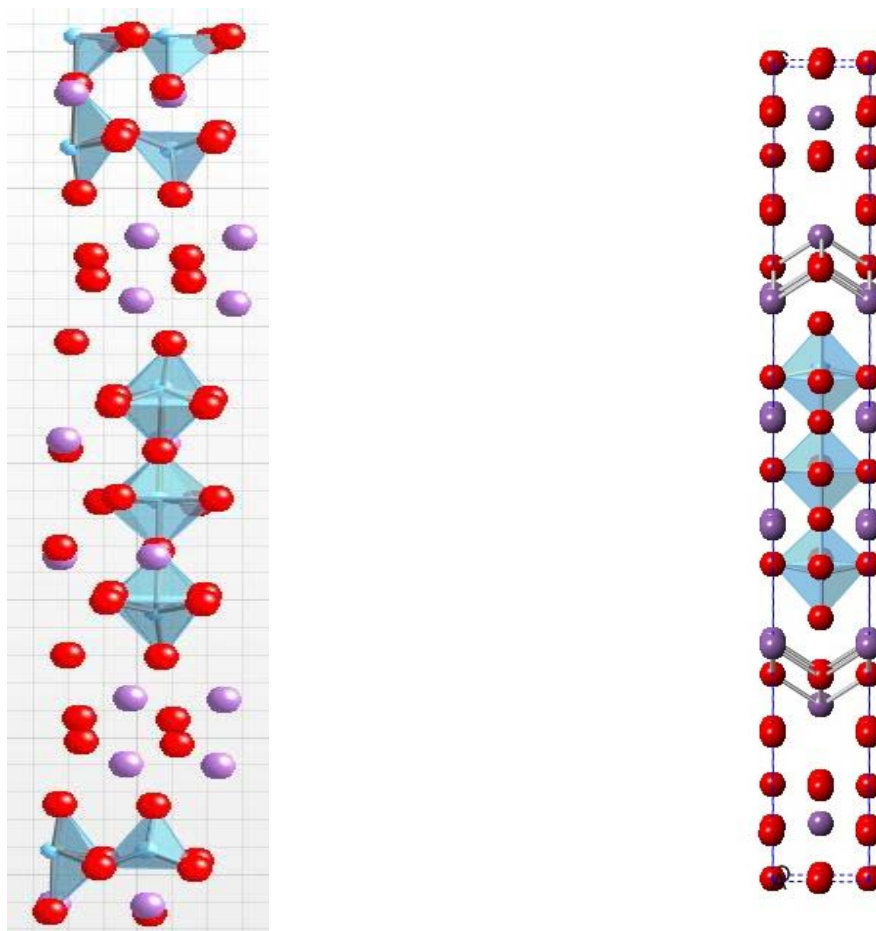


Figure 3-6. Unit cell of $\text{Bi}_4\text{Ti}_3\text{O}_{12}$ for A) low temperature monoclinic structure B) high temperature tetragonal structure, Bi is violet, O is red and Ti is light blue

Figure 3-6 compares the high temperature tetragonal structure with low temperature structure. The atomic positions for tetragonal as well as low temperature monoclinic structure are given in Tables 3-5 and 3-6, respectively. Low temperature lattice parameters are taken as $a=5.450 \text{ \AA}$, $b=5.4059 \text{ \AA}$, and $c=32.832 \text{ \AA}$ and all the angles 90° [123]. There is no consensus over the low temperature crystal structure of BIT and scientific community is divided between orthorhombic and monoclinic

structures. A list of experimental investigations and their conclusion on the structure of BIT is shown in Table 3-7.

Table 3-5. Fractional coordinates for tetragonal structure (I4/mmm) of BIT [124]

Atom	Site	Fractional coordinates		
		X	Y	Z
Bi	4a	0.5	0.5	± 0.5667
Bi	4a	0.5	0.5	± 0.0662
Ti	4a	0.0	0.0	0.0
Ti	4a	0.0	0.0	± 0.1259
O	4a	0.0	0.5	0.0
O	4a	0.5	0.0	0.0
O	4a	0.0	0.5	± 0.1141
O	4a	0.5	0.0	± 0.1141
O	4a	0.0	0.0	± 0.0593
O	4a	0.0	0.0	± 0.1802
O	4a	0.0	0.5	0.25
O	4a	0.5	0.0	0.25

Table 3-6. Fractional coordinates for monoclinic structure (B1a1) of BIT [125]

Atom	Site	Fractional coordinates		
		X	Y	Z
Bi	4a	0.0407	0.5041	0.5667
Bi	4a	0.0427	0.4777	0.7104
Ti	4a	0.0849	-0.0044	0.4969
Ti	4a	0.0948	0.0014	0.6279
O	4a	0.3401	0.2710	0.5086
O	4a	0.3036	0.2389	0.2473
O	4a	0.1375	-0.0614	0.5585
O	4a	0.0879	0.0406	0.6815
O	4a	0.3212	0.2747	0.6118
O	4a	0.4071	-0.2036	0.6257
Bi	4a	0.0429	0.4991	0.4332
Bi	4a	0.0386	0.5170	0.2878
Ti	4a	0.0884	0.0093	0.3716
O	4a	0.3884	-0.2203	0.4944
O	4a	0.3213	-0.2443	0.7480
O	4a	0.1215	0.0638	0.4402
O	4a	0.1039	-0.0573	0.3187
O	4a	0.3418	-0.2720	0.3890
O	4a	0.3899	0.2095	0.3775

Aurivillius in his X-ray diffraction study conceived the structure as orthorhombic with space group *Fmmm*. Later neutron diffraction studies suggested the orthorhombic

structure with *B2cb* space group (#41, in the international table [101]) [126, 127]. In other studies using single crystal X-ray diffraction, Rae *et al.* [123] and Shimakawa *et al.* [128] reported the monoclinic structure with the *B1a1* space group (#7, in the international table [101]). From the crystallography perspective, the only difference between *B1a1* and *B2cb* space group is the absence or presence of b-glide. Experimentally, it is very hard to differentiate between these two space groups. The controversy arises because all of these possible structures are subgroups of *I4/mmm*. Figure 3-7 represents a group-subgroup graph connecting the space groups *I4/mmm* and *B1a1*. Table 3-7 summarizes the experimental investigations and their results for the structure of BIT.

Table 3-7. Historical preview for structures of BIT

Year	Method	Structure	Lattice Parameters	Reference
1949	Single crystal X-ray	<i>B2cb</i> (Orthorhombic)	$a=5.410\text{\AA}$ $b=5.448\text{\AA}$ $c=32.800\text{\AA}$	Aurivillius [117]
1971		<i>B2cb</i> (Orthorhombic)	$a=5.448\text{\AA}$ $b=5.411\text{\AA}$ $c=32.83\text{\AA}$	Dorrian <i>et al.</i> [127]
1990	No b glide → polarization along c-axis	<i>B1a1</i> (Monoclinic)	$a=5.45\text{\AA}$ $b=5.4059\text{\AA}$ $c=32.832\text{\AA}$ $\beta=90^\circ$	Rae <i>et al.</i> [123]

Table 3-7 Cont

Year	Method	Structure	Lattice Parameters	Reference
1999	Neutron power diffraction	B2cb (Orthorhombic)	a=5.444Å b=5.4086 Å c=32.8425 Å	Hervoches and Lightfoot [126]
2001	Neutron power diffraction	B1a1 (Monoclinic)	a=5.44521Å b=5.41118 Å c=32.8432 Å	Shimakawa <i>et al.</i> [128]
2003	Neutron power diffraction	B1a1 (Monoclinic)	a=5.4475Å b=5.4082 Å c=32.8066 Å	Kim <i>et al.</i> [129]
2007	Rietveld refinement of powder neutron diffraction	B2cb (Orthorhombic)	a=5.4432Å b=5.4099 Å c=32.821 Å	Chakraborty <i>et al.</i> [130]
2008	DFT	B1a1 (Monoclinic)	a=5.4289Å b=5.4077 Å c=32.8762 Å	Shrinagar <i>et al.</i> [131]
2008	Odd n:B2cb Even n:A2 ₁ am	B1a1 (Monoclinic)	a=5.411Å b=5.448 Å c=32.83 Å	Jardiel <i>et al.</i> [132]

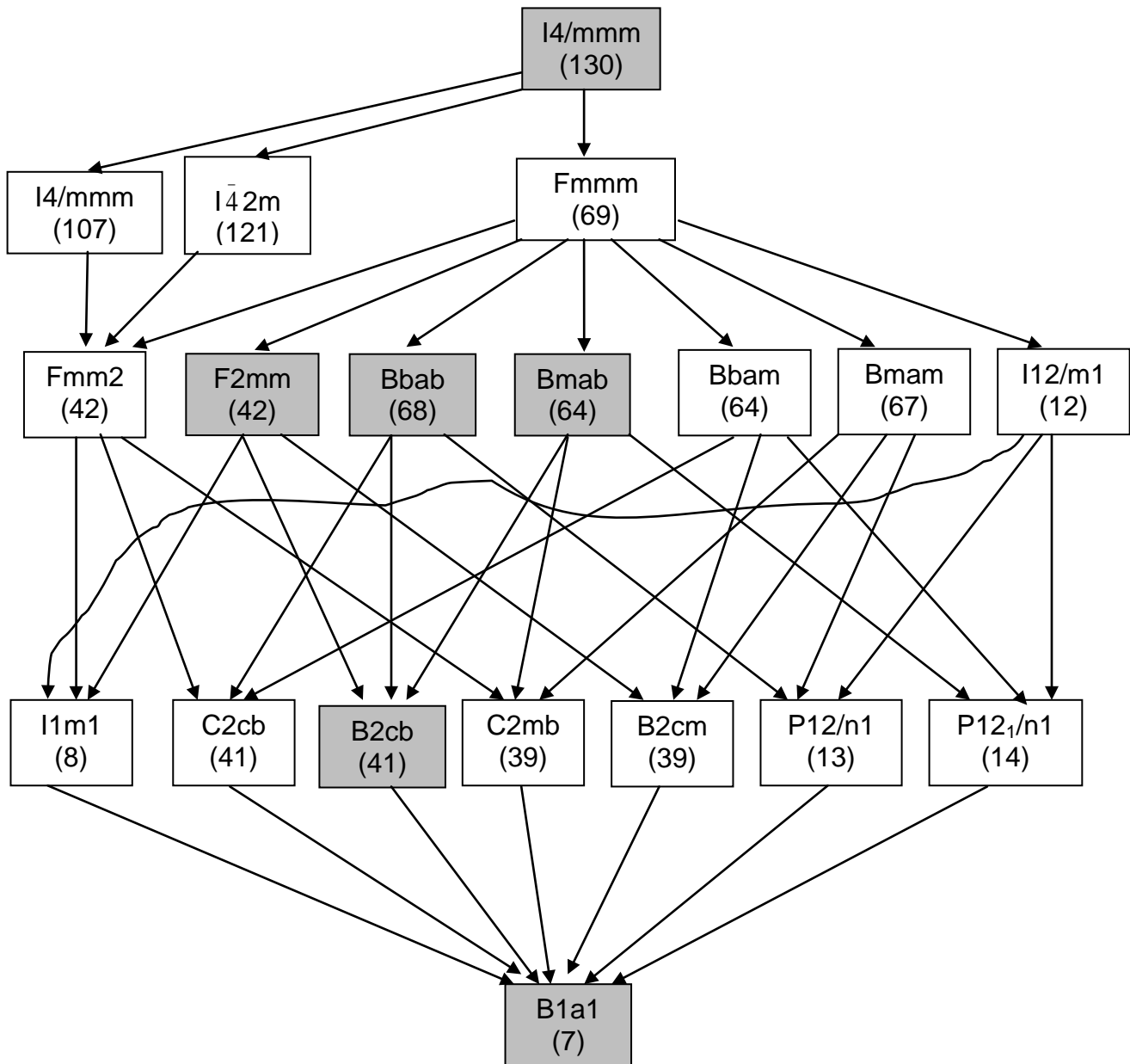


Figure 3-7. Group-subgroup graph connecting I4/mmm to B1a1 [133]

The structural controversy can be resolved with the help of symmetry constraints on the physical properties. BIT showed a finite polarization along the *c* axis, which is unlikely in the B2cb structure because the b-glide has its mirror plane perpendicular to the *c* axis and thus all the polarization vectors along the *c* axis cancel out. Following the study by Shrinagar *et al.* [131], the fractional coordinates for B1a1 crystal structure can be derived by the appropriate transformations to its original Bravais lattice P1n1. Point 1

of P1n1 (x,y,z) remains unchanged but point (x+1/2,-y+1/2,z) changes to (x+1/2,-y+1/2,z+1/2).

An important feature of these layered perovskites is the tilting of the octahedra. Figure 3-7 captures the nature of octahedra tilting along different axes. The effect of tilting is associated with the onset of ferroelectric phase change in Aurivillius structures. A study by Newnham *et al.* [134] suggested that increasing the number of perovskite units in Aurivillius structure ($\text{Bi}_4\text{Ti}_3\text{O}_{12}$, $\text{SrBi}_4\text{Ti}_4\text{O}_{15}$, $\text{Sr}_2\text{Bi}_4\text{Ti}_5\text{O}_{18}$) reduces T_c (Curie temperature). Another study by Shimakawa *et al.* [128] related structural disorder to curie temperature. A tolerance factor can be obtained for the layered perovskite structures by considering the perovskite tolerance factor;

$$t = \frac{(R_A + R_O)}{\sqrt{2}(R_B + R_O)}, \quad (3-4)$$

where R_A , R_B , and R_O are the ionic radii of A, B and oxygen ions, respectively. This can be applied to Aurivillius structures. Due to additional Bi_2O_2 layers present in Aurivillius structures, stability region becomes very narrow due to extra structural constraints. Most of the perovskite structures exhibit tolerance factor between 0.77-1.01 [135]. The t value for layered structures is suggested to lie between 0.81-0.89 and with further decreasing as perovskite layers increase [136]. A brief description about octahedron tilting and its notation is discussed below.

Octahedron Tilting: Octahedron tilting reduces the symmetry of the structure. Tilting also has a prominent effect on lattice parameter but it is very difficult to describe it. Attempts are made to explain the effect by including the effect of octahedral into it [137]. However, there are multiple ways the octahedra can tilt and change the environment around the cation. A standard notation has been developed to describe

octahedra tilting in perovskite by Glazer [138]. The notation describes the tilting of MX_6 octahedra about any of the three orthogonal Cartesian axes.

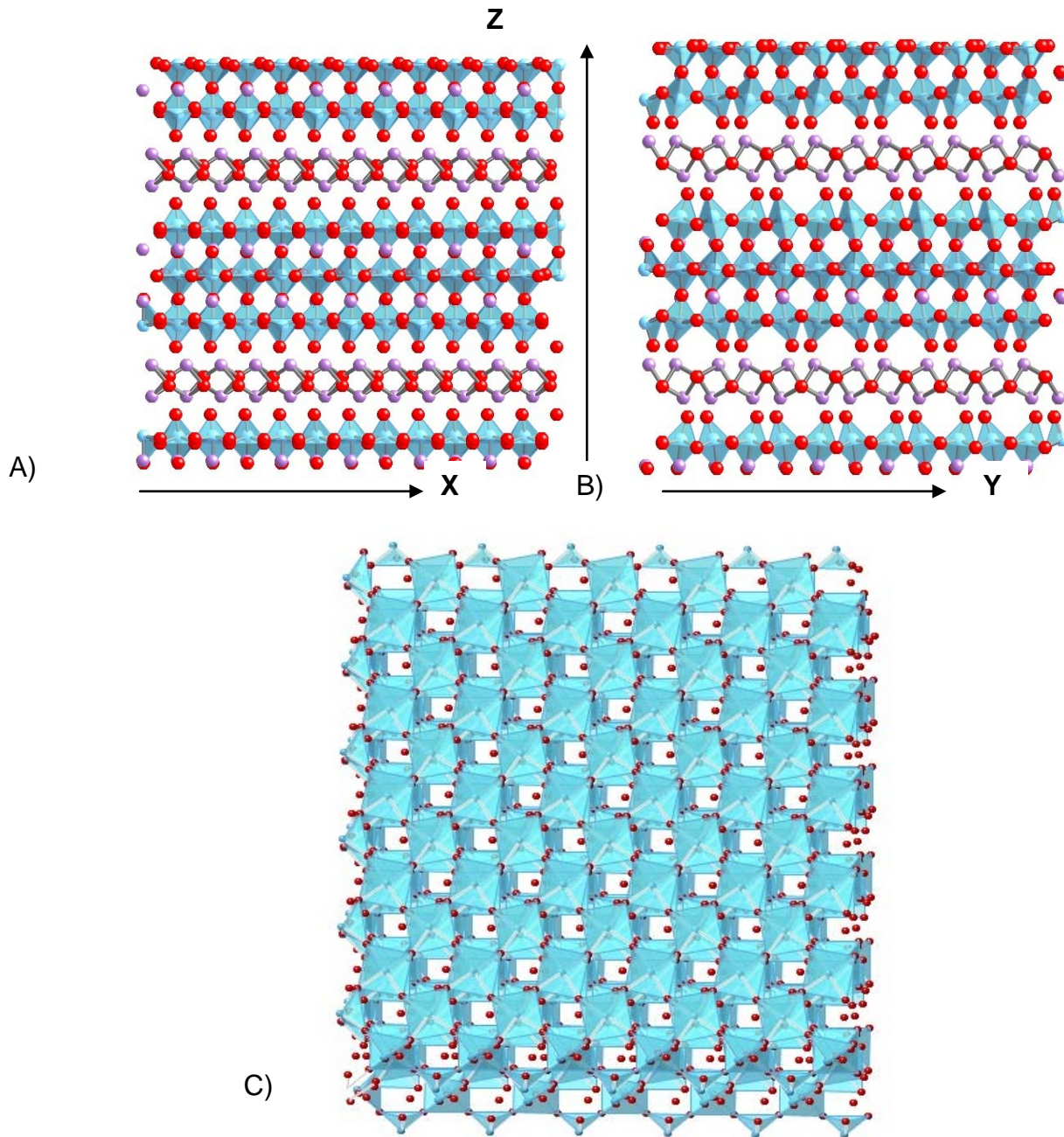


Figure 3-8. Octahedra tilt of 6x6x1 supercell of BIT along A) X-axis [100] B) Y-axis [010] C) Z-axis [001]

The general notation for tilt is used as $a^+b^0c^-$, where a,b,c are the magnitude of the tilt corresponding to [100], [010], and [001] axes. Superscripts depend on the sense of

the tilting of successive octahedra. A + (positive) superscript would denote the same direction (in-phase) tilt of the successive octahedra and a – (negative) superscript implies tilt in the opposite direction (out of phase). A superscript of 0 (zero) denotes no tilting about that axis. There are certain important results that can be inferred from the tilting notation and are given below:

1. Equality of tilts about two or more pseudocubic axes implies equality of axial lengths ($a^+a^+a^+ \rightarrow a=b=c$).
2. Two or more superscripts are '0' or '+', system has orthogonal axes.
3. If two of the superscripts are '-', then respective axes are inclined to each other and third one is perpendicular to both of them.
4. If all there superscripts are '-', then all axis are inclined to one another.

Based on this brief description and Fig. 3-8, it can be inferred that BIT shows $a^0b^-c^-$ octahedra tilting in Glazer notation.

CHAPTER 4 THERMAL TRANSPORT PROPERTIES OF MgO-Nd₂Zr₂O₇

4.1 Introduction

As discussed in the Chapter 1, next generation fuel is one of the solutions of today's energy crisis. In a study of diluents materials for Pu burning in nuclear reactors, MgO along with AlN and ZrN showed promising properties to be a candidate for nuclear reactor applications [139]. Neeft *et al.* [140] also suggested MgO as a potential inert matrix fuel (IMF) material and studied the effect of neutron irradiation in MgO dispersed IMF and modeled the crack propagation in the fuel. Further study by Chauvin *et al.* [141] showed a good behavior by MgO based IMF. Recognizing the importance of MgO, Medvedev *et al.* [15] proposed MgO-ZrO₂ as a candidate IMF material to overcome hydration limitation of MgO. Detailed report on MgO-ZrO₂ as an IMF, is presented in the dissertation of Medvedev [14]. Inspired by this, Yates *et al.* [16] suggested MgO-Nd₂Zr₂O₇ (NDZ) as a candidate material for IMF. The selection of this specific pyrochlore composition (NDZ) is based in part on insights obtained from atomic-level simulations. In particular, Sickafus *et al.* [142] used atomic-level simulation methods to characterize the radiation tolerance of a wide range of pyrochlores (A₂B₂O₇). They found that the radiation tolerance increases significantly as the B ion radius increases. In another atomic level simulation study by Schelling *et al.* [143], it has been reported that the thermal conductivity increases as the B cation radius decreases. Combining these two results with the guidelines suggested by Matzke *et al.* [12], neodymium zirconate, NDZ, is identified as a suitable candidate pyrochlore material.

Interface effects on the thermal properties of MgO-NDZ certer is of primary concern for its potential application as IMF. How the microstructure, interfaces,

volumetric composition governs the thermal transport of the composite is investigated in this chapter. Before investigating interface effects for the MgO-NDZ cercer composite, fidelity of interaction parameters is tested for both the system. MD simulations were run to compute elastic and thermal transport properties of MgO and NDZ. By comparing them with experiment and establishing the veracity of interaction parameters, interface effects are simulated for polycrystals. These polycrystal results are extended to composite system of MgO-NDZ.

4.2 Simulation Set-ups

4.2.1 Thermal Expansion

The simulation set-up to capture thermal expansion consists of cubic arrangement of 6x6x6 or 4x4x4 unit cells in the case of MgO and NDZ respectively. Having 8 atoms in the unit cell of MgO gives a total of 1278 atoms in the simulation supercell. Similarly for NDZ, unit cell having 88 atoms gives 5632 atoms in the simulation set-up. Periodic boundary conditions are applied in all the spatial directions.

4.2.2 Thermal Conductivity

As explained in Sec. 2.11, thermal conductivity is calculated by creating a temperature gradient across the system. After reaching steady state heat flow, thermal conductivity is calculated using Fourier's law (Eq. 2-40). The system can be compared with simple set-up of creating a heat flow across a rod by putting one end at the flame and the other at the cold bath. Schematic of simulation set-up is shown in Fig. 4-1 on the right and a simple cartoon representing heat flow is shown on the left. Simulation set-up has non cubic arrangement with z-axis longer than x and y axes. The set up is chosen to have unidirectional heat flow in z-direction.

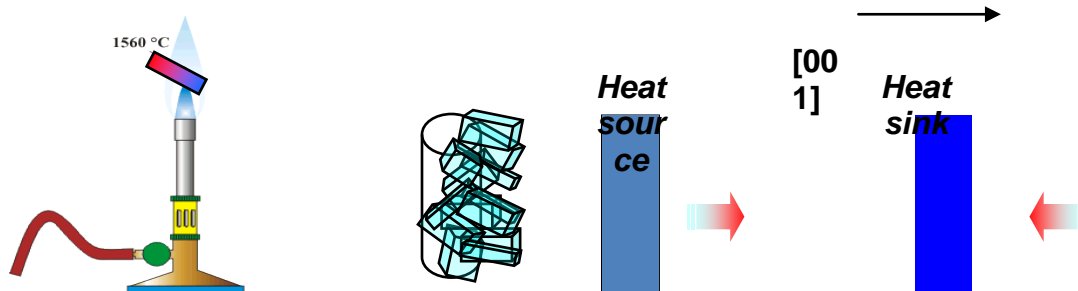


Figure 4-1. Simulation set-up to simulate thermal conductivity

4.3 Results

4.3.1 Thermal Expansion

Simulation set-ups are ran at several temperatures under NPT ensemble (please refer, Sec. 2-9) to compute the coefficient of thermal expansion. After reaching equilibrium state at each temperature, an average of lattice parameter of the system is calculated. The lattice parameters calculated by the simulation are compared with experiment for MgO (Fig. 4-2A) and NDZ (Fig. 4-2B). The lattice parameters for both the system are in quite good agreement with the experiment [144, 145].

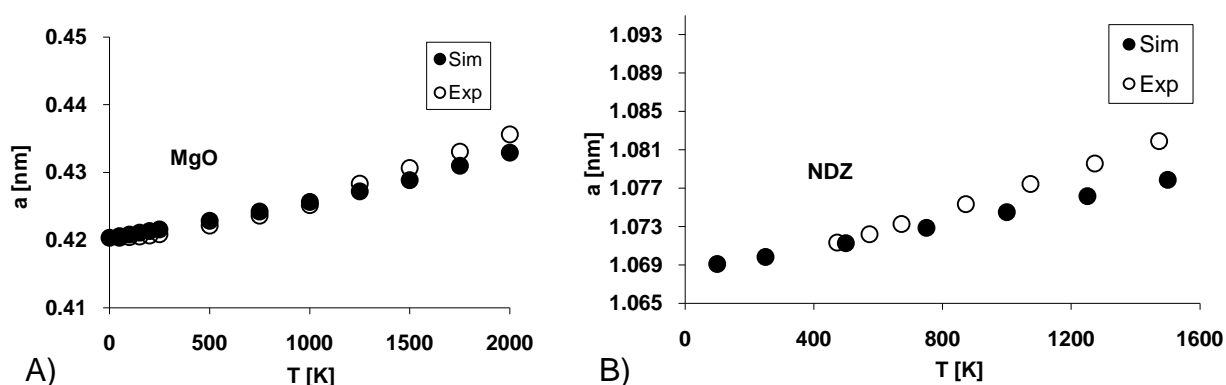


Figure 4-2. Lattice parameter variation with temperature for A) MgO and B) NDZ

Using these simulation values and Eq. 2-39, coefficient of thermal expansion (CTE) is computed for each of the material. CTE for MgO and NDZ from simulation and experiment is shown in Table 4-1. Fidelity of interaction parameters is tested by

comparing the simulated values with experiment. The comparison for MgO is within 5% and for NDZ it is 22% of the experimental value. Such levels of agreement are typical of empirical potentials for oxide materials as shown by other simulation studies [143, 146, 147].

Table 4-1. Coefficient of thermal expansion for MgO and NDZ

Species	Simulation	Experiment
NDZ	$7.4 \times 10^{-6}/\text{K}$	$9.5 \times 10^{-6}/\text{K}$ [145]
MgO	$12.4 \times 10^{-6}/\text{K}$	$13.5 \times 10^{-6}/\text{K}$ [148]

4.3.2 Anharmonic Analysis

The different values of thermal expansion for the simulated and experimental values provide valuable information on the nature of the interatomic interactions. As is well known, the thermal expansion arises from the asymmetry in the interaction potential, *i.e.* from the anharmonicity in the interatomic interactions. An elementary analysis gives the Grüneisen relation for the thermal expansion [29]:

$$\alpha = \frac{\gamma c_v}{3B}, \quad (4-1)$$

where c_v is the specific heat, B is the bulk modulus and γ is the Grüneisen parameter, which is a measure of the anharmonicity of the material. Thus, the reduced values of the simulated thermal expansions are attributed to the interatomic interactions being insufficiently anharmonic and/or the bulk modulus being too high.

This conclusion has important implications for the thermal transport properties, because the thermal conductivity is also determined by the anharmonicity of the interactions. In particular, in most electrically-insulating materials the dominant

scattering mechanism is phonon-phonon scattering. Such scattering would be completely absent if all of the interactions were harmonic. Using a perturbation expansion of the interatomic potential to third order, thereby including the lowest anharmonic terms, Liebfried and Schloemann [149] showed that the thermal conductivity is inversely proportional to the square of the Grüneisen parameter:

$$\kappa \sim \frac{24}{10} \frac{\sqrt{4}}{\gamma^2} \left(\frac{k_B}{h} \right)^3 Mv \frac{\theta^3}{T}, \quad (4-2)$$

where k_B is the Boltzmann constant, h is the Planck constant, v and M are the volume and the mass per atom. The only two materials constants that enter into Eq. 4-2 are the Debye temperature, θ , and the frequency-averaged Grüneisen parameter, γ . From this relation, it is clear that the thermal conductivity is inversely proportional to γ . Through their dependence on the Grüneisen parameter, a simple empirical relationship between the thermal conductivity and thermal expansion is shown as [150]:

$$\alpha^2 \kappa = \chi \frac{\theta^3 C_v^2}{B}, \quad (4-3)$$

The constant χ contains all of the non-materials constants in Eqs. 4-2 and 4-3.

Table 4-2 shows the values of Θ_D and C_p for MgO and NDZ is determined using GULP (General Utility lattice Program) [151, 152] and compared with the experimental values.

Table 4.2. Comparison of Debye temperature and C_p calculated using GULP with experiment. $\Gamma = G_{sim}/G_{expt}$, where $G = \Theta_D^3 C_p^2$

Material	Θ_D (K)		C_p (J/mol-K)		□
	Sim.	Exp.	Sim.	Exp.	
MgO	830	946 [153]	38.77	34.82 [153]	0.83
Nd ₂ Zr ₂ O ₇	549	489 [154]	207.54	232.70 [154]	1.13

Moreover, the experimental and calculated values of $G=\Theta_D^3 C_p^2$, analogous to the combination in Eq. 4-3 are within 20% for both materials. After merging C_v and Θ_D with other constants Eq. 4-3 becomes

$$\kappa = \frac{\chi'}{\alpha^2 B} \quad (4-4)$$

where $\chi' = \chi \theta^3 C_v^2$. From Eq. 4-4, a relationship between experimental and simulation thermal conductivity comes out to be:

$$\kappa_{\text{sim}} = \kappa_{\text{expt}} (\alpha_{\text{expt}}/\alpha_{\text{sim}})^2 (B_{\text{exp}}/B_{\text{sim}}) \quad (4-5)$$

In Eq. 4-5, $(\alpha_{\text{expt}}/\alpha_{\text{sim}})^2 (B_{\text{exp}}/B_{\text{sim}})$ ratio is termed as “correction factor”. After dividing the simulated value with the correction factor, comparison with experimental value is done. The bulk modulus for MgO and NDZ from simulation for these potentials came out to be 170 GPa and 167 GPa respectively at 0 K. The corresponding experimental room-temperature values for single crystals are 155 GPa and 159 GPa, which are quite consistent [155, 156].

From these data, Eq. 4-5 predicts $\kappa_{\text{sim}} = 1.02 \kappa_{\text{expt}}$ for MgO and $\kappa_{\text{sim}} = 1.61 \kappa_{\text{expt}}$ for NDZ; that is, simulations of the thermal conductivity of MgO should match the experimental results rather well, while the simulations should significantly overestimate the thermal conductivity of NDZ.

4.3.3 Thermal Conductivity

As described in section 4.2.2, simulation is set up to generate unidirectional heat flow. By generating temperature gradient, conduction is simulated and then calculated by using Fourier’s law, Eq. 4-6

$$J = -\kappa \frac{dT}{dx} \quad (4-6)$$

The key determinant of thermal conductivity is the mean free path of the phonons before they scatter from each other or from other components of the microstructure. If the system size in the direction of heat flow is smaller than the phonon mean free path, then the intrinsic anharmonic properties of the system will not be probed completely. This regime is known as the Casimir limit. It is thus no surprise that previous studies have also shown that the accuracy of the simulations of the thermal conductivity depends significantly on the length of the simulation cell. In a previous study by Schelling *et al.* [157], a finite size scaling approach is used to determine the thermal conductivity of the material.

4.3.4 Finite Size Analysis

This approach, which is based on the inverse additivity of contributions to the mean free path yields (for details, please refer Eq. 2-47):

$$\frac{1}{\kappa} = \frac{1}{\kappa_{\infty}} + \frac{4P}{L_z} \quad (4-7)$$

where κ is the thermal conductivity determined from simulation, κ_{∞} is the thermal conductivity in the infinite system-size limit (i.e., the best estimate of the ‘true’ thermal conductivity of the material), L_z is the length of the simulation cell and P is a constant. Equation 4-7 thus suggests that a plot of $1/\kappa$ vs $1/L_z$ should be linear, and that the thermal conductivity of an infinite system can be obtained by extrapolating to $1/L_z = 0$. Figure 4-3 shows such analysis for MgO and NDZ at 573 K. By using the above described system size analysis at various temperatures, the temperature dependence of thermal conductivity is extracted for both MgO and NDZ.

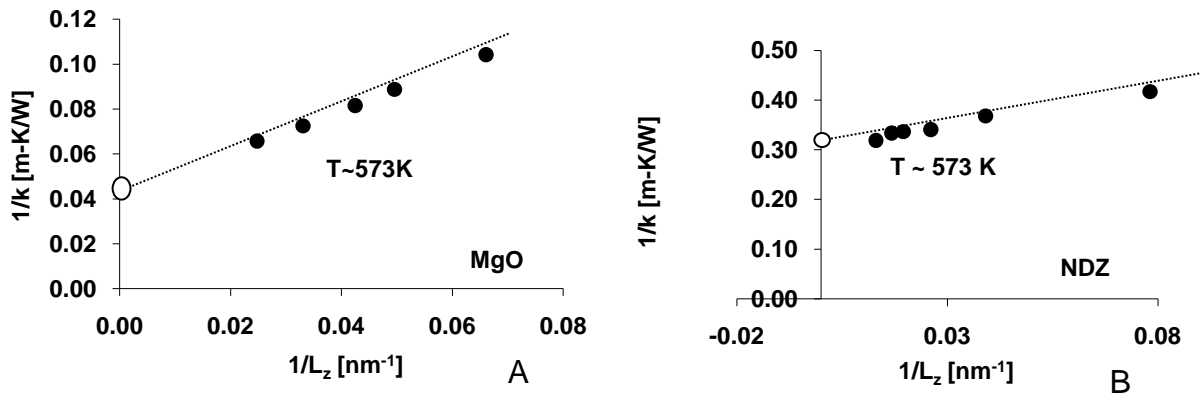


Figure 4-3. System size effect on thermal conductivity A) MgO B) NDZ

Finite-size scaling analysis can lead to a significant increase in the simulated value of thermal conductivity, as is illustrated in Fig. 4-3. If only a single simulation had been performed for the shortest simulation cell ($L_z = 15.3$ nm for MgO and $L_z = 12.80$ nm for NDZ), then the estimated thermal conductivities would be less than one-fourth of the best estimated value.

4.3.5 MgO: Thermal Conductivity

Figure 4-4 compares the best estimate of the thermal conductivity determined from simulation and finite-size scaling analysis, with the experimental data for MgO. The data of Cahill (open circles) [158] is for a high-quality single crystal thin film, while the polycrystalline data (open squares) is for coarse-grained polycrystal [159]. The experimental polycrystalline data is systematically lower than the experimental data for a single crystal by a small amount. While physically this is reasonable since the polycrystals contain grain boundaries, and possibly other defects arising from processing, all of which provide additional scattering mechanisms, this difference could also simply be statistical in origin [31].

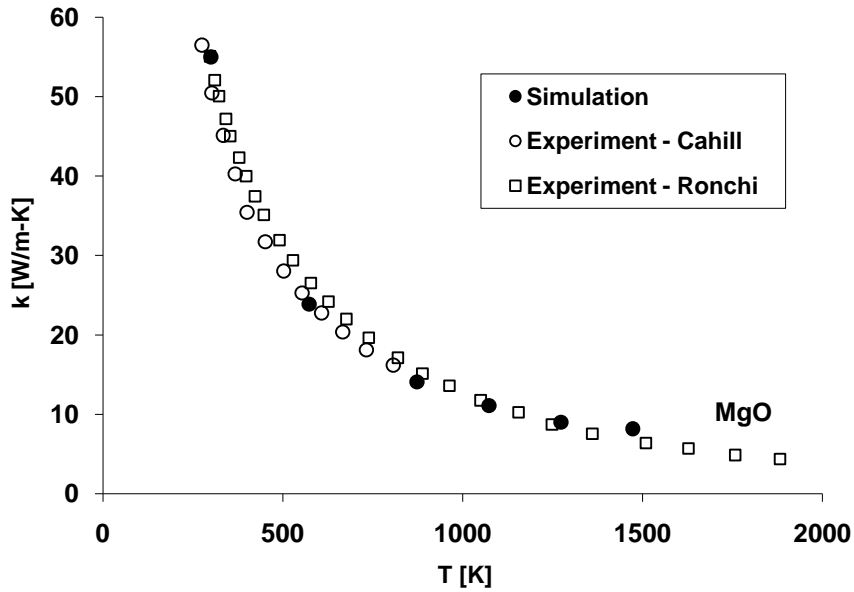


Figure 4-4. Thermal conductivity data of MgO: experiment data for single crystal thin film (open circle) [158], experiment polycrystal data (open square [159]) and simulation data (solid circle).

The simulated data (solid circles) agreed very well with the single crystal experimental data. Had a finite size analysis not been performed, these values would have been significantly lower and would not have agreed with the experimental values. That the experimental and simulated values are in such good agreement provides validation for the harmonic analysis described in the Sec. 4.3.2, which predicted that they should agree within 2%.

4.3.6 NDZ: Thermal Conductivity

The anharmonicity analysis yielded a multiplicative correction factor of $1/1.61 = 0.62$ for NDZ. Thermal conductivity values are computed using the simulation method as described in Sec. 2.11. The simulated values of thermal conductivity are modified using the correction factor. Figure 4-5 shows both the uncorrected and corrected values for the thermal conductivity of NDZ. While the uncorrected values are, as expected,

consistently higher than the experimental values, the corrected values are much more consistent with the experimental results [160].

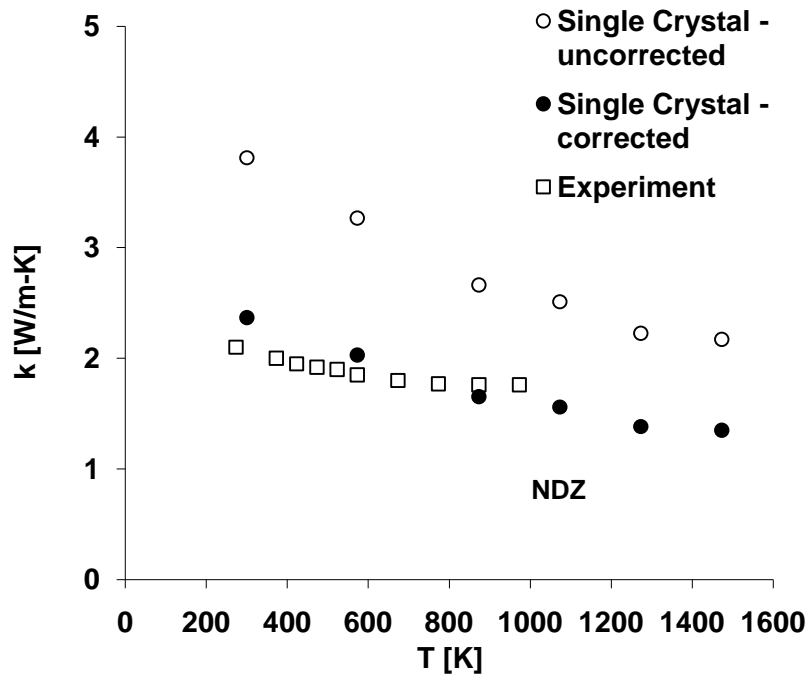


Figure 4-5. Thermal conductivity of $\text{Nd}_2\text{Zr}_2\text{O}_7$: uncorrected single crystal simulation values (open circle), corrected single crystal values (solid circle) and experimental polycrystal values (open square) [160]

Both the thermal conductivity results for MgO and NDZ are done on single crystals. The difference between experiment and simulation results, besides other reasons is because experimental system has defects. To illustrate the effect of grain boundaries (GBs), simulations on polycrystals are performed and analyzed.

4.4 MgO-NDZ: Polycrystals and Composite

Defects are an essential part of any material. In nuclear reactor, fuel pellets have grain boundaries as one of the primary defects. The working temperature in the reactor ranges from 800 K-1500 K. Grains in the nuclear fuel undergoes structural changes and that leads to changes in the thermal and mechanical properties of the fuel. It is

important to know how these interfaces affect thermal transport in the fuel. That can be understood if the effects of interfaces are characterized in the fuel. Since at atomic level interface effects are enhanced, atomic level simulations provide an ideal vehicle to characterize the interface effects. To characterize the effect of grain boundaries the thermal transport properties of MgO and NDZ polycrystals and MgO-NDZ composites are simulated. Interface effects are enhanced at smaller grain size level. It is possible to extend the size into the tens of nanometers range but, due to intrinsic computational limitations, it is not possible to extend the range to microns and tens of microns grain size, present in typical ceramic materials. To extend the results for larger grains, a simple analysis model is used and results are compared with experiment results.

The following section will outline the method used in this work to generate polycrystal and composite structures.

4.4.1 Polycrystal Structure

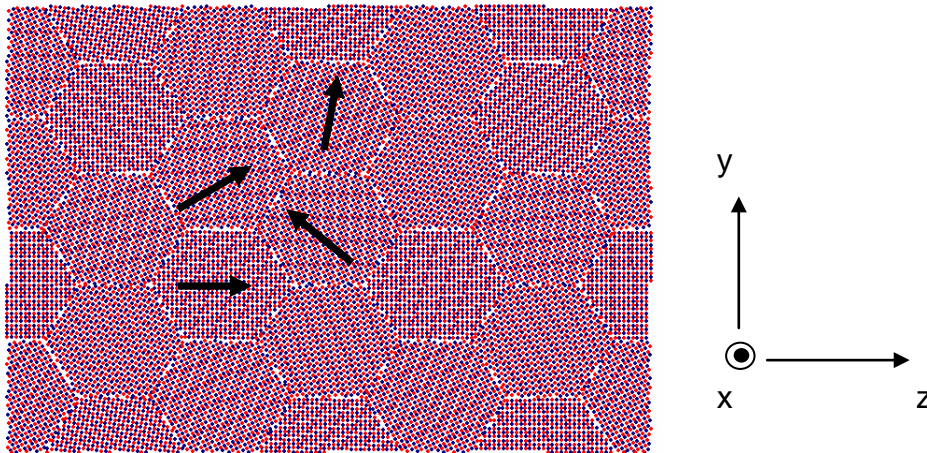


Figure 4-6. MgO polycrystal ~ 3 nm grain size; black arrows showing orientation of the grain

Interface effects can be estimated using 2-D textured polycrystals. They provide an efficient alternate to 3-D grains to capture interface effects. A simple code has been developed to generate 2-D polycrystals as shown in Fig. 4-6.

The polycrystal is textured with all the grains being parallel to the [100] direction. For both materials, MgO and NDZ, 24 perfectly hexagonal grains are filled with perfect crystal with the [100] directions oriented in almost random directions with respect to the horizontal x-axis, with the stipulation that all grain-boundary (GB) misorientations should be $>15^\circ$, thereby reducing the tendency for grain coalescence. The grain-boundaries in these polycrystals are thus a reasonably random selection of $\langle 001 \rangle$ tilt boundaries. Periodic boundary conditions are applied such that there are no additional interfaces at the boundaries. The whole process of generating polycrystal can be summarized as

1. 24 hexagonal grains of equal size were created by specifying their centers but all of them are empty at this step.
2. Each grain was oriented in a way that no neighboring grains form low angle GB.
3. Each grain is filled with the unit cells of the material (MgO or NDZ).
4. Each grain-atom is screened and are removed if they are closer to neighboring grain centers.
5. All the grains are combined to make the polycrystal.
6. Any two atoms, with a distance less than a specified cut-off distance are identified and termed as bad atoms.
7. Charge of each grain is calculated and maintained to zero by removing bad atoms from the grain.
8. Still if system is not neutral, bad atoms are removed to achieve charge neutrality.
9. If system is charge neutral but still have bad atoms, bad atoms are removed as a formula unit. For example, for each Zr of NDZ, two nearest oxygens are removed to keep the neutral charge of the system.

4.4.2 Composite Structure

Depending upon the connectivity of constituent phase of the composite, it can be one-, two-, or three-dimensionally continuous. A simple scheme to classify the connectivity for two-component system is presented by Newnham *et al.* [161]. All the possible connectivity of two-component composite system is shown in Fig. 4-7. Among the ten different connectivity patterns, 3-3 composites are extremely rare and 0-3 is very common for particulates in a matrix and 1-3 for aligned fiber-matrix composites.

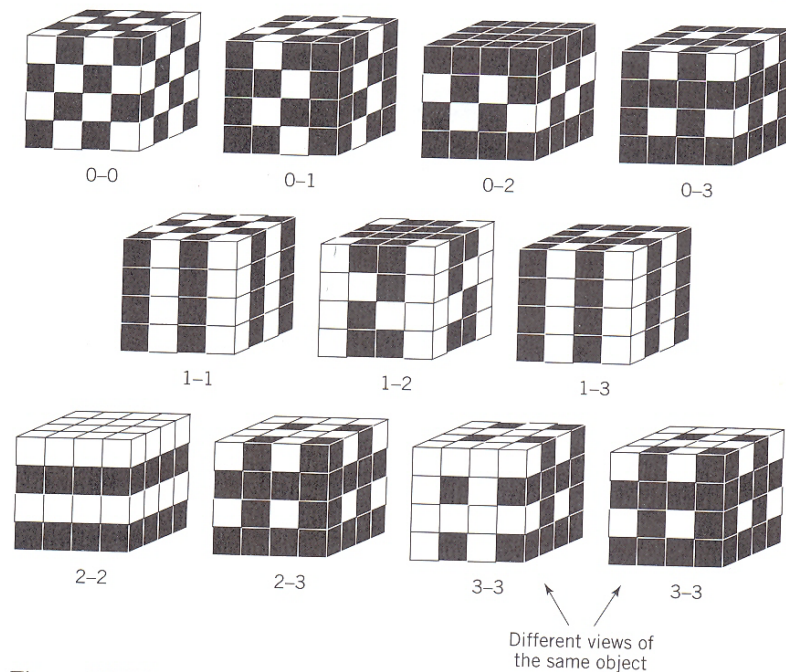


Figure 4-7. Different connectivity patterns for two-component composite system [162].

To understand this notation, a simple method is used:

1. First number represents the connectivity of white
2. Second number represents the connectivity of black

Black and white nomenclatures are used here to define two different materials because it is easier to follow Fig.4-7 with the convention. For example, 1-1 composite means, only 1-dimension connectivity for both white and black blocks. As shown in Fig.

4-7, 1-1 composite has only vertical alignment for both white and black. Another example of 2-3 composite means, white is continuous in 2-dimensions and black in all 3 dimensions. For the textured composite, the composite will exhibit at least 1-1 connectivity.

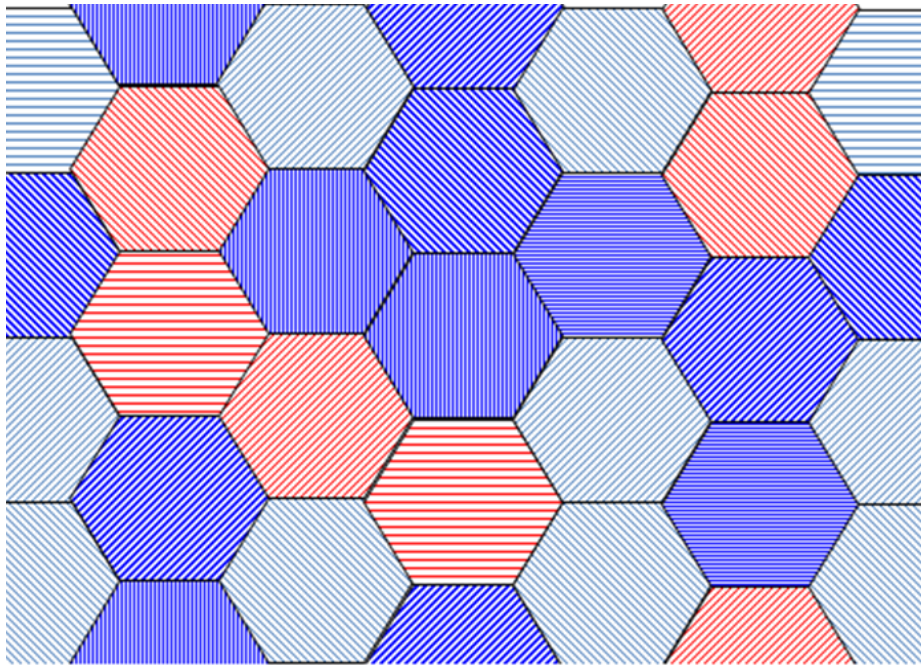


Figure 4-8. MgO (blue)-NDZ (red) composite (2-1 composite)

A Simple schematic representation of composite structure is shown in Fig. 4-8. Composite structure can be either MgO connected and/or NDZ connected or not connected. Based on the experimental insight by Yates *et al.* [16], same volumetric composition of MgO and NDZ gives micro-structural dependent temperature dependence of thermal conductivity.

Similar to the procedure used to build polycrystals, composites are built. Slight changes are made because of the difference in lattice parameters of MgO and NDZ. The method to generate composite is as follows:

1. 24 hexagonal equal size grains were created by specifying their centers but all of them are empty at this step.

2. Each grain was oriented in a way that no neighboring grains form low angle GB.
3. Atomic coordinates of MgO atoms are changed according to NDZ lattice parameter. For example, (1, 0, 0) coordinate corresponds to $\sim (0.39, 0, 0)$.
4. Based on the connectivity, grains are assigned to MgO or NDZ..
5. Each grain is filled with the corresponding material unit cells.
6. Atoms with a smaller distance than a specified cut-off are termed as bad atoms for each grain
7. Grains are made charge neutral by removing bad atoms
8. Still if system is not neutral, bad atoms are removed to achieve charge neutrality.
9. Grains are combined and composite is built.

Composite structures are equilibrated and high energy atoms are screened. These high energy atoms are removed from the system. Equilibrated composite structures are used to compute thermal conductivity and capture interface effects.

4.4.3 Interfacial Effect on Thermal Conductivity

As described in section 4.4.1, polycrystals of MgO and NDZ structures are generated. Thermal transport properties are calculated using the same approach as used for the single crystals. The effect of system size is expected to be much less important for such fine-grained polycrystals because the dominant mechanism should be phonon/grain boundary rather than phonon/phonon scattering. Simulations on the system shown in Fig. 4-6 and a system with the same microstructure and grain size, but twice the length (formed by simply putting two simulation cell shown in Fig. 4-6 end to end), gave thermal conductivity values within 5% of each other, which is within the statistical errors of the simulations.

The anharmonicity analysis predicted the thermal conductivities of the single crystals from simulations would be overestimated by 2% for MgO and 62% for NDZ. Anharmonic correction factors are used in predicting the thermal conductivity of MgO and NDZ

polycrystals. In this step, the thermal expansion and bulk modulus are taken as essentially microstructure independent. However, within the approximation made in separating the contributions in the polycrystal thermal conductivity from that of grain interior and grain boundary, the accuracy may not be sufficient to consider more careful analysis.

As Figs. 4-9 and 4-10 show, the calculated thermal conductivities of the fine-grained polycrystals of MgO and NDZ are considerably smaller than their single-crystal counterparts. The thermal conductivity for polycrystalline NDZ shows a smaller reduction from the single-crystal value than does polycrystalline MgO (note the difference in scales); this smaller reduction is attributed to the already much smaller mean free path of phonons in NDZ as compared to MgO. Also, for both systems, the effect is considerably larger at lower temperatures, at which the phonon mean free path is longer.

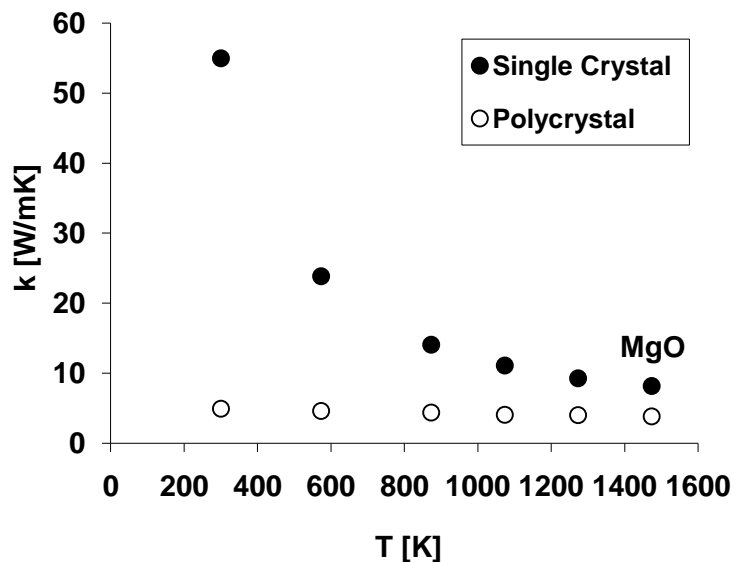


Figure 4-9. Comparison of thermal conductivity of MgO: single crystal (solid circle) and 3 nm polycrystal (open circle).

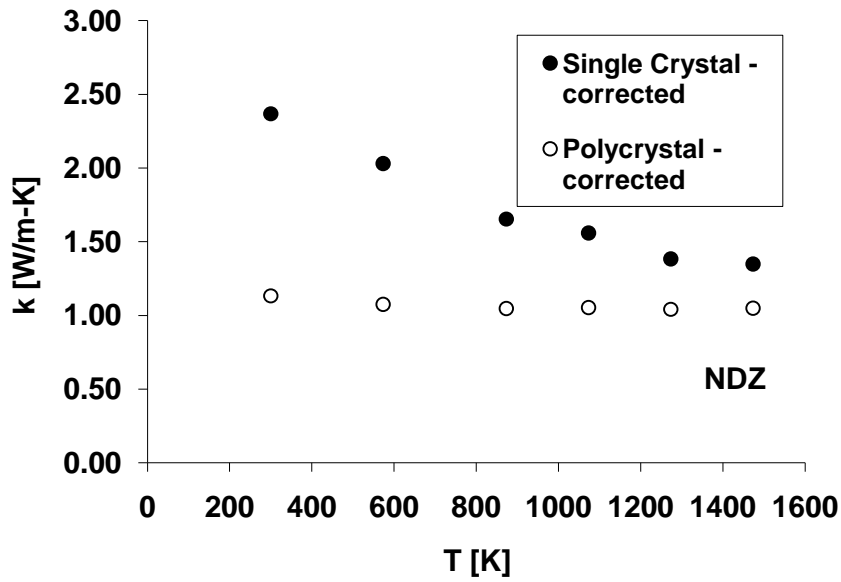


Figure 4-10. Comparison of thermal conductivity of NDZ: single crystal (solid circle) and 3 nm polycrystal (open circle).

Using a simple model in which the polycrystal is assumed to be describable in terms of a volume of bulk with thermal conductivity (κ_0) and a volume of grain boundary with interface conductance (G) (all grain boundaries being assumed to be physically the same), Yang *et al.* [19] derived a simple relation for the dependence of the thermal conductivity, κ , of a polycrystal on grain size, d:

$$\kappa = \frac{\kappa_0}{\left(1 + \frac{\kappa_0}{Gd}\right)} \quad (4-8)$$

Using Eq. 4-8, estimates for G are extracted; the result is shown in Fig. 4-11 for both materials, MgO and NDZ. As for other materials that have been studied experimentally and/or in simulation, G increases with temperature, reflecting the enhanced anharmonic coupling of weakly coupled phonon modes across the interfaces [163].

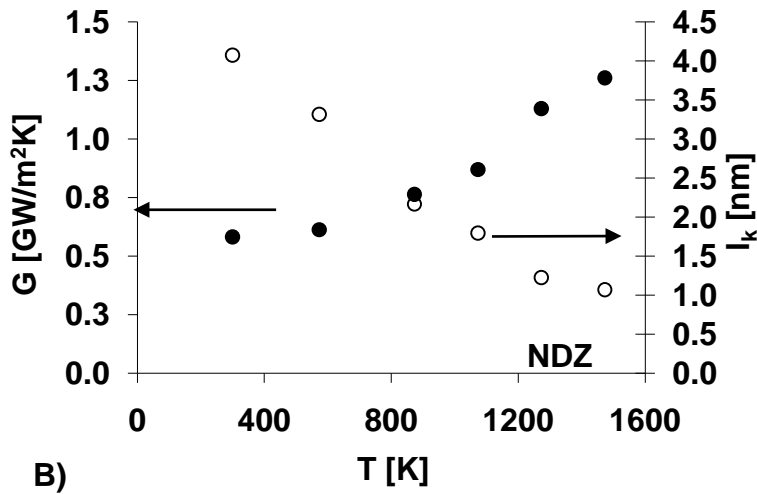
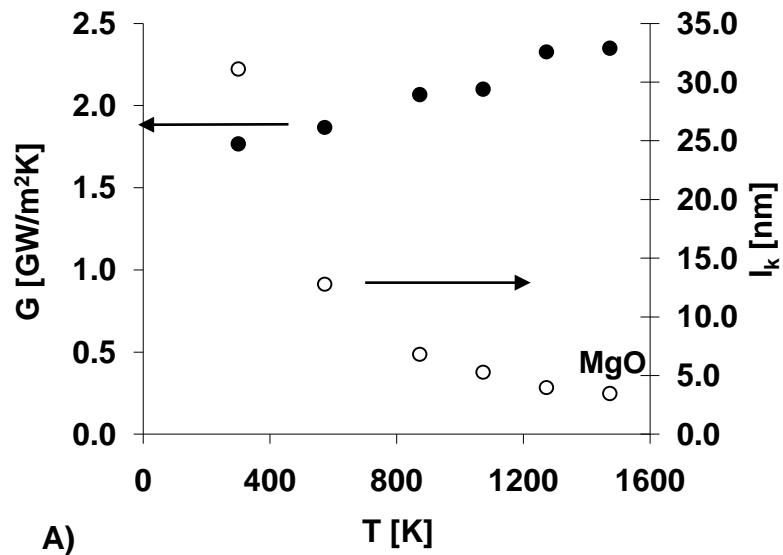


Figure 4-11. Temperature dependence of the interfacial conductance, G (solid symbols) and Kapitza length, l_k (open circles) for A) 3 nm polycrystalline MgO and B) 3 nm polycrystalline NDZ.

Because the thermal conductivity and G are in different units, it is not possible to compare them directly. To make a better comparison, a new variable named Kapitza length is defined as

$$l_k = \kappa_0 / G \tag{4-9}$$

The Kapitza length (l_k) is a measure of the length of perfect crystal that offers the same resistance to heat transport as the interface *i.e.* the larger the value of l_k , the larger the thermal barrier offered by the interface. From Fig 4-11, l_k goes from 30 nm at 300 K to ~3 nm at 1473 K for MgO. The effect is less dramatic in NDZ, with l_k decreasing from 4 nm at 300 K to 1.75 nm at 1473 K. These decrease in MgO and NDZ are consistent with the trends seen previously for UO_2 [150] and diamond [164] in both of which, l_k decreases with temperature for both materials.

4.4.4 Grain Size Dependence on Thermal Conductivity

Having determined G , Eq. 4-8 was used to predict the grain-size dependence of the thermal conductivity. Figure 4-12 shows the calculated grain size dependence of the thermal conductivity at 300 K and 573 K for MgO and NDZ, normalized to the corresponding single crystal values; thus in both cases, the large grain size limit is $\kappa/\kappa_0=1$. In the absence of any experimental data on the thermal conductivity of MgO or NDZ as a function of grain size against which to compare these trends, Fig. 4-12 includes the experimental results of Yang *et al.* for yttria-stabilized zirconia (YSZ) [19]. Despite the considerable difference in materials and microstructures (textured vs. random polycrystal), the simulation data is broadly consistent with the experimental data. In particular, the agreement between the simulation results for NDZ and the experiments for YSZ is remarkably good; this agreement probably arises from the fact that they both are low thermal conductivity materials with fluorite-related crystal structures. After gaining insight at the effect of homogeneous interface on thermal transport, study was extended to include composites.

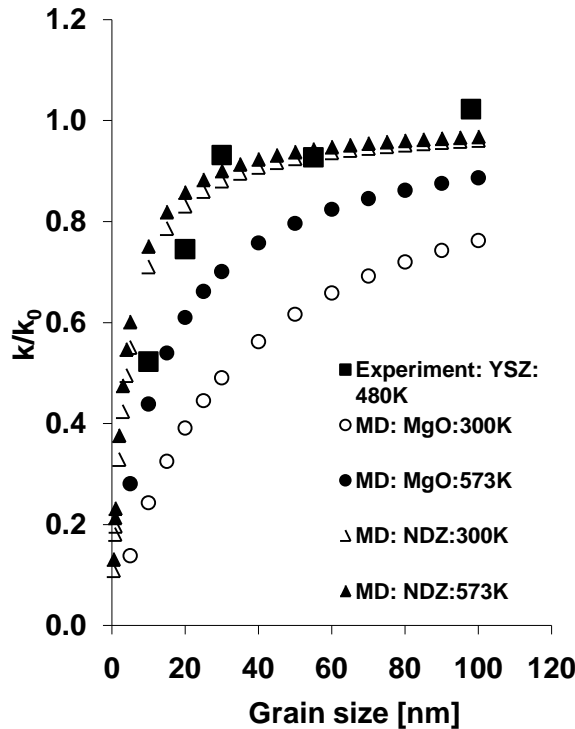


Figure 4-12. Predicted grain-size dependence of the normalized thermal conductivity of MgO (solid and open circle) and NDZ (solid and open triangle) polycrystals compared with experimental results of YSZ (solid square) [19]

Polycrystal simulations provided information for MgO-MgO and NDZ-NDZ interfaces. To understand the nature of MgO-NDZ interface, composite system with different connectivity is generated. Section 4.4.5 details the information on simulation studies done on MgO-NDZ composites.

4.4.5 Thermal Conductivity of MgO-NDZ Composite

Based on experimental investigation by Yates *et al.* [16], a volumetric ratio of 60-40 (MgO-NDZ) was suggested for the composite for the simulation study. To achieve the similar ratio, 10 grains were selected as NDZ and remaining 14 were MgO grains. Polycrystal investigations gave us insight into interfacial effects of both the constituents separately. Interfacial effects were larger than grain size itself at this sub nano size level

and that led to the assumption that no additional interface effects can be seen in the composite.

A simple model based on volumetric composition is used to predict the thermal conductivity of composite. The predicted value of thermal conductivity is given by:

$$\kappa = x_{NDZ} \kappa_{NDZ, poly} + x_{MgO} \kappa_{MgO, poly} \quad (4-9)$$

where x_{NDZ} gives the volumetric composition of NDZ (For example, in this case 10/24 is for NDZ) and $\kappa_{poly, NDZ}$ is the thermal conductivity of the same size NDZ polycrystal. Similarly values are defined for MgO grain component.

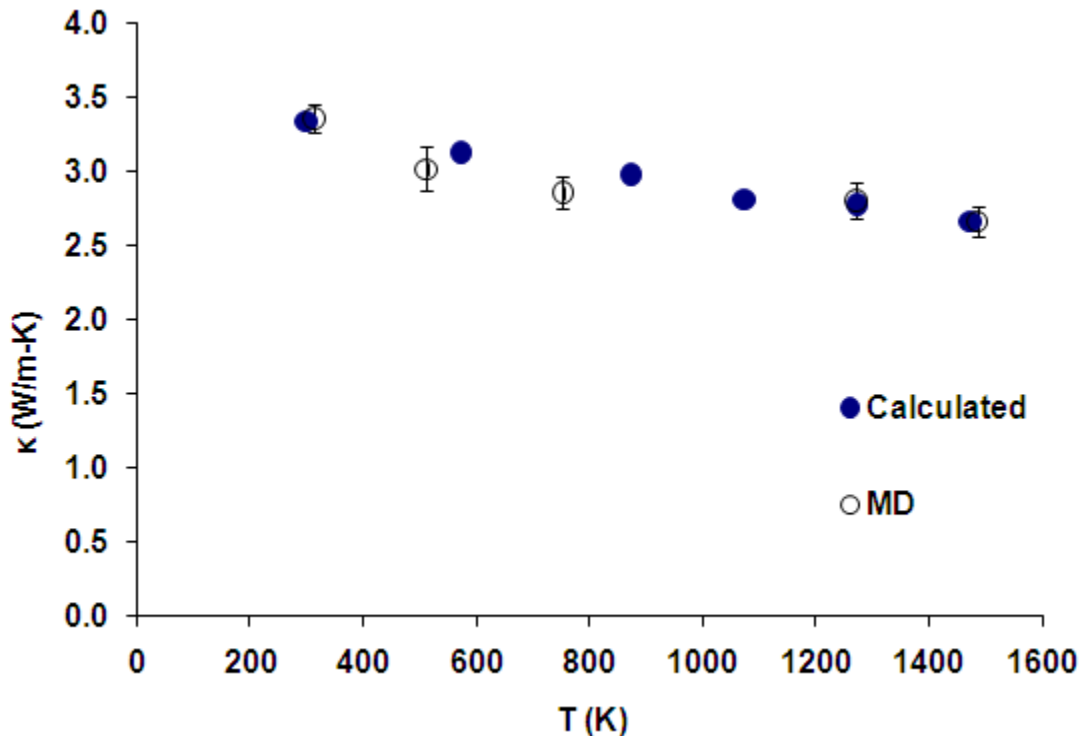


Figure 4-13. Comparison of thermal conductivity of 60-40 MgO-NDZ composite with predicted value

Based on the simulation results, no additional interface effects are observed in the composite. This can be attributed to the limitation of current status of simulation power.

4.5 Discussion

The atomic-level simulation method has provided an important insight into the MgO-NDZ system. The fidelity of interaction parameters for MgO and NDZ was tested separately. The interaction parameters for MgO have shown better fidelity with experiment than for NDZ.

Finite size and anharmonic analysis tools are used to correct the simulated thermal conductivity values. The modified values after the analysis have shown a good comparison with the experiment. After establishing single crystal results, interfaces are introduced into the system.

A simple program is written to generate 2-D textured polycrystals. Very fine grain size enhanced the interface effect. Interfacial conductance for MgO and NDZ polycrystals showed correct temperature dependence. Calculation of Kapitza length has shown that interface effects are as big as grain itself for both the materials: MgO and NDZ. A simple analysis is used to extrapolate the effect of grain size and compared with the experiment study. Both the materials showed the independence of the thermal conductivity on the grain size beyond ~100 nm. That implies the limiting effect of interfaces for bigger grains.

A simple analysis based on the volumetric composition of the individual grains is used to predict the thermal conductivity of the composite. Thermal conductivity values of the polycrystals are used to predict the composite thermal conductivity. Comparable results for predicted value and MD results showed that thermal conductivity depends only on the volumetric composition of the composite and not the microstructure at very fine grain size level.

CHAPTER 5 THERMAL TRANSPORT PROPERTIES OF MgAl_2O_4

5.1 Introduction

Based on the guidelines for inert matrix materials (for details, please refer Section 1.5) proposed by Matzke *et al.* [12], magnesium aluminate spinel MgAl_2O_4 is among the potential inert matrix materials for minor actinide incineration. In particular, MgAl_2O_4 is very tolerant to neutron irradiation [165, 166]. Its ability to tolerate radiation damage is attributed to i) a very high recombination rate of Frenkel pairs [165] and, ii) the ability to tolerate significant intrinsic cation antisite disorder [167]. The property of cations interchanging their sites in the spinel structure is called *inversion*. It has been well established that cation arrangement plays an important role in the material properties. For example, the elastic properties change with cation arrangement in spinel [168, 169], and the bulk modulus of MgTi_2O_5 changes with cation ordering [170]. It has also been found that with increasing temperature MgAl_2O_4 undergoes inversion [171-173]. A deeper understanding of the effects of inversion on the thermo-elastic properties of MgAl_2O_4 is highly desirable before it can be fully assessed as a potential IMF material. The experimental investigation of the effects of inversion on MgAl_2O_4 faces two big challenges:

1. It is hard to control inversion during the synthesis process.
2. It is impossible to separate out the effect of temperature from inversion.

Both of these challenges are easily overcome in atomic level simulation. MD is chosen as an ideal vehicle to perform the simulations to capture the effect of inversion on MgAl_2O_4 properties. One of the key performance metrics of any IMF material is

thermal conductivity; therefore an important question here is: *How does inversion affect the thermal conductivity of MgAl₂O₄?*

5.2 Selection of Inverted Structure

Conventional MD simulation methods and lattice dynamics are used to investigate the effect of inversion on mechanical and thermal transport properties of MgAl₂O₄. Interaction parameters are taken from Table 2-2.

As discussed in Chapter-3, each unit cell of MgAl₂O₄ contains 8 Mg, 16 Al and 32 O ions. For the MD simulation study, a cubic arrangement of 4x4x4 unit cells for a total of 3584 atoms is formed. For the lattice dynamics calculations in GULP a 2x2x2 system with 448 atoms is formed. This large system size benefited us by giving us more choices for the degree of inversion. There are 2 simple ways to create an inverted structure in MgAl₂O₄:

- i) Direct interchange of Mg and Al;
- ii) Al can move to a vacant tetrahedral site and Mg to a vacant octahedral.

A first-principles electronic structure study by Gupta [174] has shown that direct cation exchange is energetically more favorable. Therefore randomly selected Mg and Al atoms were simply exchanged to generate the inverted structures. Since there is no experimental information on possible ordering in inverted structures available, ~7000 structures were generated for each inversion value via random cation interchange. Three lowest energy structures were identified and used them for the subsequent simulations. Figure 5-1 captures the distribution of structural energy among the generated structures for the same inversion value. The x-axis of Fig. 5-1 covers the whole energy range spanned by generated structures for the inversion values $i=0.0625$ and $i=1.0$, and the y-axis shows the number of structures having that energy. The

energy of the structure increases from left to the right on the x-axis. Thus, structures having energy in the left extreme of the graph are picked. The large number of structures for each inversion maximizes the chances of identifying the energetically most favorable structure.

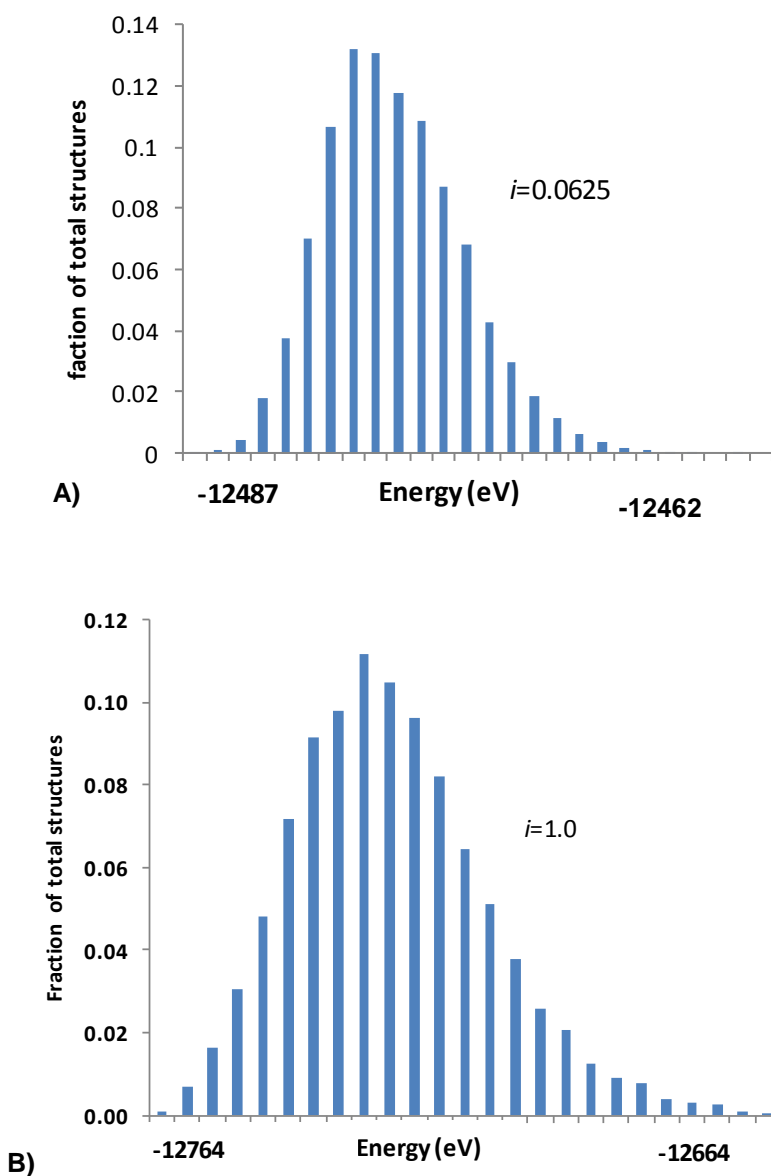


Figure 5-1. Distribution of energy as a function of cation arrangement for the inversion value of A) 0.0625 B) 1.0

After selecting structures for each inversion, pair distribution function (PDF) for each cation is investigated. PDF provides structural insight with a very simple and easy analysis method. PDF for normal ($i=0$) is shown in Fig. 5-2A, and it shows that first Mg-Al neighbor is beyond 3 Å. As inversion is introduced in the system, the height of the peaks is decreasing. A comparison between the PDF of Al-Mg for $i=0$ and 0.125 is shown in Fig. 5-2B. They have very similar peaks but the actual values have gone down by more than 20% and peaks are more spread out for $i=0.125$.

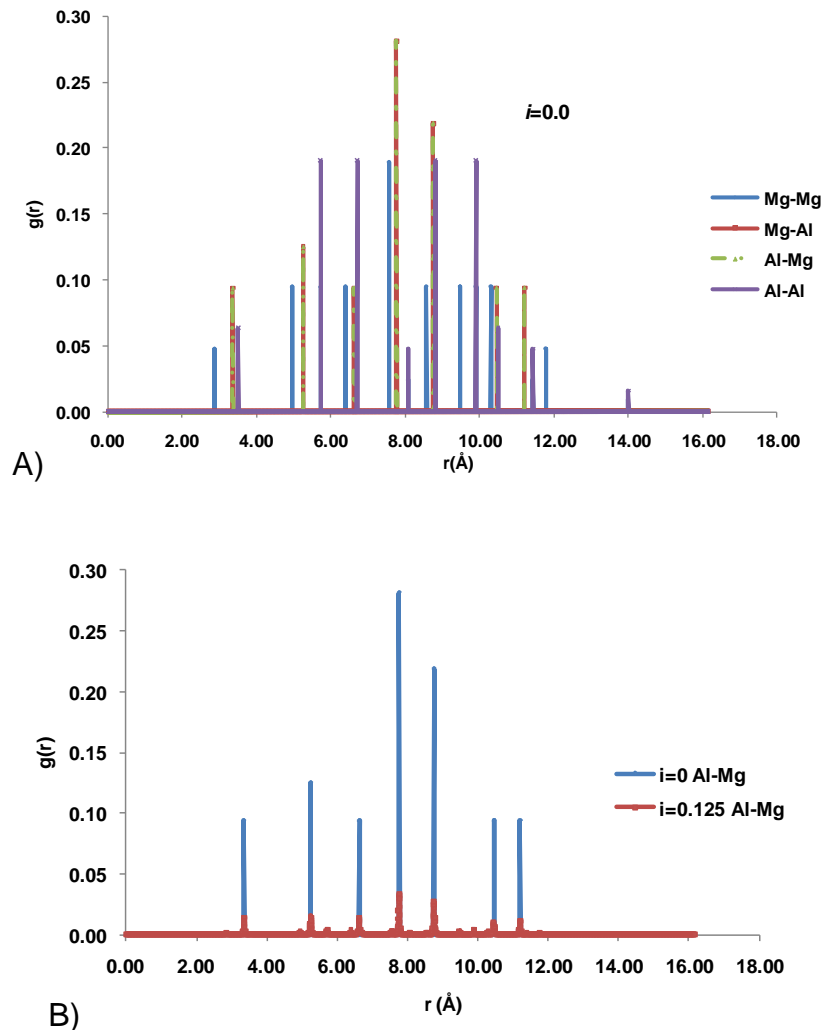


Figure 5-2. PDF for A) normal spinel B) comparison of Al-Mg PDF for $i=0$ and $i=0.125$

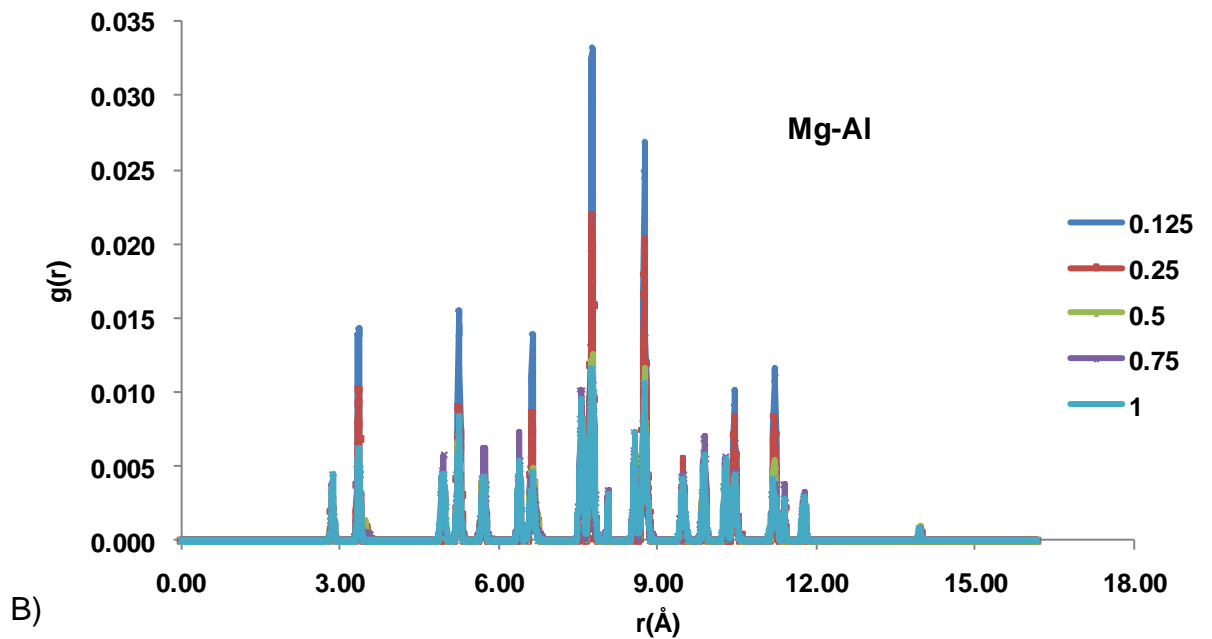
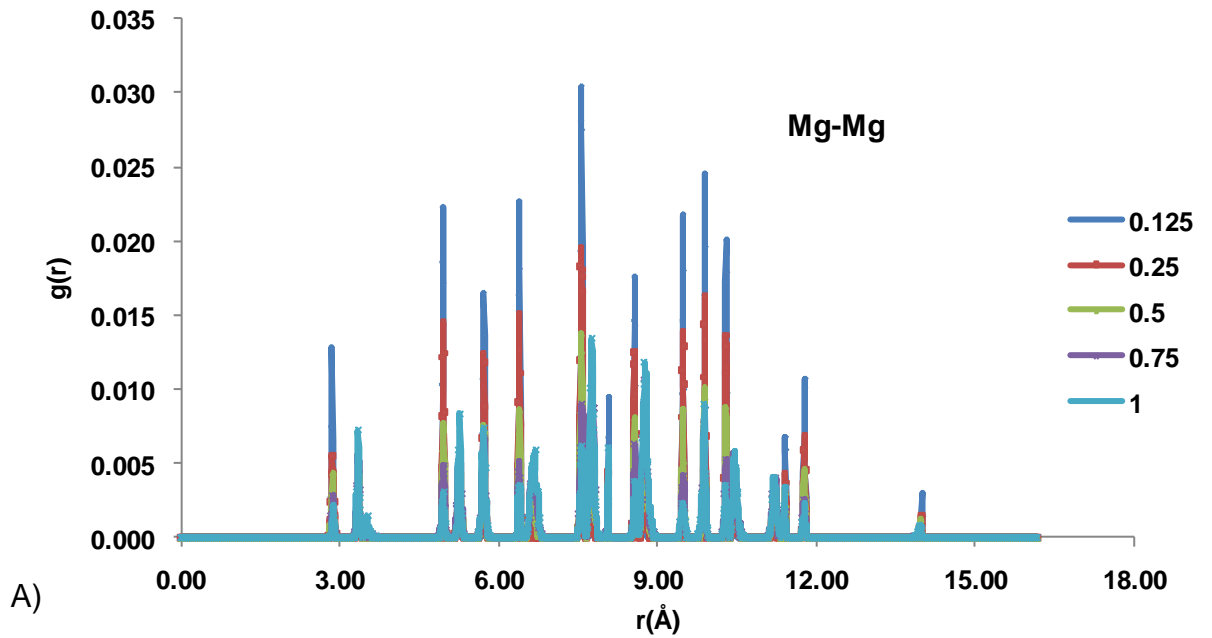
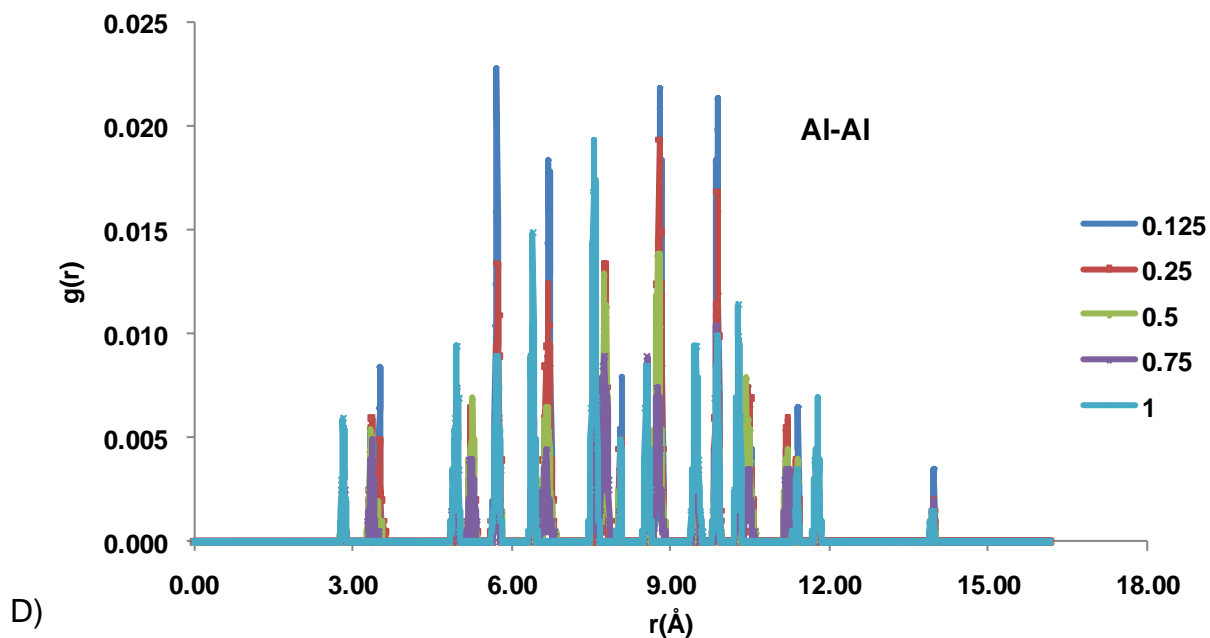
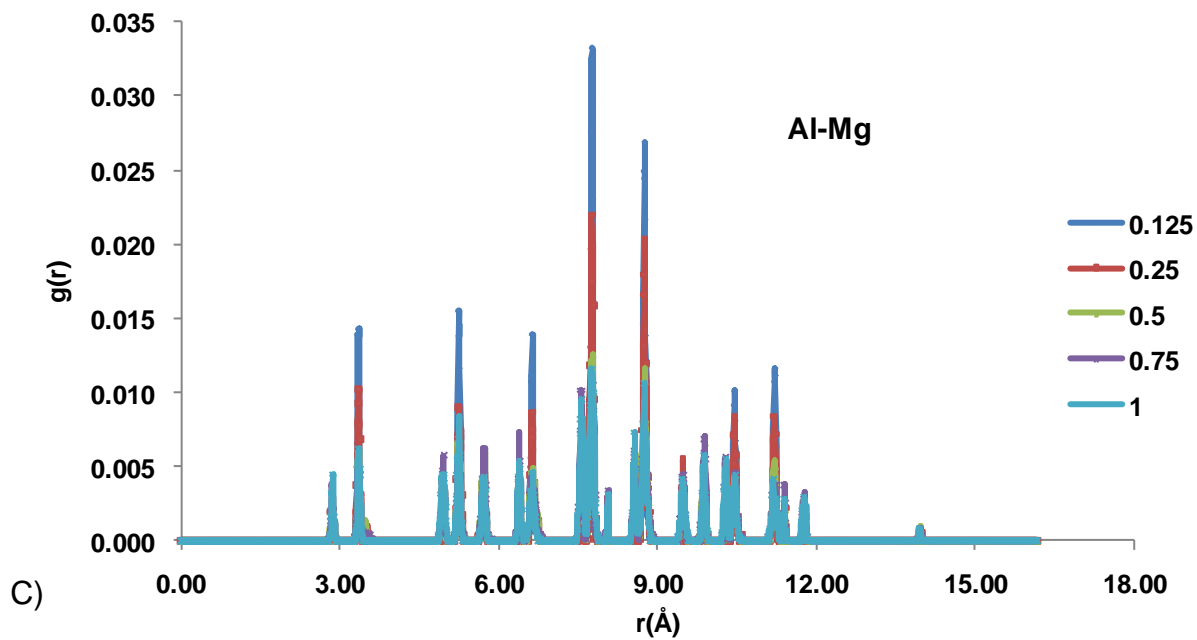


Figure 5-3. Comparison of PDFs for inverted structures for A) Mg-Mg, B) Mg-Al, C) Al-Mg and D) Al-Al

Figure 5-3 Cont... Comparison of PDFs for inverted structures for A) Mg-Mg, B) Mg-Al, C) Al-Mg and D) Al-Al



For better comparison between inverted structures, PDFs for each cation-cation pair are plotted against each other for all the inverted structures except $i=0$ (Fig. 5-3). As seen in Fig. 5-3, with the increase in the value of i , the system shows disorder in the form of less sharp peaks (more spread out). Even though spreading of the peaks does not change significantly at $i=1$, the intensity of peaks gets higher. That corresponds to ordering at tetrahedral site in favor of Al but disorder on the octahedral sites (Fig. 5-3B). Similar results are shown for Al in Figs. 5-3C and D.

5.3 Effects of Inversion on Properties

5.3.1 Lattice Parameter

The unit cell of MgAl_2O_4 has 8 Mg ions which limits the step-size of inversion to 0.125 (1/8). Each Mg-Al interchange changes the inversion by 0.125. Although this large step size covers the whole range of inversion, it might fail to capture some important physics for intermediate inversion values. To overcome this, the system size is increased by 8-fold, thus reducing the step-size from 0.125 to 0.015625. This provided more inversion values for the simulation and better insight into the effects of inversion on material properties. MD and GULP simulations methods were used to equilibrate the structure at $T = 0$ K. As explained above, among the various possible cation arrangements for any particular i value, the lowest energy structure is chosen for the simulation. The effect of inversion is shown in Fig. 5-4 and is compared to the effect captured by Andreozzi et al. [175].

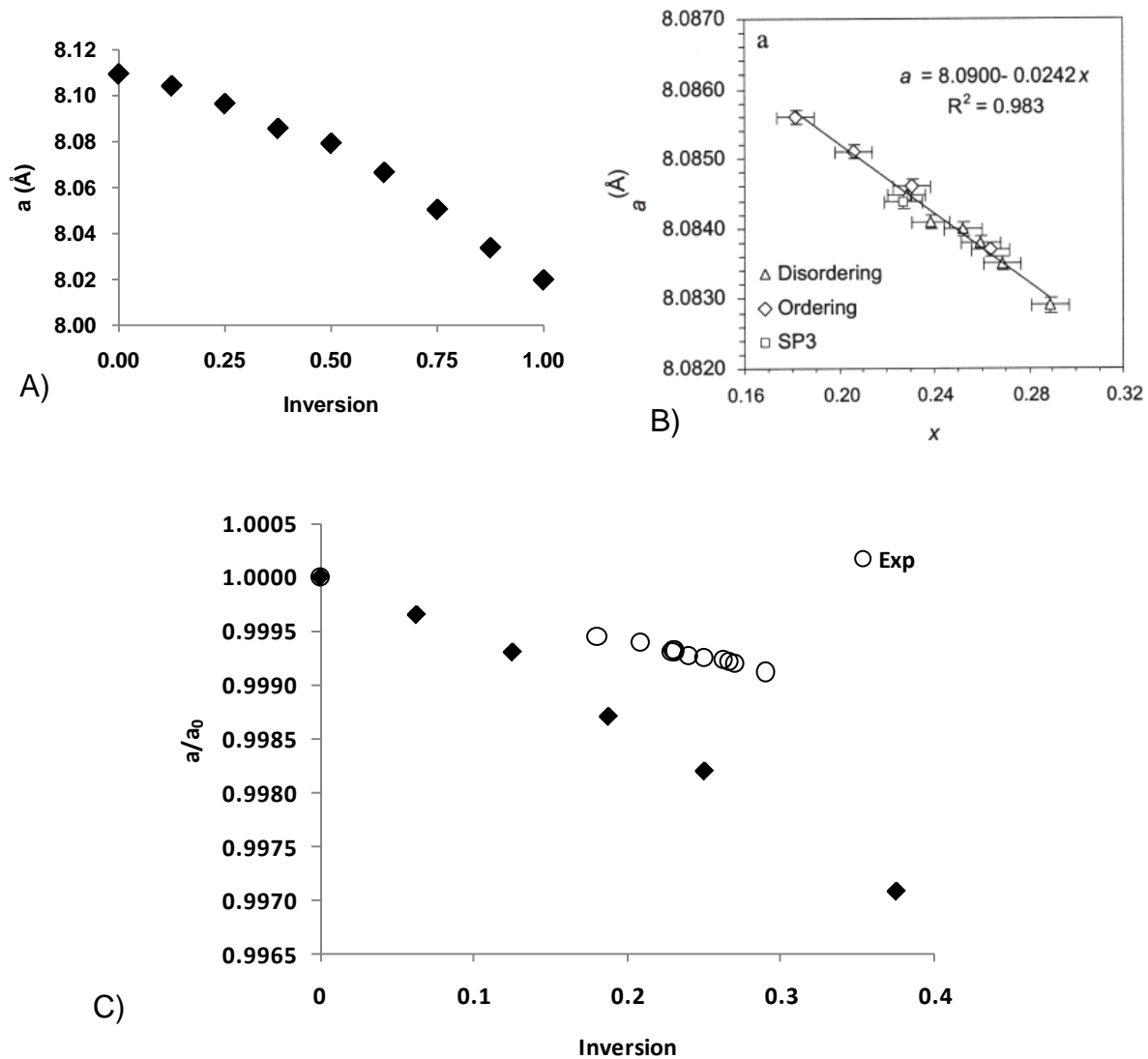


Figure 5-4. Decrease of lattice parameter with inversion A) this MD simulation study B) reproduced from experimental investigation by Andreozzi *et al.* [176] C) comparison between MD and experimental study

Comparison between experiment and this MD simulation study gives an impression of a much stronger dependence of lattice parameter on inversion in MD but in reality that is not the case. Experimental dependence also involves the expansion due to temperature which is absent in simulation data. Even though the experiment in 5-4 B) does not span the full range of inversion available to simulation, both show a

decrease in lattice parameter with inversion. This increase in density with increasing inversion can be qualitatively understood in terms of a simple picture of the bond strength as a function of bond charge. In normal spinel ($i=0$), each tetrahedral site is occupied by Mg^{2+} with 4 O^{2-} neighbors and each octahedral site is occupied by Al^{3+} with 6 O^{2-} neighbors. Each cation shares $\frac{1}{2} e^-$ with each neighboring oxygen on both tetrahedral or octahedral sites. On inversion, Al^{3+} on a tetrahedral site with 4 neighboring oxygens, shares now $\frac{3}{4} e^-$ with each neighboring oxygen, an addition of $\frac{1}{4} e^-$ per bond. Similarly, Mg^{2+} on the octahedral site has 6 neighboring oxygen ions, thus sharing $\frac{1}{3} e^-$, a loss of $\frac{1}{6} e^-$, compared to non-inverted spinel. A simplified picture of bond strength being proportional to bond charge gives a larger change at inverted tetrahedral sites than at octahedral sites. In other words, the decrease in Al-O bond length at tetrahedral sites is larger than the increase in Mg-O bonds at octahedral sites. That, in turn, should produce an overall densification of the spinel upon inversion as is observed.

5.3.2 Anti-site Formation Energy

To investigate the effects of inversion further, the energy is determined as a function of inversion. Consistent with the normal state being more stable, Fig. 5-5 shows an increase in energy with inversion.

This appears to be linear up to $i \sim 0.5$, above which there is a change in slope. A further analysis is performed by calculating the formation energy of each additional cation interchange (Fig. 5-6). It is evident from Fig. 5-5 that up to $i \sim 0.375$, the energy required to form new antisite defects is almost constant. Equivalently, it can be said that for these low inversion cases, existing defects make it neither easier nor harder to form additional antisite defects. Conversely, beyond $i = 0.375$, it becomes comparatively

easier to form new defects with the defect formation energy decreasing by ~25% for the fully inverted system. This decrease in formation energy can be understood in terms of the effects of the antisite defects on the local strain fields. At low inversion, the local strain produced by interchanging Mg and Al cations is small, and is easily relieved by structural relaxations, thus not affecting the formation energy for the next antisite pair to form. As the inversion increases, however cation disordering increases and rearrangement of cations is not able to relieve the strain dipole. Such unrelieved strain dipoles lower the energy required to form strain dipoles of opposite orientation. As a result, the antisite formation energy for each additional disorder decreases.

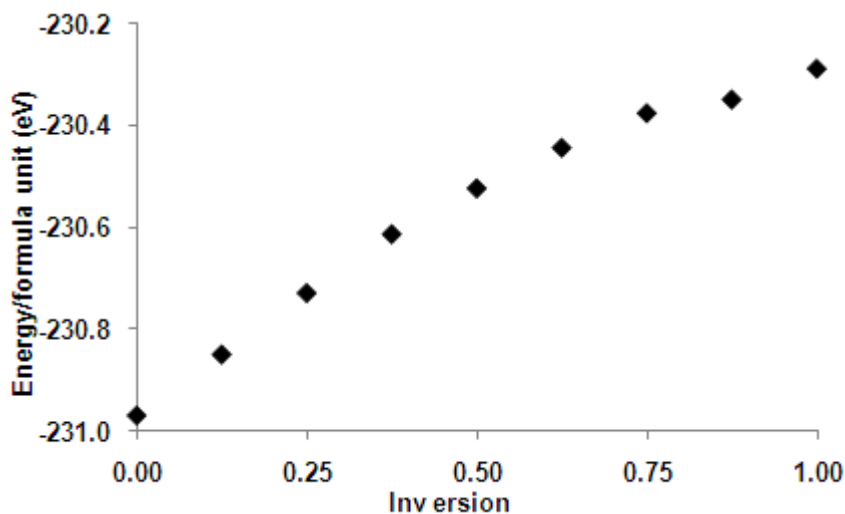


Figure 5-5. Structural energy as a function of inversion for MgAl_2O_4 .

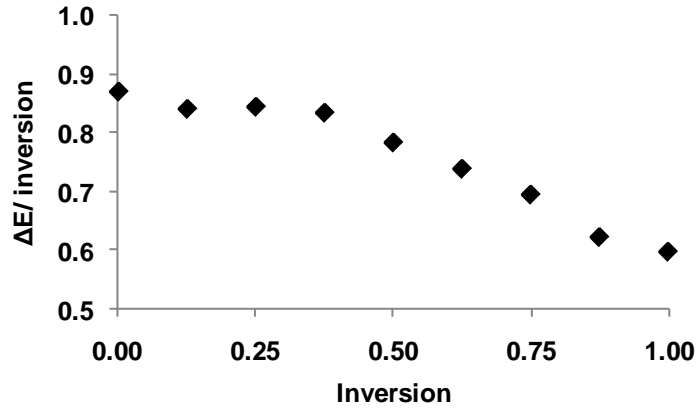
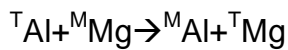


Figure 5-6. Cation antisite formation energy as a function of inversion.

A simple analysis provides further insight into the order-disorder process and will help us understand Figure 5-6. The order-disorder process can be described by a chemical exchange reaction: [177]



where, T is a tetrahedral site and M is an octahedral site. The forward reaction represents the restoration of the ordered structure, the backward reaction represents disordering. K_1 and K_2 are taken as the forward and backward reaction rate constants, respectively. The time rate of change of the Al concentration on a T site is given by

$$\frac{-dX({}^T\text{Al})}{dt} = K_1 \Phi({}^T\text{Al})X({}^T\text{Al})\Phi({}^M\text{Mg})X({}^M\text{Mg}) - K_2 \Phi({}^T\text{Mg})X({}^T\text{Mg})\Phi({}^M\text{Al})X({}^M\text{Al}) \quad (5-1)$$

where X is the fraction of T sites occupied by Al and Φ is analogous to an activity coefficient and is generally a function of temperature, composition and volume.

Assuming ideal mixing in each site [178] and at equilibrium $\frac{-dX({}^T\text{Al})}{dt}$ is 0, applying

these two conditions on Eq. 5-1, it becomes:

$$\frac{K_2}{K_1} = \frac{X({}^T\text{Al})X({}^M\text{Mg})\Phi({}^T\text{Al})\Phi({}^M\text{Mg})}{X({}^T\text{Mg})X({}^M\text{Al})\Phi({}^T\text{Mg})\Phi({}^M\text{Al})} \quad (5-2)$$

In MgAl_2O_4 spinel, $X(^T\text{Al})=x$, $X(^T\text{Mg})=1-x$, $X(^M\text{Mg})=x/2$ and $X(^M\text{Al})=1-x/2$.

After substituting, Eq. 5-2 turns into

$$\eta \equiv \frac{K_2}{K_1} = \frac{x^2}{(1-x)(2-x)} \frac{\Phi(^T\text{Al})\Phi(^M\text{Mg})}{\Phi(^T\text{Mg})\Phi(^M\text{Al})} \quad (5-3)$$

As already pointed out, K_2 signifies the reaction rate for disordering and K_1 for ordering. In the original analysis by Mueller, all Φ values are taken to be unity for the crystals with two non-equivalent sites [178].

$$\eta \equiv \frac{K_2}{K_1} = \frac{x^2}{(1-x)(2-x)} \quad (5-4)$$

In that case for the Eq. 5-4, $\eta > 1$ signifies the disordering of the structure being the dominant reaction. Solving the inequality equation for disordering as the preferential reaction, gives $x > 2/3$. This simple analysis shows that, disordering becomes preferential after the system achieves ~66% inversion. Even though the threshold value for inversion is different, this simple model shows that each additional disorder in MgAl_2O_4 costs less energy after the threshold value. The analysis here is based on all the Φ values being unity. The value of Φ may change from unity, given high temperature, electrostatic charge analysis [179] favors inversion and disordered structure release strain by more disorder. Combining it with the work presented here, it is proposed that the disordered structure at low inversion values forms stress dipoles at inverted sites to release the strain, thereby lowering the energy of the system. This is also shown by the smallest possible inversion, exchange of 1 antisite pair. Figure 5-6 shows the variation of the formation energy for the inverted structure as a function of distance between inversion sites.

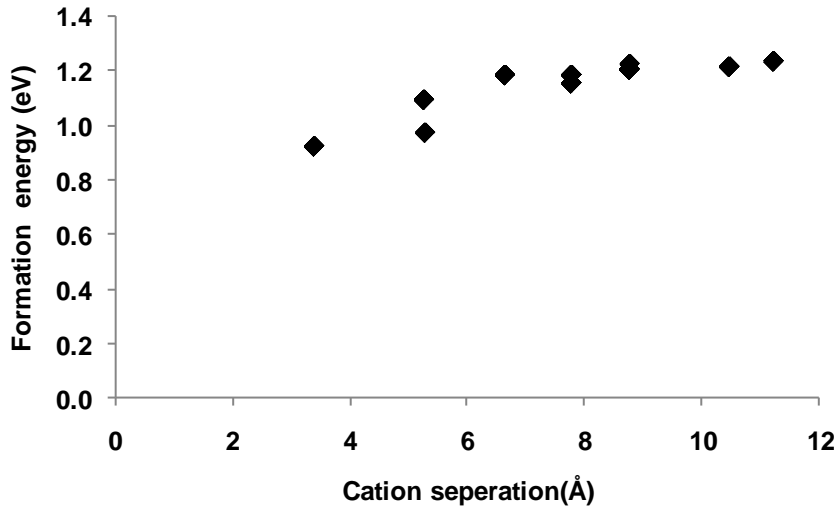


Figure 5-7. Formation energy as a function of inversion site distance.

As seen in Fig. 5-7, inverted sites prefer to be in close proximity. Based on the result of 1 antisite pair energy and theoretical understanding, it can be hypothesized that, as disorder increases, tetrahedral sites are increasingly occupied by Al. Also the Al-O bond length is decreased at tetrahedral sites. At 50% inversion, tetrahedral sites are equally occupied by Al and Mg. Combined with electrostatic analysis (favoring of Al on tetrahedral sites) and reaction rate analysis (less energy expense for each additional cation disorder after certain inversion value), favoring of disorder can be understood. This transition is seen at lower than 50% inversion, which can be attributed to the approximations and simple reaction rate analysis. The effect of inversion on the elastic properties is discussed in the next section.

5.3.3 Bulk Modulus

For a typical solid, the bulk modulus increases as the system becomes denser due to the rapidly increasing interatomic repulsion. Based on this argument, the bulk modulus is expected to increase with inversion. As the crosses in Fig. 5-8 indicate, the

behavior is actually more complex: initially the bulk modulus decreases slightly, then levels off, and then increases above $i=0.5$. A similar strong dependence of the bulk modulus at high inversions in MgAl_2O_4 was also reported by Chartier *et al.* in their MD simulations [180] (Fig. 5-8 B)). The interatomic interaction in their study had Buckingham interaction with Morse potential as short range interaction which was fitted by Morooka *et al.* [181]. That potential is developed to capture the Frenkel pair accumulation under neutron irradiation. The system might also turn to an amorphous state. Since the system under investigation had no point defects, other than cation anti-site disorder, potential parameters are chosen as described in Table 2-3.

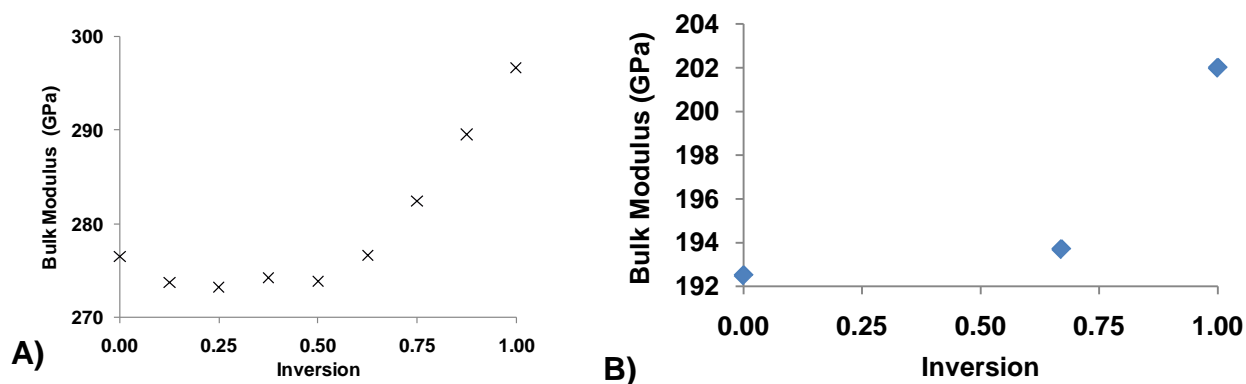


Figure 5-8. Bulk modulus as a function of inversion A) this work B) reproduced from the reference [180]

Even though values of the bulk modulus are different in the two studies, qualitative effect of inversion on the bulk modulus is very similar in nature. To compare the qualitative behavior of bulk modulus, the bulk modulus is normalized to normal spinel ($i=0$) for both the simulation studies and compared in Fig. 5-9. The small differences are due to the different description of the interatomic interactions used in the two studies. The potential description used in the study by Chartier [180] and developed by Morooka *et al.* [181] and has the Buckingham form and a Morse potential.

The good agreement argues that the specific description of the interatomic forces are not essential to obtain qualitative and semi-quantitative trends in behavior.

The dependence of the bulk modulus on inversion can be understood in terms of the separate contributions of inversion to cation disordering alone and to the associated volume change. To dissect these effects further, each contribution was studied separately: such separation is not possible experimentally, but is straightforward in simulation. The separate effects on the bulk modulus are shown in Fig. 5-10.

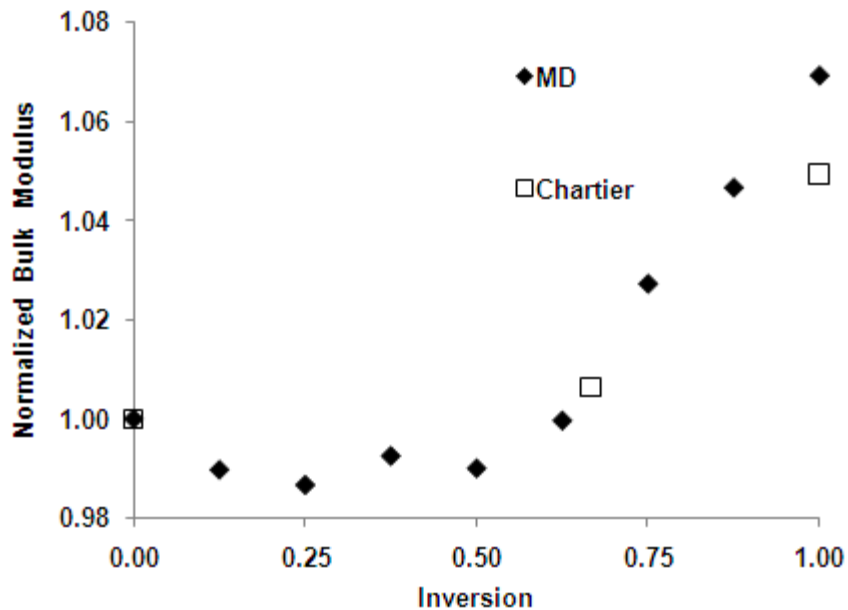


Figure 5-9. Comparison of normalized bulk modulus with MD study by Chartier [180]

First, the volume of the system was fixed to that of normal spinel and the bulk modulus was calculated as a function of inversion, thereby picking out the the effect of the cation arrangement on the bulk modulus (filled circles in Fig. 5-10). Initially the bulk modulus decreases with inversion, then levels off. It has been already shown (Sec. 5.3.1) that inversion causes shortening of Al-O bonds and expansion of Mg-O bonds at inverted sites, respectively. A similar effect of decrease in bulk modulus with cation disordering was experimentally observed in MgTi_2O_5 [170].

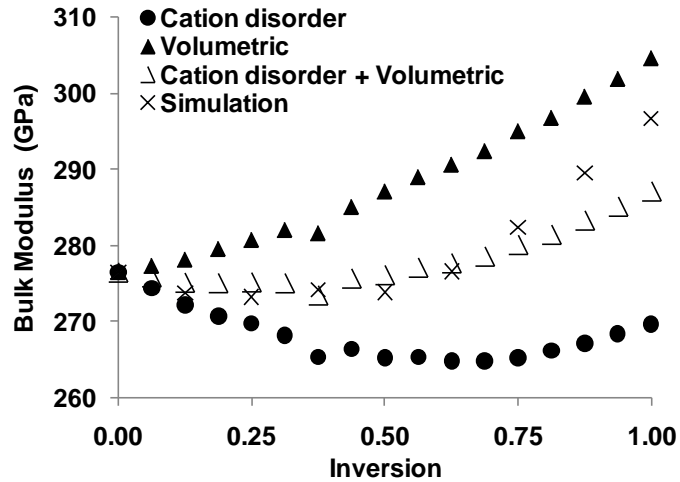


Figure 5-10. Separating out various effects on bulk modulus

In the case of single crystal MgTi_2O_5 , the decrease in bulk modulus was attributed to the different compressibility of the weaker Mg-O and stronger Ti-O bonds and the way in which the octahedra are arranged. Even though MgTi_2O_5 (orthorhombic-dipyramidal Bbmm) and MgAl_2O_4 are structurally different, the behavior of cation disordering is analogous because they both display weaker Mg-O bonds under cation disordering. Since this bond weakening is primarily responsible for lowering bulk modulus in MgTi_2O_5 for low inversions, it is also most likely related to lowering of bulk modulus in MgAl_2O_4 . The leveling off of bulk modulus with inversion suggests the limited effect of weak Mg-O bonds in this case, as compared to MgTi_2O_5 [170]. This also suggests that there is an increasing effect of Al-O bonds with inversion. Since the lengthening of the Al-O bond has precisely the opposite effect on elastic properties, a small increase in the bulk modulus at higher values of I is seen.

Second, the bulk modulus for normal spinel was calculated as a function of volume. Using the relationship between the degree of inversion and volume, the volume dependence of the the bulk modulus was replotted as a function of the inversion (filled

triangles in Fig. 5-10). It is evident from Fig. 5-10 that the decrease in volume monotonically increase the bulk modulus, consistent with the usual behavior of crystals. To capture the combined effect of volume and cation disordering, the average of the two effects is taken as an estimate for the dependence of the bulk modulus on inversion. As the triangles in Fig. 5-10 shows, this prediction matches the actual simulation results reasonably well. In particular, it shows that the volumetric effect essentially negates the effect of cation disorder up to $i=0.375$. For higher degrees of inversion, further cation disorder has little effect, while the volumetric contraction leads to an increase in the bulk modulus.

5.3.4 Thermal Expansion

The behavior of bulk modulus was attributed to the relative strength between inverted Mg-O and Al-O bonds and to the volume change. These effects are also manifested in the thermal expansion. To calculate the thermal expansion, a series of MD simulations were run at different temperatures for NPT ensembles (for details refer to Chapter 2). The coefficient of thermal expansion is computed for each inversion value following the procedure described in Sec. 2.10. The variation of lattice parameter for $i=0$ with temperature is shown in Fig. 5-11. Similar variation of lattice parameter with temperature is shown for all other inversion values. The thermal expansion coefficients for each inversion value are compiled in Fig. 5-12.

The similarity in the effect of inversion on the bulk modulus and thermal expansion is expected. The bulk modulus and the thermal expansion can be related through the Grüneissen relation [30]:

$$\alpha = \gamma C_v / 3B \quad (5-4)$$

where C_v is the specific heat and γ is the Grüneisen coefficient, which measures the anharmonicity of the interatomic interactions. In Eq. 5-4, if everything else is constant, the thermal expansion and bulk modulus are expected to show opposite behavior with inversion. As seen by Fig. 5-8, bulk modulus increases with inversion after reaching $i=0.5$ and from Fig. 5-12, thermal expansion decreases.

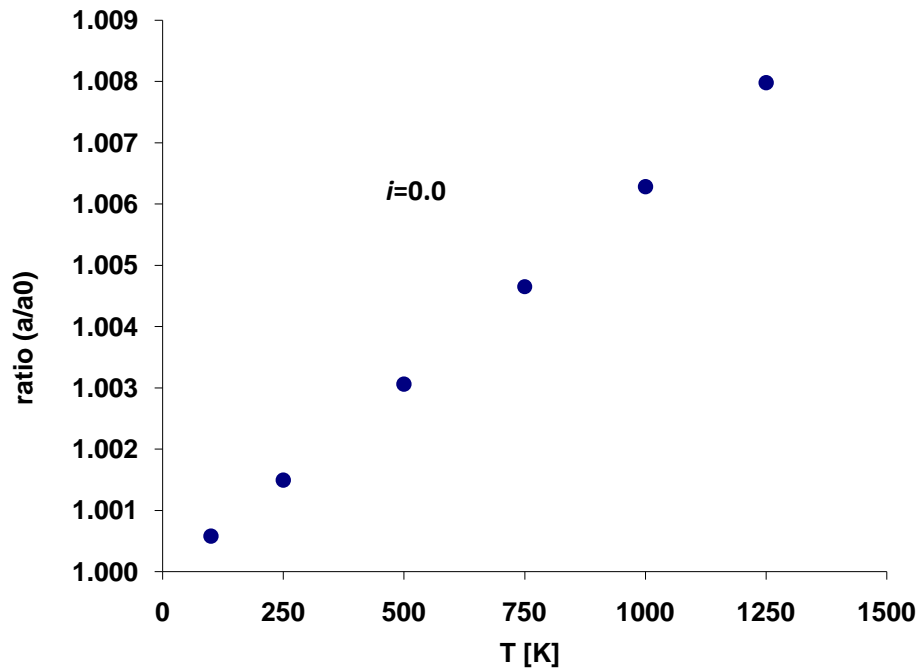


Figure 5-11. Variation of lattice parameter with temperature for $i=0$.

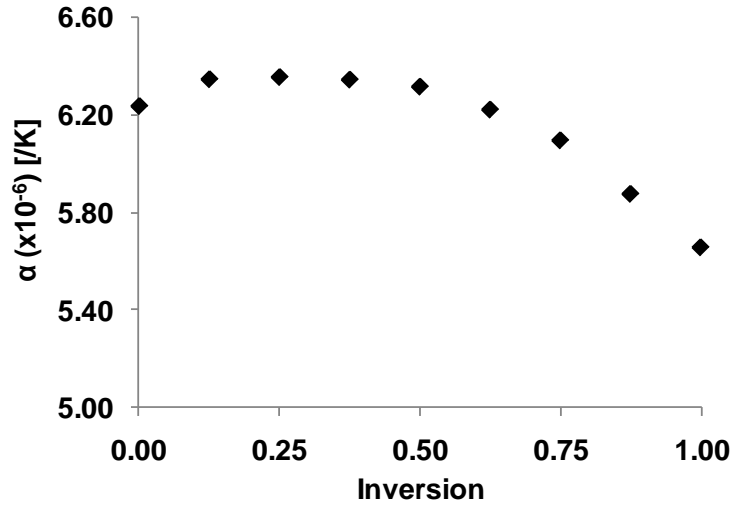


Figure 5-12. Coefficient of thermal expansion as a function of inversion.

Using simulated values of α , C_v and B ; γ is calculated using Eq. 5-4. The dependence of γ on inversion is illustrated in Fig. 5-13 and suggests that γ does not depend strongly on inversion. The average value of $\gamma \sim 2$ is consistent with the value of 2.0 experimentally reported by Chopelas and Hofmeister [182].

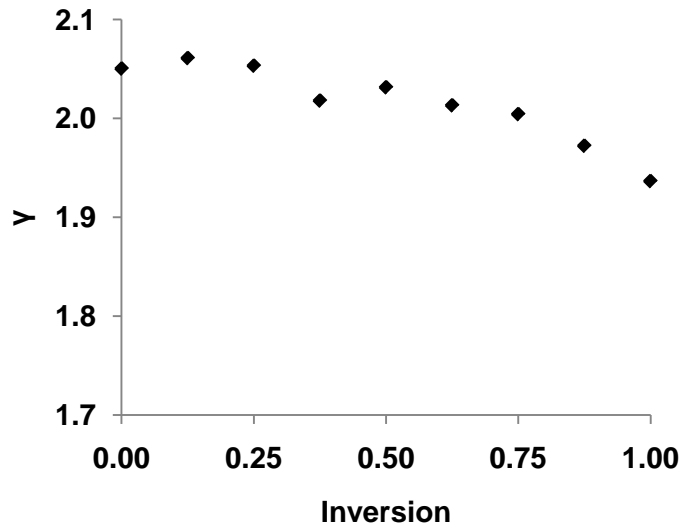


Figure 5-13. Dependence of the Grüneisen coefficient on inversion.

The Grüneisen coefficient is a measure of the anharmonicity of the system. The good agreement between MD results and the experimental findings shows that the interatomic potential yields the same level of anharmonicity as the experiment. As shown previously that the thermal expansion is related to the thermal conductivity through the anharmonicity (for details, please refer Ch. 2). Thus, the analysis suggests that the simulated thermal conductivity values should be at least semi-quantitatively correct.

5.3.5 Thermal Conductivity

As noted in the Sec 5.1, MgAl_2O_4 undergoes inversion under neutron irradiation. A similar simulation set-up as described in Section 2.10 is used to compute the thermal conductivity. These thermal conductivity values are then corrected for system size effect and compared to the experiment (Fig. 5-14). Thermal conductivity results for normal ($i=0$) MgAl_2O_4 are shown as open circles in Fig. 5-14. The MD results are shown as open circles and “corrected” represents the thermal conductivity values after harmonic analysis is performed on these MD values. As explained in Chapter 2, harmonic analysis provides a correction factor based on the accuracy of interaction parameters in reproducing bulk modulus and thermal expansion values to the experimental values. Table 5-1 provides detailed information about the correction factor calculated by harmonic analysis. Based on the numbers from Table 5-1, the correction factor comes out to be equal to 1.52. That means, based on the fidelity of the interaction potential, thermal conductivity values will be 1.5 times higher than the experimental counterpart (For details, please refer Eq. 4-6). After dividing MD simulation thermal conductivity values by 1.52, they are plotted as open triangles in Fig. 5-13 and termed as

“corrected”. The filled circles are taken from the experimental studies of Burghartz *et al.* [183].

Table 5-1. Comparison of thermal expansion and bulk modulus for harmonic analysis

	α ($\times 10^{-6} / ^\circ\text{K}$)	Bulk Modulus (GPa)
Experiment	8.89 [184]	197.4 [172]
Simulation	6.1	275.74

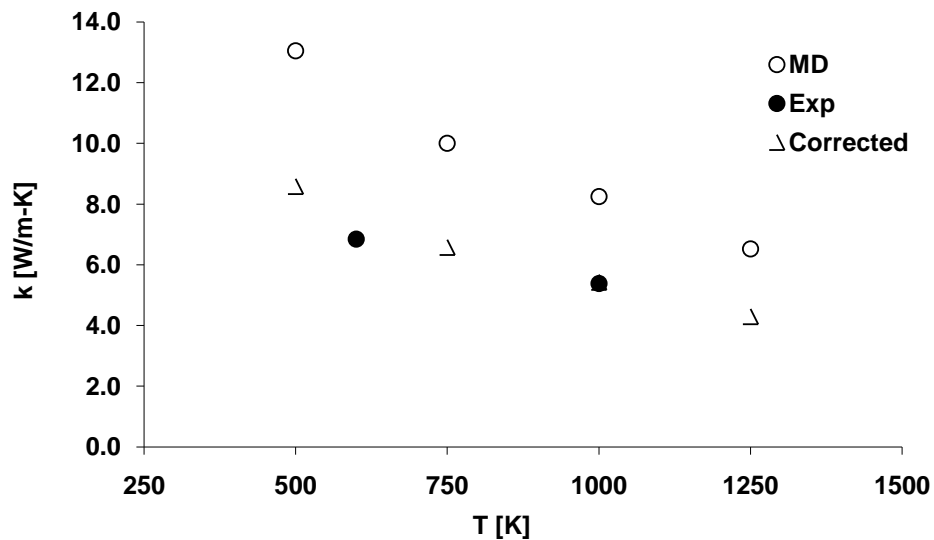


Figure 5-14. Variation of thermal conductivity for MgAl_2O_4 with temperature, open symbols represent the simulation results and filled circles are points reproduced from the experimental study by Burghartz *et al.* [183]

The similarity between experimental and simulated thermal conductivity values gave the confidence to use the simulation tool for further investigation. Since the working temperature for nuclear fuels is in the range of 800 K-1500 K, investigation on thermal conductivity as a function of inversion is performed at 1250 K.

Finite system size analysis (For details, please refer Eq. 2-46) is performed to take into account any artifacts produced by system size limitations. A system size analysis

for each inversion value is shown in Fig. 5-15. The circles at $y=0$ gives the estimate of inverse of thermal conductivity for infinite system size. These infinite system size thermal conductivity values are computed using a linear fit and taking the inverse of intercept at $y=0$ (Chapter 2).

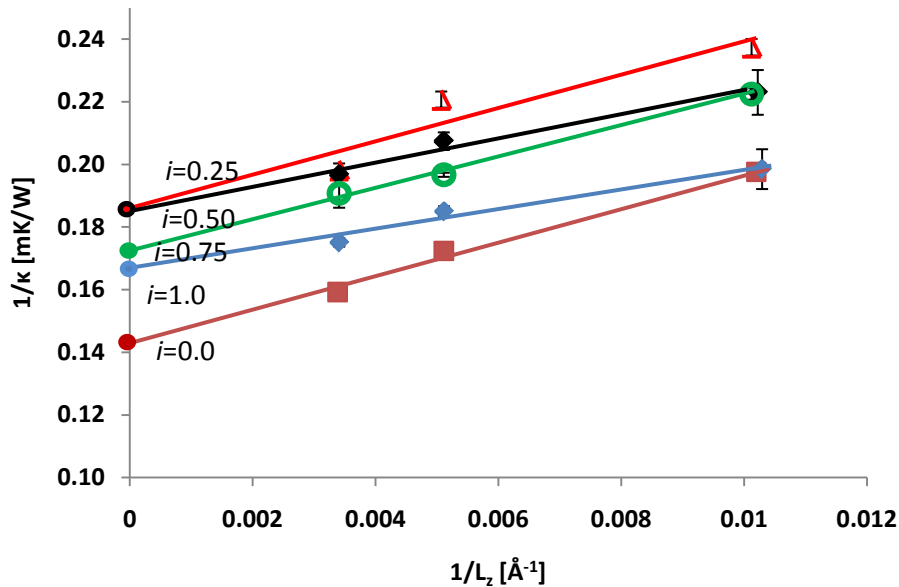


Figure 5-15. System size analysis for different inversion values for MgAl_2O_4

The extrapolated thermal conductivity values for different inversion values of MgAl_2O_4 system are plotted as open triangles against inversion in Fig. 5-16. The rather weak dependence of the thermal conductivity on inversion is quite surprising when viewed in terms of the thermal transport properties of defected ceramics materials. In particular both experiments and MD simulations of fluorite-structure materials (e.g., yttria-doped zirconia and hyperstoichiometric UO_2) have shown a strong decrease in thermal conductivity with even quite low defect concentrations [63, 185]. The key difference between the spinel case and the fluorite structured materials is that here disorder only involves antisite defects, while for the fluorites the disorder involved

oxygen vacancies (zirconia) and oxygen interstitials (urania), which presumably affect the phonon properties and hence thermal conductivity much more strongly.

By recalling the relation between anharmonicity and thermal conductivity of the system, as defined by the Eq. 4-2, the inversion dependence in a quantitative manner can be understood. This representation of thermal conductivity is based on the Debye approximation which assumes all phonon modes present in the system are acoustic and contribute to the thermal conductivity. It works well for very simple systems but as the structural complexity increases, the actual thermal conductivity values deviate from the predicted values. For the system, even though Eq. 4-2 cannot be expected to quantitatively predict the thermal conductivity, it should still capture the qualitative picture of the variation of thermal conductivity with inversion.

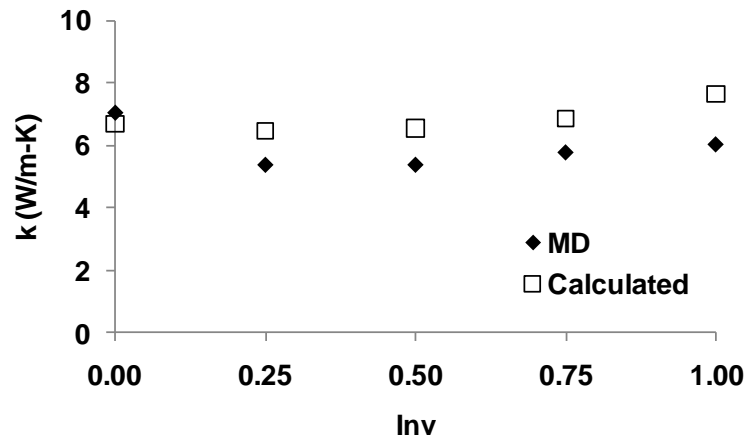


Figure 5-16. Dependence of thermal conductivity variation on inversion

The thermal conductivity calculated from MD does show a shallow minimum at $i \sim 0.5$, not predicted from the anharmonicity analysis alone. This minimum can be attributed to the degree of disorder in the system which, for the fluorites, led to a significant drop in the thermal conductivity [186-188]. There are various factors that can

produce differences between thermal conductivity values calculated from MD and the predicted values by using Eq. 4-2. They are investigated one by one:

Effect of density: As already shown, the volume decreases with inversion (Fig 5.2). This increase in density increases the sound of speed in the material. The effect of cation disorder and volume on the thermal conductivity is separated out with the help of these two simple cases:

Case 1: Change the lattice parameter to $i=0.0$ value for $i=0.5$ and 1.0

The lattice parameter of the inverted structures ($i=0.5$ and 1.0) is increased to the value of $i=0.0$ (normal). By comparing the thermal conductivity values of the $i=0.5$ structure with two different lattice parameters, the effect of density on thermal conductivity is calculated. Similar study is done on $i=1.0$ structure also. The results are shown in Fig. 5-16 and showed a negligible effect ($\sim 1\%$) of the density on the thermal conductivity.

Case2: Change the lattice parameter to $i=1.0$ for $i=0.0$

To extend the study of case 1 on perfectly ordered structure ($i=0$), the lattice parameter of normal MgAl_2O_4 is changed to the value of $i=1.0$. The results are also shown in Fig. 5-15 and again no significant effect of density on thermal conductivity is found.

Arrangement of cations: This analysis is motivated by the fact that for each inversion, there could be thousands of possible ways to arrange the cations. Similar to the analysis mentioned in Sec. 5.2, was performed here. Instead of choosing the lowest energy structures (as was done for the thermal expansion), structures with lowest and highest energies for same i values were chosen for thermal conductivity simulations. A

difference of less than 1% in the thermal conductivity between these structures was found. This is in accord with the expectation. Since random distribution of cations does not introduce any new defect in the system, no change in thermal conductivity was expected.

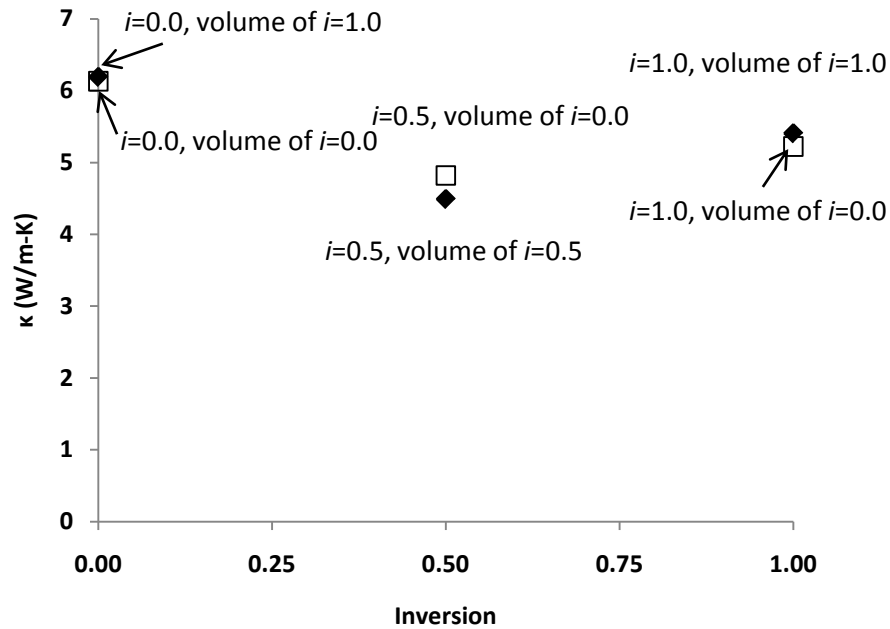


Figure 5-17. Density effect on thermal conductivity

Total scattering sites: A key effect of point defects is the number of possible scattering sites in the system produced by antisite defect creation. To capture the effect of point defects, a simple “combinatorics analysis” was used. With each inversion, the possible number of scattering sites is

$$C_{n_i}^{Mg} \cdot C_{n_i}^{Al}, \quad (5-5)$$

where $C_{n_i}^{Mg}$ denotes the number of possible ways to generate the structure for the inversion i , involving n_i Mg and n_i Al ions. Thus, the product is a measure of possible number of scattering sites for the inversion value (i). As an example, for $i=0$, Mg and Al occupy tetrahedral and octahedral positions, and there is only one way to arrange the

cations. For one anti-site pair, in one unit cell system, 1 Mg can be in any of the 16 possible Al sites and also Mg can be chosen in 8 different ways. The multiplicity of these possible arrangements with inversion can be expected to have an impact on the thermal conductivity. Figure 5-17 captures the variation of the number of possible arrangements for each cation site for each inversion.

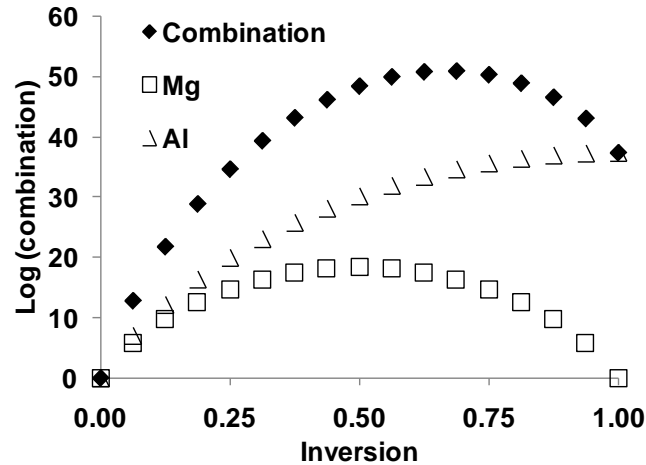


Figure 5-18. Combinatoric analysis: y-axis shows number of possible combinations for Mg-Al exchange possible in 2x2x2 unit cell system of MgAl_2O_4

Even though $i=1$ signifies the totally inverted structure, it does not have the most number of possible combinations, because all of the A sites are now totally occupied by Al. There is a maximum in the number of different defect arrangements at $i=0.67$, at which point the system would display the maximum number of different scattering environments. If there were no other effects, a minimum in the thermal conductivity at $i=0.67$ is expected. The fact that the thermal conductivity is actually a minimum at close to $i=0.5$ suggests that the disorder on the A sublattice actually affects the phonon scattering more strongly than the disorder on the B site. This can be understood in terms of local strain produced at inverted sites. As previously discussed, the T_{Al} sites experience greater strain than the M_{Mg} sites and thus affect material properties to a

greater extent. As inversion increases, T_{Al} experiences more chemical disorder; at $i=0.5$ half are occupied by Mg and half by Al above $i=0.5$ they become more and more populated by Al ions.

5.4 Conclusion

The MD study has provided significant insights into the effects of inversion on the thermo-elastic properties of $MgAl_2O_4$. Ease of formation of more disorder in already inverted structures is shown by this study. The effect of inversion is extended on thermo-elastic properties of $MgAl_2O_4$ by scanning the whole range of inversion ($i=0-1$). The effects of temperature and cation arrangement are also separated.

The decrease in lattice parameter with inversion is shown to arise from a simple charge sharing between cation-oxygen at tetrahedral and octahedral site. The effect of disorder already present in the structure on the formation of new cation arrangement is also presented. A simple theoretical analysis favors the formation of disordered structure after $i\sim 0.67$ and the simulation results presented the favoring of additional cation disorder after $i\sim 0.37$. The difference from the theoretical model is explained in the light of simplified analysis and charge analysis favoring the inverted structure for $MgAl_2O_4$.

The variation in elastic constants and bulk modulus with inversion are reported and compared with other DFT and MD studies. Contributions to the bulk modulus are analyzed in two parts: volumetric and cation disorder. This study has shown that weakening of Mg-O bonds at inverted octahedral sites essentially negates the volumetric effect on bulk modulus up to $i\sim 0.5$. After $i=0.5$, stronger Al-O bonds at inverted tetrahedral sites and volumetric effects dominate and control the bulk modulus of $MgAl_2O_4$.

The effect of thermal expansion as a function of inversion is also captured and explained. As expected from the bulk modulus results, thermal expansion remain almost unchanged up to $i \sim 0.5$ and decreased afterwards. Anharmonicity of the system is calculated using bulk modulus and thermal expansion and compared to the experimental value.

The thermal conductivity for the normal structure reproduces values similar to the experimental ones. The study is extended to include the effect of inversion on thermal conductivity, which has never been done before. The thermal conductivity results are compared with the theoretically computed values. Deviation from the theoretical model is reported and explained with the help of a “combinatorics analysis”.

CHAPTER 6
THERMAL TRANSPORT PROPERTIES OF $\text{Bi}_4\text{Ti}_3\text{O}_{12}$

6.1 Introduction: Thermal Barrier Coating

Thermal barrier coatings (TBCs) are applied on materials operating at elevated temperatures to act as insulation. TBCs are widely used in turbine blades, combustor cans, gas turbines and aero engine parts. The most common place where to see a gas turbine engines is commercial jets and in electricity generating plants. In gas turbines a pressurized gas spins the turbine. Pressurized gas is generated by burning fuel in the engines. Possible fuels include propane, kerosene, jet fuel or natural gas.

The main advantages of gas engines are that they are smaller in size than their counterparts and have a greater power to weight ratio. Their use is limited to power reactors and commercial jets or tanks because of the cost, high operating temperature and high spin speed of the turbine and limitations of constant load rather than fluctuating one.

Jet engines can be classified as either turbofan or turbojet. Both work on the same principle. A schematic of a simple turbofan is shown in Fig. 6-1. They have three parts: *The compressor* compresses the incoming gas to about thirty times its original pressure. *The combustion area* burns the fuel and produces high pressure, high velocity gas. *The turbine* extracts power from the high velocity high pressure gas.

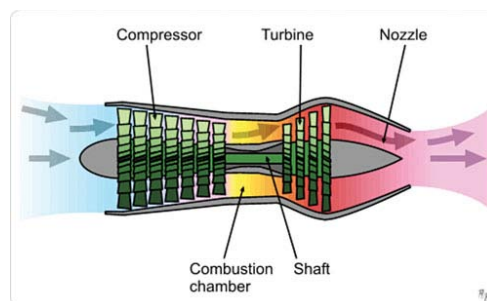


Figure 6-1. Simple schematic view of turbofan gas turbine engine [189]

Thermodynamically the Brayton cycle is used to describe gas turbines. In the Brayton cycle, air is compressed isentropically, combusts at constant pressure and expands again isentropically at the initial pressure. An idealized Brayton cycle is shown in Fig. 6-2.

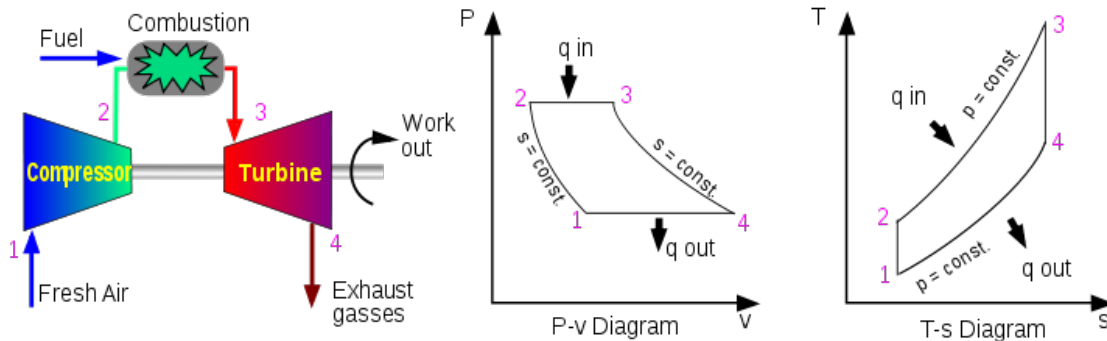


Figure 6-2. Idealized Brayton cycle [190]

Similar to other heat cycles, the efficiency of the Brayton cycle is proportional to the combustion temperature. There is thus a strong incentive to increase the operating temperature. The limiting factor to elevate the operating temperature is the limitations of the performance of the materials that make up the engine and its parts to withstand heat and pressure. To elevate the temperature, thermal barrier coatings (TBCs) are applied to the turbine blade itself [191]. A TBC is primarily made of four layers (Fig. 6-3):

1. *Ceramic top-coat*: This layer provides the thermal insulation for the turbine blade. It has very low thermal conductivity and is designed to withstand a large number of thermal cycles. The most common TBC material is yttria stabilized zirconia (YSZ) which has a thermal conductivity around 2.3 W/mK at $\sim 1000^{\circ}\text{C}$ and melting point around 2700°C . These are typically 100 μm to 2 mm thick.
2. *Thermally Grown oxide (TGO)*: This layer is created when the top-coat reacts with the bond coat layer. It is about 1-10 μm thick.

3. *Bond coat*: This layer is about 75-150 μm thick and is below the TGO. The purpose of this layer is to hold the top-coat on the substrate. This layer is made of Ni and Pt and often consists of more than one layer of different compositions.
4. *Substrate*: The turbine itself is generally made of a superalloy and is cooled by hollow channels inside the turbine blade.

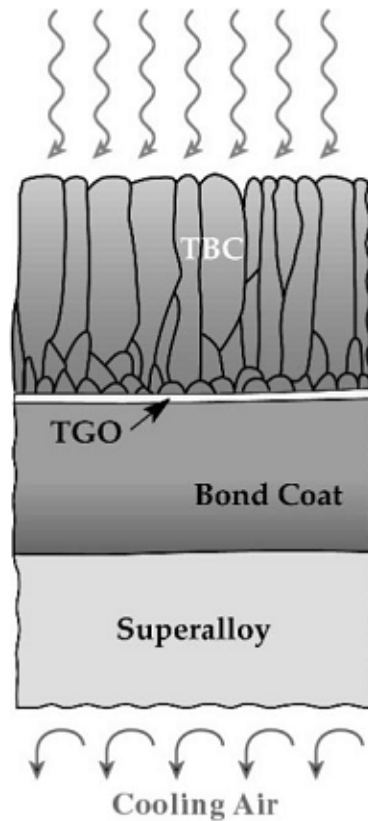


Figure 6-3. Schematic of a TBC [192]

The important considerations in the selection of a TBC material are its ability to withstand thermal stresses with repeated heating and cooling cycles; thermodynamic compatibility with oxides formation of bond coat; and low thermal conductivity. The current material of choice for TBCs is yttria-stabilized zirconia (YSZ) in its metastable tetragonal-phase; it will also remain the material of choice for the current operating temperatures [193]. However, YSZ has poor creep resistance at high temperatures

which results in crack and eventually spallation. YSZ also has high diffusivity of oxygen that results in oxidation of bond-coat layer. The limiting factors of YSZ and the need for higher operating temperature provides a motivation for developing new materials for TBC applications.

Table 6-1. Different forms of layered perovskites

Composition/Formula	Layer orientation	Name and example
$A_{n+1}B_nX_{3n+1}$ or	$\{001\}_p$	Ruddlesden-Popper
$A_2'[A_{n-1}B_nX_{3n+1}]$		$Sr_3Ti_2O_7$
$A'[A_{n-1}B_nX_{3n+1}]$	$\{001\}_p$	Dion-Jacobson
		$RbCa_2Nb_3O_{10}$
$Bi_2O_2[A_{n-1}B_nX_{3n+1}]$	$\{001\}_p$	Aurivillius
		$Bi_4Ti_3O_{12}$
$A_nB_nX_{3n+2}$	$\{110\}_p$	$Ca_4Nb_4O_{14}$
$A_{n+1}B_nX_{3n+3}$	$\{111\}_p$	$Ba_5Nb_4O_{15}$

Even though all the requirements are critical in the selection of TBC material, low thermal conductivity remains the primary criterion. Desirable properties of TBCs include large average atomic numbers, large unit cell and the possibility of bonding and structural disorder [194]. Aurivillius compounds possess many of the required properties for TBCs. These anisotropic layered materials have weakly bonded planes (Bi_2O_2 layers

or any other layer between perovskites) between layers of pseudo-perovskites having rigid polyhedra. This intrinsic structural disorder acts as a barrier to phonons and reduces their mean free paths. Thus the weakly bonded planes in layered perovskite materials are useful in achieving lower thermal conductivity values without introducing any external defects or dislocations in the system. Anisotropic thermal expansion exhibited by these layered materials is useful in minimizing residual stresses. Based on the composition of inter-slabs and/or the orientation of the layer plane relative to aristotype cubic lattice, these layered perovskites are divided into five groups as shown in Table 6-1.

In Table 6-1 for $\{001\}_p$ notation, p refers to pseudocubic. Among these layered perovskite types, Aurivillius structures possess many desirable properties for use as a TBC. As shown in Table 6-1, Aurivillius compounds are represented by the general formula $(\text{Bi}_2\text{O}_2)^{2+}[\text{A}_{n-1}\text{B}_n\text{O}_{3n+1}]^{2-}$, where n represents the number of perovskite layers separating Bi_2O_2 layers. A simple Aurivillius compound with $n=3$, $\text{Bi}_4\text{Ti}_3\text{O}_{12}$ $\{(\text{Bi}_2\text{O}_2)[\text{Bi}_2\text{Ti}_3\text{O}_{10}]\}$ has many promising properties (large atomic number, large unit cell, anisotropic structure, layered structure) to be a potential TBC material. A recent study by Shen *et al.* has investigated the low value and anisotropic nature of the thermal conductivity of $\text{Bi}_4\text{Ti}_3\text{O}_{12}$ (BIT) and attributed the low value to the density difference between layers [20]. Further investigations pertaining to the effects of density difference between layers and other intrinsic factors on limiting thermal transport properties of BIT might be useful. The experimental studies, however, face two big challenges:

1. It is very hard to synthesize single crystals
2. It is impossible to tune the density of layers to the desired value.

Both of the experimental limitations are easily handled by atomic-level simulation. Therefore, the experimental investigation is expended with the help of MD simulation. In this chapter, the effects and limitations of density and intrinsic structural factors on the thermal transport of single crystal BIT are illustrated.

6.2 Selection of Potential Parameter

As discussed in Section 2-8, for the study of BIT, three sets of potential parameters were chosen to capture the short-range interaction. They all had same Bi-O and O-O interactions but different Ti-O parameters. Table 2-4, has all the parameters. They are given again below for quick reference.

Table 6-2. Short range potential parameters for $\text{Bi}_4\text{Ti}_3\text{O}_{12}$ [65, 67] (Repeat of Table 2-4)

Species	A (eV)	$\rho(\text{\AA})$	C (eV \AA^6)
$\text{Bi}^{+3}\text{-O}^{-2}$	49529.4	0.2223	0.00
$\text{O}^{-2}\text{-O}^{-2}$	9547.96	0.2192	32.0
2131	2131.04	0.3038	0.00
$\text{Ti}^{+4}\text{-O}^{-2}$	760	760.47	0.3879
2549	2549.4	0.2989	0.00

These interactions are used to calculate to calculate structural properties of BIT. To check the quality of parameter sets, they are compared with experimental values as shown in Table 6-3.

As explained in Chapter-2, interaction potentials are the back bone of MD simulation. Interaction potentials are developed in order to reproduce material properties by simulation. Based on the Table 6-2, all interaction parameters overestimate the system volume. Interactions 760 and 2549, overestimated the volume

by ~2-5%. Whereas for interaction 2131, the simulated volume is within 0.05% of experimental value. This simple comparison of structural features to the experiment provides us an opportunity to choose the best-fit interaction parameters. Bearing this in mind, all the further simulations are performed using 2131 potential parameters.

Table 6-3. Comparison of interaction parameters for BIT

	2131	760	2549	Exp. [118]
a(Å)	5.42	5.53	5.48	5.45
b(Å)	5.34	5.46	5.43	5.41
c(Å)	33.41	33.43	33.35	32.83
α	90.00	90.00	90.00	90.00
β	89.93	90.16	89.90	90.00
γ	90.00	89.99	89.99	90.00
Vol. (Å ³)	968.29	1009.06	992.46	967.98

6.3 Thermal Expansion

At low temperature ($T < 900$ K), BIT has monoclinic structure with all the crystallographic angles of 90° . Confusion arises because of the conventional classification of the crystal systems. If all the angles are 90° and sides are not equal, it is classified as orthorhombic and not monoclinic. However, there are symmetry operations tied with each system. The orthorhombic B2cb space group has 2-fold rotation, a 2_1 screw axis, mirror plane and glide plane symmetries whereas B1a1 has only mirror and glide as symmetry elements. So even though description of lattice features leads to the conclusion of BIT being orthorhombic, when combined with symmetry considerations it is clearly monoclinic.

The thermal expansion is simulated for the NPT ensemble. Since the cut-off distance is $\sim 10\text{\AA}$, the smallest system is generated by building a structure of $6 \times 6 \times 1$ unit cells in the x, y and z directions. This supercell structure has dimension of $\sim 30\text{\AA}$ in each direction, and is shown below (Fig. 6-4). Figure 6-4 clearly shows the difference in tilting behavior of TiO_6 octahedra along x and y axes which can be represented as $a^0b\bar{c}$ in the Glazer notation (for details, please refer the Sec. 3.5) [138].

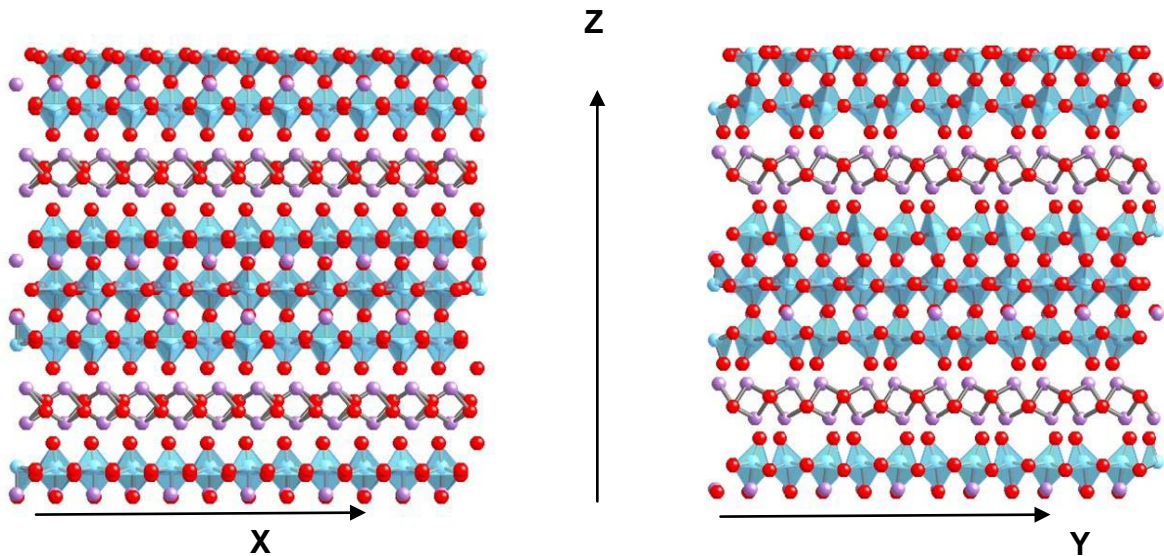


Figure 6-4. $6 \times 6 \times 1$ super cell of BIT viewed along x and y axes

The tilting of the TiO_6 octahedra in the pseudo-perovskite layer affects the Bi_2O_2 layer also. As seen in Fig. 6-4, the two layers are tilted in a similar fashion along the y-axis. The effect of octahedron tilting on lattice parameter becomes clear when the coefficient of thermal expansion along each direction is computed.

The normalized lattice parameters are compared for the different directions in Fig. 6-5. Table 6-4 compares the simulation values to the experimental studies.

Table 6-4. Comparison of thermal expansion values

Axis	Simulation ($\times 10^{-6}/\text{K}$)	Experiment ($\times 10^{-6}/\text{K}$)
X	5.14	10.1 [195]
Y	3.09	4.45 [195]
Z	3.77	0.20 [195], 16.12 [196]
Average	4.00	4.91 [195], 11 [197]

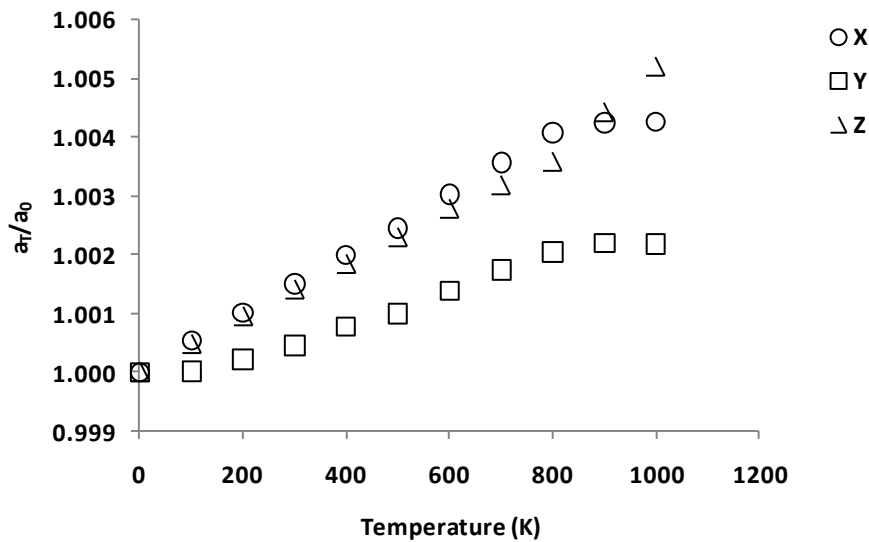


Figure 6-5. Coefficient of thermal expansion of BIT along x,y and z axes

Very few experiments have reported the thermal transport properties of BIT. The discrepancy among the experiments is larger than that between the simulation results in this work and experiment [195-197]. The experimental study by Hirata [195] was done to investigate the physics behind ferroelectric behavior of BIT near its Curie temperature. It reported that the a-axis (x-axis) displacement of Bi atom with respect to

TiO₆ octahedra in the perovskite layer is mainly responsible for ferroelectricity of BIT. The experimental investigations by Subbarao [197] were done on polycrystalline samples and mainly focused on to the structural changes around the Curie temperature of BIT (675⁰C). Another experimental study by Hirata *et al.* [195] found an average expansion value (4.9x10⁻⁶/K) similar to the one reported earlier by Subbarao (10x10⁻⁶/K) [197]. Due to this large variation among experiments, expansion coefficients are compared to the average value. Similar to the experiment findings, MD simulation also captures the anisotropy in expansion coefficients.

The strong difference between the x and y values of the thermal expansion is interesting and can be attributed to two structural features:

1. Octahedra tilting,
2. The difference in thermal expansion of the layers.

A very good description of octahedron tilting on lattice parameter is given by Megaw [137]. To compute the octahedra tilting effect, structural analysis is used in Crystalmaker. Since there is no tilt along x, only y and z tilts need be computed. An analysis tool is required to calculate the tilting of the octahedra. Due to the lack of any sophisticated analysis tool, tilting is calculated using the angle tool  in Crystalmaker.

As seen from Fig. 6-4, tilting of octahedra along Y-axis can be measured in two ways: inside-tilt (inset of Fig. 6-6 A) and outside-tilt (inset of Fig. 6-6 B). Both are measured and shown in Fig. 6-6.

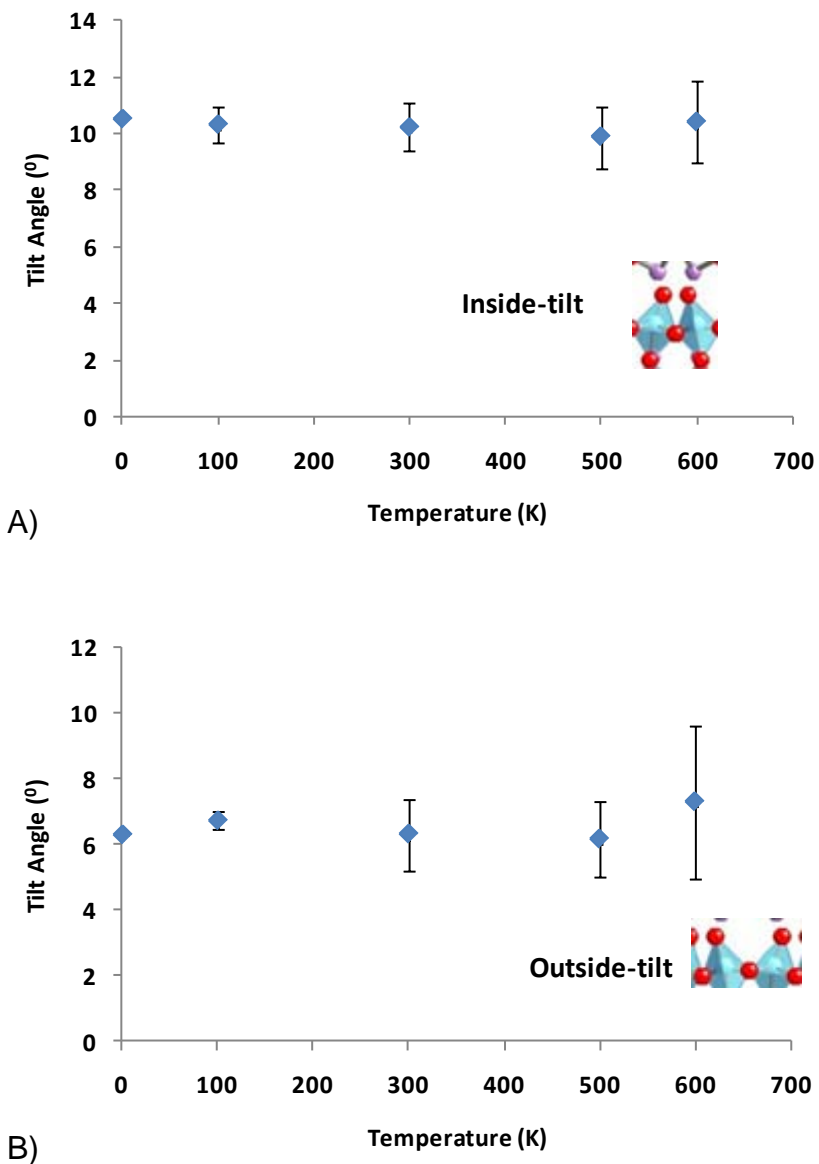


Figure 6-6. Temperature variation of tilt angles of A) Inside and B) Outside tilt of the octahedra along Y-axis (b-axis).

As seen in Fig. 6-6, there is negligible effect of temperature on octahedra tilting. The second structural feature of the layering is investigated to characterize the non-uniformity of the thermal expansion.

To measure expansion of different layers, the cation-cation distance is measured as a function of temperature. It is not trivial to resolve the distances in different direction.

The minimum separation between same cations in each layer can be used to compute thermal expansion of each layer. Again Crystallmaker is used to calculate the distances between the same cations of each layer. The methodology to calculate change in same type of closest cations is described below:

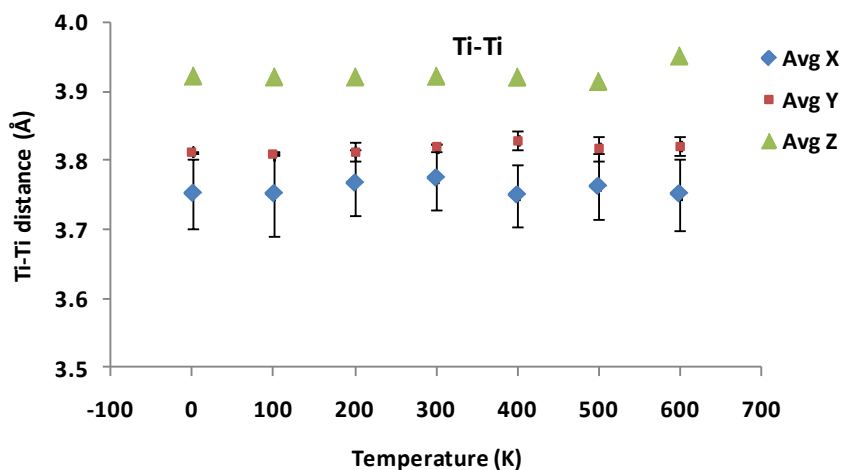


Figure 6-7. Temperature profile of nearest Ti-Ti distance in BIT structure

Pseudo-perovskite layer: Ti is only present in pseudo-perovskite layer, thus temperature profile of Ti-Ti smallest distance is used to compute thermal expansion of the layer. The distance between Ti-Ti is measured along both X and Y axes using Crystallmaker. Interatomic distance of closest Ti-Ti is calculated in each pseudo-perovskite layer. Average of the bond length at each temperature is taken and is shown in Fig. 6-8. Since there is only one layer to compute thermal expansion in Z-direction, no error bar is denoted for z-axis bond length.

Bi₂O₂ layer: Since Bi is present in both the layers, Bi-Bi is calculated separately for each layer. A system similar to that used for Ti-Ti bond calculation is used. Instead of masking Bi and O, Ti and O are masked. Bi-Bi temperature profile, shown in Fig. 6-8, is used to compute the thermal expansion of Bi₂O₂ layer.

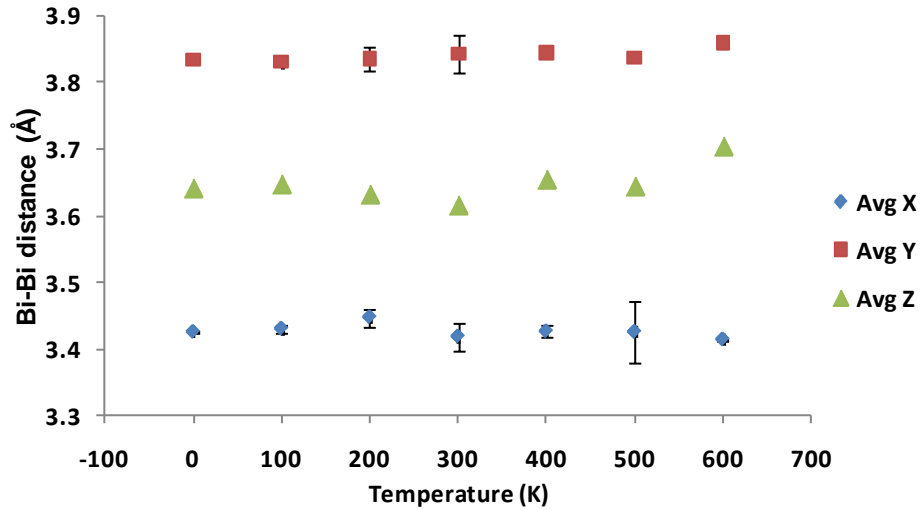


Figure 6-8. Temperature profile of Bi-Bi cation distance in Bi_2O_2 layer

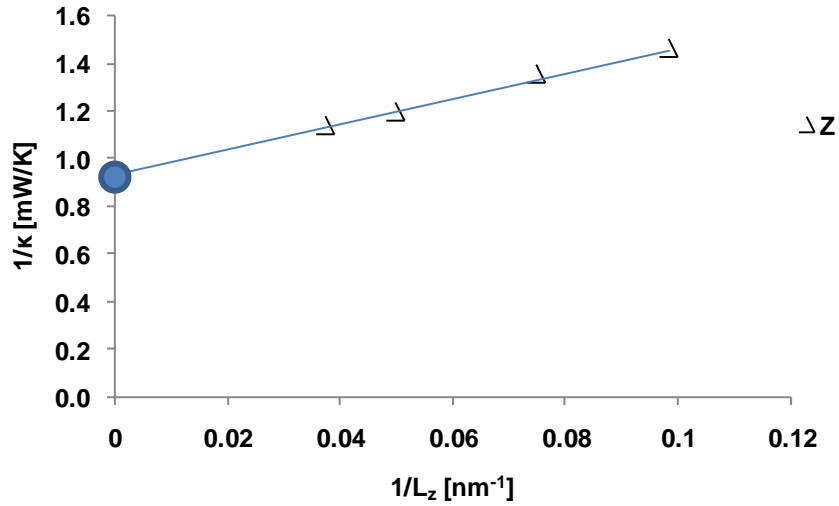
Analysis for both the layers provides some interesting insight into their response towards the temperature. But it is not trivial to suggest any effect of these layers on the overall thermal expansion. Besides the atomic disorder, density difference between layers might also play some role in the anisotropy of the heat transport properties of BIT. A detailed investigation to capture the effect of mass on thermal expansion gave no conclusive indication. The investigation is extended to observe the effect on thermal conductivity.

A recent experimental investigation of thermal transport properties of BIT by Shen et al. reasoned the density difference between layers was responsible for its low thermal conductivity [20]. The experimental study and the effect of density on thermal transport are discussed in detail in the following section.

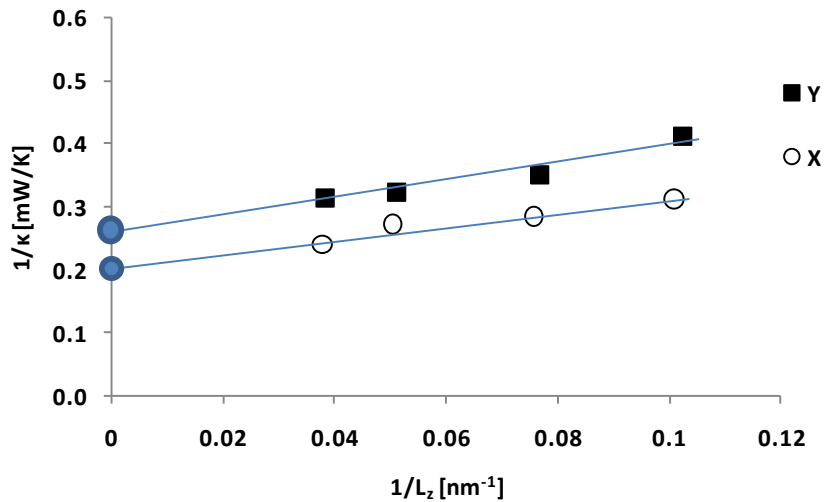
6.4 Thermal Conductivity

BIT exhibits anisotropic thermal conductivity. As discussed in sec. 2-3, BIT can be indexed as orthorhombic (because of its unique nature of being monoclinic with orthorhombic axes). The thermal conductivity can be written in matrix form as

$$\kappa = \begin{bmatrix} \kappa_{11} & 0 & 0 \\ 0 & \kappa_{22} & 0 \\ 0 & 0 & \kappa_{33} \end{bmatrix} \quad (6-1)$$



A)



B)

Figure 6-9. System size analysis for $T = 300$ K in all the direction A) x,y and z system size dependence B) x and y system size analysis only

The off-diagonal terms are zero because all the angles are 90° . The thermal conductivity is calculated in all three directions. As discussed in Chapter 2, it is necessary to perform system size analysis, from which the thermal conductivity values for the infinite system size are computed. As a representative example, the system size

analysis for $T = 300$ K is shown in Fig. 6-9. A similar system size analysis is performed at all the temperatures. The thermal conductivity for infinite system size systems are shown in Fig. 6-10.

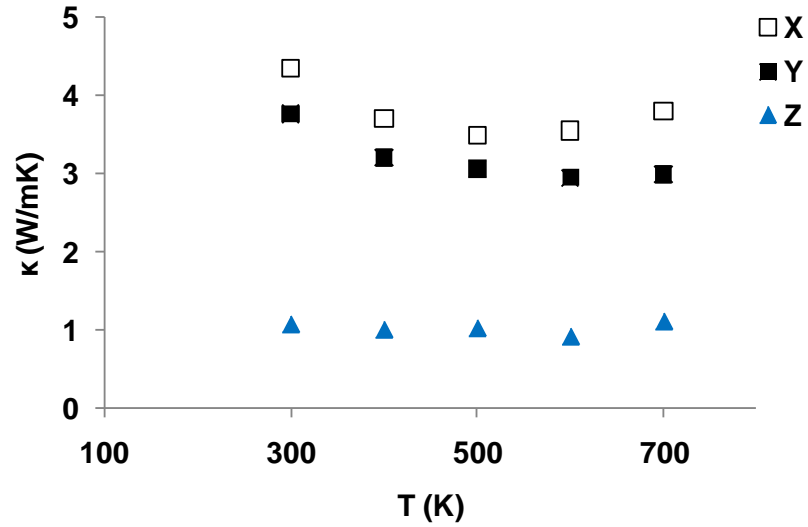


Figure 6-10. Temperature and direction dependence of thermal conductivity for BIT

Anisotropy in the thermal conductivity is very well captured by the simulation study. Experimental investigation of the thermal conductivity of BIT is shown in Fig. 6-11 and simulation does produce similar qualitative dependence of the thermal conductivity on temperature.

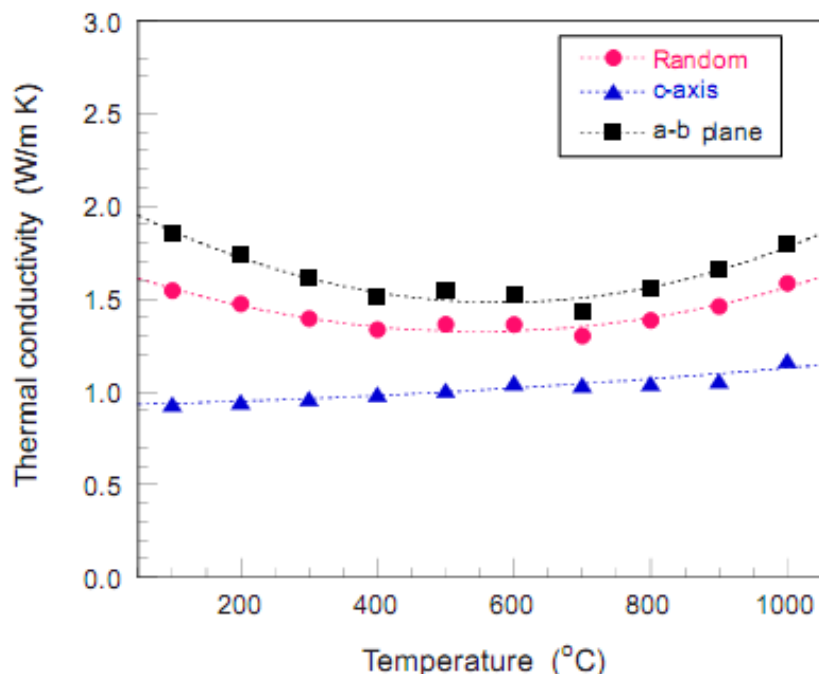


Figure 6-11. Thermal conductivity of BIT by experiment [20]

The experimental results are shown on Fig. 6-11 and need some explanation as figure in itself is not sufficient to explain its results. Experimentally, it is very hard to synthesize single crystal BIT, so results shown are of textured polycrystalline sample. In the experiment, two types of samples were prepared: i) c-axis textured sample and ii) random polycrystalline sample.

The thermal diffusivity was measured using the thermal flash method [82] and thermal conductivity is calculated using Eq. 2-41. Reported experimental sample densities (textured: 7882 kg m^{-3} , random: 7590 kg m^{-3}) were lower than the theoretical value (8040 kg m^{-3}).

The thermal conductivity from the random sample is shown by filled circles and the textured sample with filled triangles in Fig. 6-11. It has been assumed in the experiment that the thermal conductivity along *a* and *b* axes is the same and is shown by filled

squares (a-b plane) in Fig. 6-11. Since the thermal conductivity along a and b axes is the same, Eq. 6-1 can be written as

$$\kappa = \begin{bmatrix} \kappa_{ab} & 0 & 0 \\ 0 & \kappa_{ab} & 0 \\ 0 & 0 & \kappa_{cc} \end{bmatrix} \quad (6-2)$$

If random polycrystalline sample has thermal conductivity κ_p , it can be written in the form of axial thermal conductivities as:

$$\kappa_p = \frac{1}{3}(2\kappa_{ab} + \kappa_{cc}) \quad (6-3)$$

Since experimentally, κ_p and κ_{cc} is measured, κ_{ab} can be calculated as:

$$\kappa_{ab} = \frac{1}{2}(3\kappa_p - \kappa_{cc}) \quad (6-4)$$

The calculated data for thermal conductivity along a-b plane is shown as filled squares in Fig. 6-10. The thermal conductivity results from the experiment and simulation are in qualitative agreement. A theoretical discussion on thermal conductivity behavior over temperature gives the $1/T^n$ dependence. This temperature dependence corresponds to a decrease in thermal conductivity values with temperature for non metals.

An increase in the thermal conductivity at high temperatures ($T > 800$ K) is seen in Fig. 6-11. This is attributed to radiative component of the thermal transport. Contribution of this radiative component of heat transfer in BIT thermal conductivity increases the apparent thermal conductivity of the material beyond 800 K.

Density Effect on Thermal Conductivity: As explained in Section 6.1, low thermal conductivity materials are needed for TBC applications. The motivation behind

this analysis is to understand the factors contributing towards lowering the thermal conductivity of BIT and then to exploit them to reduce the thermal conductivity value even lower. Clarke has described, a minimum thermal conductivity value expression based on material's elastic and structural properties [194]:

$$\kappa_{\min} \propto \frac{m^{2/3} \rho^{1/6} E^{1/2}}{M^{2/3}} \quad (6-5)$$

Where, M is the molecular mass, m is the number of atoms per molecule. The expression of 6-2, changes different atomic masses to effective mass and that leads to absence of optical phonons in the material. Overall effects of this assumption are unknown but this underestimates thermal conductivity.

As shown in experiment thermal conductivity (Fig. 6-11), even after the phase change in BIT, the thermal conductivity does not change much. This reflects the limited role of specific atomic arrangements on thermal conductivity in BIT. When the phonon mean free path is calculated in the limit of high temperature, it gives a value of 0.24 nm (half of interatomic spacing 0.46 nm) [20]. Since there is no ionic disorder present in the system and atomic disorder has a very limiting effect on thermal conductivity, the low thermal conductivity is attributed to the scattering of phonons from the superlattice of alternating pseudo-perovskite and Bi₂O₂ [20]. The density of Bi₂O₂ fluorite-like block is 11,397 kg m⁻³ and the thickness is 0.45 nm, whereas the perovskite block has a density of 6487 kg m⁻³ with a thickness of 1.21 nm. This density difference becomes larger in low temperature structure. Since MD simulation gives total control over structure and its features, the density effect can be easily probed. The effect of the density difference is investigated in a systematic manner.

In the BIT structure, the PP layer is less dense than the BO layer. A simple method to probe the density effect on thermal conductivity of BIT is described below:

1. The PP layer is made heavier by increasing the mass of Ti (HT)
2. The PP layer is made heavier by increasing the mass of Bi only in PP layer (PPB)
3. The BO layer is made lighter by reducing the mass of Bi in BO layer only (LB).

A simple schematic is shown below of the above methodology (Fig. 6-12). The density of BO and PP layers are denoted by d_1 and d_2 , respectively. In the case of HT, the masses of the Ti in PP layer are artificially increased and since there is no Ti in BO layer, this captures the effect of mass only. The other two procedures, LB and PPB, involve changing mass of Bi only in BO layer or in PP layers that introduces two different kinds of Bi in the system. Thus these two scenarios include the effect of extra scattering sites along with the mass effect.

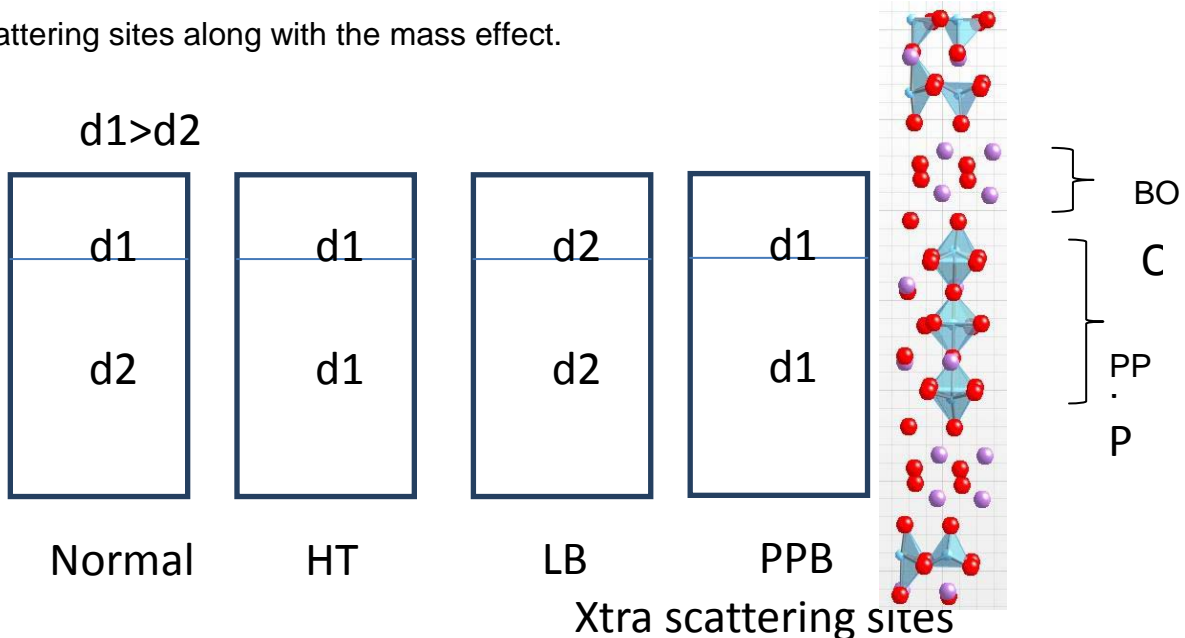


Figure 6-12. Schematic of method to investigate the density effect on thermal conductivity of BIT

At room temperature, all the above systems were compared for their respective values of thermal conductivity. Anisotropic nature of thermal conductivity allows us to choose between x, y or z axes thermal conductivity values to compare the effect of density on thermal conductivity. Thermal conductivity along the z axis is expected to reflect the effect of density more than x or y axis. Since dependence along x or y axis is expected to be same. The effect of the density is captured along the x and the z axis. The temperature is set at 300 K for the comparison. A system size analysis is performed at $T=300$ K for the thermal conductivity in x direction for all the systems and the comparisons are shown in Fig. 6-13.

Figure 6-13 shows a systematic system size dependence on all the systems along the x-axis, but it does not become clear what the effect of density on thermal conductivity is. After extracting the infinite thermal conductivity for all the systems, the result is shown in Table 6-3.

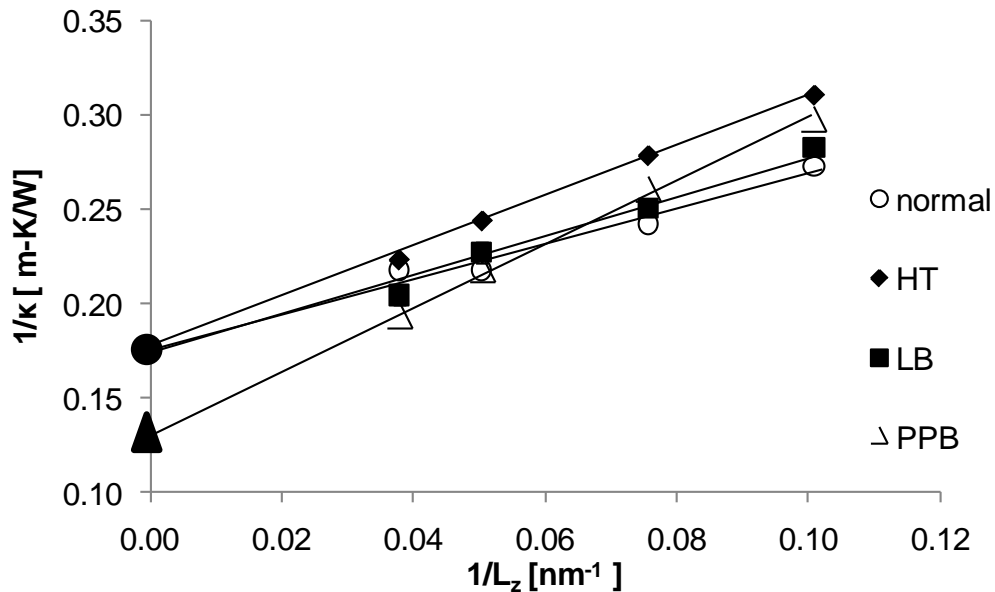


Figure 6-13. System size and density dependence of thermal conductivity for BIT

Table 6-5. Thermal conductivity variation for all 4 systems

System	κ (W/m-K)
Normal	5.63
LB	5.86
HT	5.78
PPB	7.16

The effect along the z-axis is more prominent as shown in Fig. 6-14. As expected, density difference is responsible for the low value of the thermal conductivity of BIT. Both the cases, PPB and HT increase the density of PP layer to be equal to the BO layer. If density was the only reason for the low value of thermal conductivity, the thermal conductivity increase should have been same for PPB and HT scenarios. The increase in the thermal conductivity is larger for HT case than PPB. The PPB scenario has two types of Bi in the system and that reflects as point defect in the system. The density increases the thermal conductivity value but presence of point defects lower the overall increase in the thermal conductivity. Whereas in HT, mass of all the Ti increases, thus no point defects are created in the system. That is why, a larger increase is observed in the case of HT than PPB and this absolute increase can be attributed to the density effect.

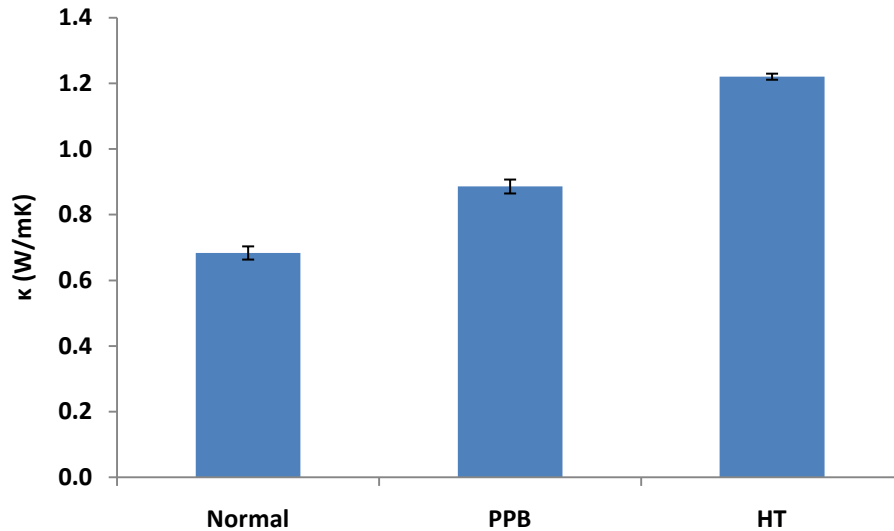


Figure 6-14. Density effect on the thermal conductivity along the z-axis in BIT

6.5 Conclusion and Future Study

Structural constraints and their effect on thermal transport properties are well documented and investigated by the MD simulation. A suitable potential parameter is chosen based on its performance to reproduce structural features of BIT.

Using the potential, anisotropy in thermal expansion was shown. The octahedron tilting was found to be temperature independent. Anisotropy in thermal conductivity qualitatively agreed with experimental investigation. Density difference between layers is attributed to the low value of thermal conductivity. A systematic investigation revealed the contribution of density effect and point defects on the thermal conductivity along the z-axis. No density effect was observed along the x axis. It can be concluded that by the introduction of point defects in the system, thermal conductivity can be lowered.

CHAPTER 7 GENERAL CONCLUSIONS

In this work, the molecular dynamics (MD) simulation method has been successfully used to investigate thermal transport in potential inert matrix fuel materials (MgO-NDZ and MgAl₂O₄) and thermal barrier coating material (Bi₄Ti₃O₁₂).

7.1 MgO-NDZ

As a candidate of inert matrix fuel, interfaces play a dominant role on thermal conductivity in composite systems. In this dissertation, it was determined that volumetric composition governs the thermal transport at very fine (<10 nm) grain size level for MgO-NDZ composite. The composite can have MgO-NDZ, MgO-MgO and NDZ-NDZ interfaces. Homogenous interfaces were investigated by simulating MgO and NDZ polycrystals separately. Using thermal conductivity values of polycrystals and single crystal, interface effects were computed for both materials. For very fine grain size, interface effects were comparable to the grain size, itself.

Due to the limitation of MD simulations, grain sizes were limited in tens of angstroms. Even with limited computational power, polycrystal thermal conductivity results were extrapolated for larger grain sizes and gave similar grain size dependence in comparison with the experiment results for YSZ [19].

Fidelity with experiment provides an additional tool to rectify the simulation data. Anharmonic analysis was used to quantify the fidelity of the interatomic interaction parameters of the simulation. Based on the difference from experiment for thermal expansion and bulk modulus, a correction term was calculated. The correction term quantified the deviation in thermal conductivity results for the material.

The study provides a key insight into the interface effects on thermal conductivity of MgO-NDZ composite. However, the study was limited to <10 nm grain size compared to micrometer size grains observed experimentally. Therefore, a systematic study with larger grain size of MgO, NDZ and MgO-NDZ system will provide additional insight into the thermal properties. Defects generally act as a barrier to thermal conduction. It will be interesting to capture the coupling of defect-grain boundary interactions on thermal conductivity of MgO-NDZ cercer.

7.2 MgAl₂O₄

With relative ease of formation of inverted structure (cation anti-site structure) in MgAl₂O₄ under neutron irradiation, effect on thermal and mechanical properties is an important issue. Experimentally temperature and inversion are interrelated, thus separating out one effect from another is extremely hard. Atomic-level simulation provided an ideal tool to capture the individual effects in the MgAl₂O₄ system.

Experimentally MgAl₂O₄ system has been characterized for $i < 0.3$. Using MD simulation, the entire range of inversion ($i = 0-1$) has been probed for thermal and mechanical properties. Thermal expansion has shown no variance for $i < 0.5$ and decreases afterwards. Similarly, analysis on bulk modulus has shown no change for $i < 0.5$ and increases for $i > 0.5$.

Using the above response of inversion on thermal expansion and bulk modulus, thermal conductivity was predicted. Thermal conductivity values were also calculated independently for each inversion using non-equilibrium MD (using heat source, heat sink). Critical analysis of the thermal conductivity values calculated by both methods showed the inability of the existing model in capturing the inversion effect.

“Combinatorics analysis” method has been used to incorporate the inversion effect on thermal properties.

Additionally, experimental and simulation observations on lattice parameters of MgAl_2O_4 has shown a decrease with inversion. However, the effect has not been properly characterized. For the first time, this study explained the reason for decrease of the lattice parameter with inversion. Besides, the study also presented a possible cation arrangement for 1 cation anti-site pair.

Another interesting question is to check whether the existing inversion enhances or reduces further disordering of the system. For $i < 0.5$, no change in further disorder of the system has been reported, however for $i > 0.5$, further disorder is facilitated. Low formation energy of additional anti-sites for $i > 0.5$ has been reported and explained through the formation of strain dipoles at inverted sites and simple reaction rate analysis model.

The present study has considered the arrangement of atoms in a spinel structure. However, defected rocksalt structure is also a possible arrangement of atoms for MgAl_2O_4 . Therefore, for a complete understanding of the thermo-elastic properties, it is essential to characterize and compare both spinel and defected rocksalt arrangements of MgAl_2O_4 . Similar to MgO-NDZ system, effect of interfaces on thermo-elastic properties can be characterized.

7.3 $\text{Bi}_4\text{Ti}_3\text{O}_{12}$

$\text{Bi}_4\text{Ti}_3\text{O}_{12}$ (BIT), a layered perovskite material, is a candidate material for thermal barrier coating (TBC) applications. The layering in BIT alternates between Bi_2O_2 and perovskite-like layers. Due to the presence of these layers, thermal conductivity results

in low values for BIT. This study focused on the fundamental understanding of the low value of the thermal conductivity of BIT.

An experimental study reported that the difference in the density of the layers guides the overall thermal conductivity of BIT [20]. In order to investigate the effect of density, simulations were performed by varying the mass of the cations in an appropriate manner. Due to the layered structure of BIT, anisotropy in thermal properties is reported in the literature. The current calculations also captured the anisotropic behavior in thermal conductivity and expansion.

Since BIT is a potential material for TBC applications mainly due to its low thermal conductivity, it is desired to further reduce its thermal conductivity. Characterization of the effects of intrinsic and extrinsic defects (like La [198]) on the thermal conductivity of BIT is essential. Diffusion of oxygen ion in BIT is also an important criterion for TBC application. Thus, characterization of ionic diffusion in BIT will provide a better understanding of the material for TBC application.

Overall, molecular dynamics is a very useful tool in characterizing atomic level details of various materials. This study successfully characterized the thermal transport properties of various oxide materials for their potential application as inert matrix fuel (MgO-NDZ, MgAl₂O₄) and thermal barrier coating (Bi₄Ti₃O₁₂).

LIST OF REFERENCES

- [1] "Annual Energy Review 2008 Prepared by Energy Information Administration," Washington, D.C., 2009.
- [2] D. Bodansky, "Global Warming and Nuclear-Power," *Nucl. Eng. Des.*, vol. 136, pp. 7-15, 1992.
- [3] P. Brohan, J. J. Kennedy, I. Harris, S. F. B. Tett, and P. D. Jones, "Uncertainty Estimates in Regional and Global Observed Temperature Changes: A New Data Set from 1850," *Journal of Geophysical Research-Atmospheres*, vol. 111, pp. D12106, 2006.
- [4] "Climate Change 2007: Synthesis Report," 2007.
- [5] U. E. P. Agency, "Inventory of U. S. Greenhouse Gas Emission and Sinks," April 15, 2010.
- [6] "IPCC, 2007: Summary for Policymakers. In: Climate Change 2007: The Physical Science Basis Contribution of Working Group I to the Fourth Assessment Report of the Intergovernmental Panel on Climate Change," S. Solomon, D. Qin, M. Manning, Z. Chen, M. Marquis, K.B. Averyt, M. Tignor and H.L. Miller, Ed., Cambridge University Press, Cambridge, United Kingdom and New York, NY, USA, 2007.
- [7] J. A. Turner, "A Realizable Renewable Energy Future," *Science*, vol. 285, pp. 687-689, 1999.
- [8] N. Lior, "Energy Resources and Use: The Present Situation and Possible Paths to the Future," *Energy*, vol. 33, pp. 842-857, 2008.
- [9] B. Comby, "Environmentalists for Nuclear Energy: <http://www.ecolo.org>," 1996.
- [10] J. Lovelock, *Revenge of Gaia*, UK, Allen Lane, 2006
- [11] W. N. Association, "Nuclear Reactors: <http://www.World-Nuclear.Org/Info/Inf32.htm>," 2009.
- [12] H. Matzke, V. V. Rondinella, and T. Wiss, "Materials Research on Inert Matrices: A Screening Study," *J. Nucl. Mater.*, vol. 274, pp. 47-53, 1999.
- [13] H. R. Trelue, "Safety and Neutronics: A Comparison of MOX Vs UO₂ Fuel," *Prog. Nucl. Energy*, vol. 48, pp. 135-145, 2006.
- [14] P. G. Medvedev, "Development of Dual-Phase Magnesia-Zirconia Ceramics for Light Water Reactor Inert Matrix Fuel," Texas A&M University, 2004.

- [15] P. G. Medvedev, S. M. Frank, T. P. O'Holleran, and M. K. Meyer, "Dual Phase MgO-ZrO₂ Ceramics for Use in Lwr Inert Matrix Fuel," *J. Nucl. Mater.*, vol. 342, pp. 48-62, 2005.
- [16] S. J. Yates, P. Xu, J. Wang, J. S. Tulenko, and J. C. Nino, "Processing of Magnesia-Pyrochlore Composites for Inert Matrix Materials," *J. Nucl. Mater.*, vol. 362, pp. 336-342, 2007.
- [17] D. R. Olander, *Fundamental Aspects of Nuclear Reactor Fuel Elements*, Springfield, Virginia, Technical Information Center, Energy Research and Development Administration, page 132, 1985
- [18] H. Matzke, "Radiation Damage in Nuclear Fuel Materials: The 'Rim' Effect in UO₂, and Damage in Inert Matrices for Transmutation of Actinides," *Nuclear Instruments and Methods in Physics Research B*, vol. 116, pp. 121-125, 1996.
- [19] H. S. Yang, G. R. Bai, L. J. Thompson, and J. A. Eastman, "Interfacial Thermal Resistance in Nanocrystalline Ytria-Stabilized Zirconia," *Acta Mater.*, vol. 50, pp. 2309-2317, 2002.
- [20] Y. Shen, D. R. Clarke, and P. A. Fuierer, "Anisotropic Thermal Conductivity of the Aurivillius Phase, Bismuth Titanate, (Bi₄Ti₃O₁₂): A Natural Nanostructured Superlattice," *Appl. Phys. Lett.*, vol. 93, pp. 102907: 1-3, 2008.
- [21] R. V. Meter, "System Software / Operating Systems:
<http://web.sfc.keio.ac.jp/~rdv/keio/sfc/teaching/System-Software/System-Software-2008-Prod/Lec01.html>," 2008.
- [22] S. Natarajan *et al.*, "A 32nm Logic Technology Featuring 2nd-Generation High-K + Metal-Gate Transistors, Enhanced Channel Strain and 0.171 μm² Sram Cell Size in a 291mb Array," *IEDM*, 2008.
- [23] S. Borkar, "Low Power Design Challenges for the Decade," presented at Proc Design Automation Conference, 2001.
- [24] C. K. Gupta, *Materials in Nuclear Energy Applications*, Boca Raton, 1989
- [25] D. D. Hass, "Directed Vapor Deposition of Thermal Barrier Coatings," Ph.D. Thesis, University of Virginia, 2000.
- [26] Ritter, "Modes of Heat Transfer:
http://www.Uwsp.Edu/Geo/Faculty/Ritter/Geog101/Uwsp_Lectures/Lecture_Radiation_Energy_Concepts.html."
- [27] W. Jones and N. H. March, *Theoretical Solid State Physics*, New York, Dover, 1985

- [28] H. Rosenberg, *The Solid State*, Oxford University, page 2004
- [29] N. W. Ashcroft and N. D. Mermin, *Solid State Physics*, Saunders College Publishing, page 1976
- [30] C. Kittel, *Introduction to Solid State Physics*, 7th ed, New York, John Wiley & Sons Inc., page 126, 2000
- [31] P. G. Klemens, *Solid State Physics 7*, page 45-46, 1958
- [32] G. P. Srivastava, *The Physics of Phonons*, 1 ed, Taylor & Francis, page 122, 1990
- [33] Wikipedia, "Phonon N and U Process:
http://Commons.Wikimedia.Org/Wiki/File:Phonon_Nu_Process.Png," 2009.
- [34] J. Callaway, "Model for Lattice Thermal Conductivity at Low Temperatures," *Phys. Rev.*, vol. 113, pp. 1046-1051, 1959.
- [35] C. J. Adkins, *Equilibrium Thermodynamic*, 2nd ed, London, McGraw-Hill, 1975
- [36] J. M. Ziman, *Electrons and Phonons*, London, UK, Oxford University Press, 1960
- [37] R. E. Peierls, *Quantum Theory of Solids*, Oxford, 1955
- [38] C. Herring, "Role of Low-Energy Phonons in Thermal Conduction," *Phys. Rev.*, vol. 95, pp. 954-965, 1954.
- [39] J. Elliott, "Multiscale Modelling: http://www.srcf.ucam.org/~jae1001/ccp5_2007," 2007.
- [40] R. M. Martin, *Electronic Structure - Basic Theory and Practical Methods*, Cambridge, 2004
- [41] R. D. Cook, D. S. Malkus, M. E. Plesha, and R. J. Witt, *Concepts and Applications of Finite Element Analysis*, New York, 2001
- [42] T. C. Germann and K. Kadau, "Trillion-Atom Molecular Dynamics Becomes a Reality," *International Journal of Modern Physics C*, vol. 19, pp. 1315-1319, 2008.
- [43] W. H. Press, B. P. Flannery, S. A. Teukolsky, and W. T. Vetterling, *Numerical Recipes in Fortran 77*, Cambridge, Cambridge University Press, 1992
- [44] M. P. Allen and D. J. Tildesley, *Computer Simulation of Liquids*, Oxford University Press, page 82, 1987

- [45] L. Verlet, "Computer Experiments on Classical Fluids.I. Thermodynamical Properties of Lennard-Jones Molecules," *Phys. Rev.*, vol. 159, pp. 98-103, 1967.
- [46] C. W. Gear, *Numerical Initial Value Problems in Ordinary Differential Equations.*, New Jersey, Englewood Cliffs, 1971
- [47] O. Teleman and B. Jonsson, "Vectorizing a General-Purpose Molecular-Dynamics Simulation Program," *J. Comput. Chem.*, vol. 7, pp. 58-66, 1986.
- [48] M. E. Tuckerman, B. J. Berne, and A. Rossi, "Molecular-Dynamics Algorithm for Multiple Time Scales - Systems with Disparate Masses," *J. Chem. Phys.*, vol. 94, pp. 1465-1469, 1991.
- [49] B. Cartling, "From Short-Time Molecular-Dynamics to Long-Time Stochastic Dynamics of Proteins," *J. Chem. Phys.*, vol. 91, pp. 427-438, 1989.
- [50] ISSAC, "PBC," <http://isaacs.sourceforge.net/phys/pbc.html>.
- [51] P. P. Ewald, "The Calculation of Optical and Electrostatic Grid Potential," *Ann. Phys.*, vol. 64, pp. 253-287, 1921.
- [52] D. Wolf, P. Keblinski, S. R. Phillpot, and J. Eggebrecht, "Exact Method for the Simulation of Coulombic Systems by Spherically Truncated, Pairwise r^{-1} Summation," *J. Chem. Phys.*, vol. 110, pp. 8254-8282, 1999.
- [53] D. Fincham, "Optimization of the Ewald Sum for Large Systems," *Mol. Simul.*, vol. 13, pp. 1-9, 1994.
- [54] H. M. Evjen, "On the Stability of Certain Heteropolar Crystals," *Phys. Rev.*, vol. 39, pp. 675-687, 1932.
- [55] J. H. R. Clarke, W. Smith, and L. V. Woodcock, "Short-Range Effective Potentials for Ionic Fluids," *J. Chem. Phys.*, vol. 84, pp. 2290-2294, 1986.
- [56] L. V. Woodcock, *Advances in Molten Salt Chemistry*, Edited by J. Braunstein, G. Mamantov, and G. P. Smith, New York, Plenum, 1975
- [57] D. Wolf, "Reconstruction of NaCl Surfaces from a Dipolar Solution to the Madelung Problem," *Phys. Rev. Lett.*, vol. 68, pp. 3315-3318, 1992.
- [58] J. E. Lennard-Jones, "On the Determination of Molecular Fields," *Proc. Roy. Soc. Lond. Math. Phys. Sci.*, vol. 106, pp. 463-477, 1924.
- [59] F. H. Stillinger and T. A. Weber, "Computer Simulation of Local Order in Condensed Phases of Silicon," *Phys. Rev. B*, vol. 31, pp. 5262-5271, 1985.

- [60] R. A. Buckingham, "The Classical Equation of State of Gaseous Helium, Neon and Argon," *Proc. Roy. Soc. Lond. Math. Phys. Sci.*, vol. 168, pp. 264-283, 1938.
- [61] J F Ziegler, J P Biersak, and U. Littermak, *The Stopping and Range of Ions in Matter*, New York, Pergomon, 1985
- [62] L. Minervini, R. W. Grimes, Y. Tabira, R. L. Withers, and K. E. Sickafus, "The Oxygen Positional Parameter in Pyrochlores and Its Dependence on Disorder," *Philos. Mag. A*, vol. 82, pp. 123-135, 2002.
- [63] P. K. Schelling, S. R. Phillpot, and D. Wolf, "Mechanism of the Cubic-to-Tetragonal Phase Transition in Zirconia and Yttria-Stabilized Zirconia by Molecular-Dynamics Simulation," *J. Am. Ceram. Soc.*, vol. 84, pp. 1609-1619, 2001.
- [64] J. A. Ball, M. Pirzada, R. W. Grimes, M. O. Zacate, D. W. Price, and B. P. Uberuaga, "Predicting Lattice Parameter as a Function of Cation Disorder in $MgAl_2O_4$ Spinel," *J. Phys.: Condens. Matter*, vol. 17, pp. 7621-7631, 2005.
- [65] C. Pirovano, M. S. Islam, R. N. Vannier, G. Nowogrocki, and G. Mairesse, "Modelling the Crystal Structures of Aurivillius Phases," *Solid State Ionics*, vol. 140, pp. 115-123, 2001.
- [66] M. O. Zacate, R. W. Grimes, and K. Scrivener, "Predicted Calcium Titanate Solution Mechanisms in Calcium Aluminoferrite and Related Phases," *J. Mater. Sci.*, vol. 35, pp. 3727-3732, 2000.
- [67] A. Snedden, P. Lightfoot, T. Dinges, and M. S. Islam, "Defect and Dopant Properties of the Aurivillius Phase $Bi_4Ti_3O_{12}$," *J. Solid State Chem.*, vol. 177, pp. 3660-3665, 2004.
- [68] B. G. Dick and A. W. Overhauser, "Theory of the Dielectric Constants of Alkali Halide Crystals," *Phys. Rev.*, vol. 112, pp. 90-103, 1958.
- [69] P. H. Hünenberger, "Thermostat Algorithms for Molecular Dynamics Simulations," *Adv. Polym. Sci.*, vol. 173, pp. 105-149, 2005.
- [70] H. C. Andersen, "Molecular Dynamics Simulations at Constant Pressure and/or Temperature," *J. Chem. Phys.*, vol. 72, pp. 2384-2393, 1980.
- [71] M. Parrinello and A. Rahman, "Crystal Structure and Pair Potentials: A Molecular-Dynamics Study," *Phys. Rev. Lett.*, vol. 45, pp. 1196-1199, 1980.

- [72] F. Zipoli, M. Bernasconi, and R. Martoňák, "Constant Pressure Reactive Molecular Dynamics Simulations of Phase Transitions under Pressure: The Graphite to Diamond Conversion Revisited," *Eur. Phys. J. B*, vol. 39, pp. 41-47, 2004.
- [73] D. Y. Sun and X. G. Gong, "A New Constant-Pressure Molecular Dynamics Method for Finite Systems," *J. Phys.: Condens. Matter*, vol. 14, pp. L487-L493, 2002.
- [74] R. Martoňák, A. Laio, and M. Parrinello, "Predicting Crystal Structures: The Parrinello-Rahman Method Revisited," *Phys. Rev. Lett.*, vol. 90, pp. 075503, 2003.
- [75] L. V. Woodcock, "Isothermal Molecular Dynamics Calculations for Liquid Salts," *Chem. Phys. Lett.*, vol. 10, pp. 257-261, 1971.
- [76] S. Nose, "A Unified Formulation of the Constant Temperature Molecular Dynamics Methods," *J. Chem. Phys.*, vol. 81, pp. 511-519, 1984.
- [77] S. Nose, "Constant-Temperature Molecular Dynamics," *J. Phys.: Condens. Matter*, vol. 2, pp. SA115-SA119, 1990.
- [78] W. G. Hoover, A. J. C. Ladd, and B. Moran, "High-Strain-Rate Plastic Flow Studied Via Nonequilibrium Molecular Dynamics," *Phys. Rev. Lett.*, vol. 48, pp. 1818-1820, 1982.
- [79] D. J. Evans and G. P. Morriss, "Isothermal-Isobaric Molecular Dynamics," *Chem. Phys.*, vol. 77, pp. 63-66, 1983.
- [80] J. M. Haile and S. Gupta, "Extensions of the Molecular Dynamics Simulation Method. II. Isothermal Systems," *J. Chem. Phys.*, vol. 79, pp. 3067-3076, 1983.
- [81] W. G. Hoover, "Canonical Dynamics: Equilibrium Phase-Space Distribution," *Phys. Rev. A*, vol. 31, pp. 1695-1697, 1985.
- [82] W. J. Parker, R. J. Jenkins, G. L. Abbott, and C. P. Butler, "Flash Method of Determining Thermal Diffusivity, Heat Capacity, and Thermal Conductivity," *J. Appl. Phys.*, vol. 32, pp. 1679-1684, 1961.
- [83] W. G. Hoover, *Computational Statistical Mechanics*, Amsterdam, Elsevier, 1991
- [84] A. Maiti, G. D. Mahan, and S. T. Pantelides, "Dynamical Simulations of Nonequilibrium Processes — Heat Flow and the Kapitza Resistance across Grain Boundaries," *Solid State Commun.*, vol. 102, pp. 517-521, 1997.

- [85] C. Oligschleger and J. C. Schön, "Simulation of Thermal Conductivity and Heat Transport in Solids," *Phys. Rev. B*, vol. 59, pp. 4125–4133, 1999.
- [86] P. Jund and R. Jullien, "Molecular-Dynamics Calculation of the Thermal Conductivity of Vitreous Silica," *Phys. Rev. B*, vol. 59, pp. 13707-13711, 1999.
- [87] A. Baranyai, "Heat Flow Studies for Large Temperature Gradients by Molecular Dynamics Simulation," *Phys. Rev. E*, vol. 54, pp. 6911-6917, 1996.
- [88] R. H. H. Poetzsch and H. Böttger, "Interplay of Disorder and Anharmonicity in Heat Conduction: Molecular-Dynamics Study," *Phys. Rev. B*, vol. 50, pp. 15757–15763, 1994.
- [89] M. J. Gillan and M. Dixon, "The Calculation of Thermal Conductivities by Perturbed Molecular Dynamics Simulation," *J. Phys. C: Solid State Phys.*, vol. 16, pp. 869-878, 1983.
- [90] S. Berber, Y.-K. Kwon, and D. Tománek, "Unusually High Thermal Conductivity of Carbon Nanotubes," *Phys. Rev. Lett.*, vol. 84, pp. 4613-4616, 2000.
- [91] G. V. Paolini, G. Ciccotti, and C. Massobrio, "Nonlinear Thermal Response of a Lennard-Jones Fluid near the Triple Point," *Phys. Rev. A*, vol. 34, pp. 1355-1362, 1986.
- [92] J. Che, T. Çağın, W. Deng, and W. A. Goddard, "Thermal Conductivity of Diamond and Related Materials from Molecular Dynamics Simulations," *J. Chem. Phys.*, vol. 113, pp. 6888-6900, 2000.
- [93] Ju Li, Lisa Porter, and S. Yip, "Atomistic Modeling of Finite-Temperature Properties of Crystalline B-SiC: II. Thermal Conductivity and Effects of Point Defects," *Journal of Nuclear Materials*, vol. 255, 1998.
- [94] S. G. Volz and G. Chen, "Molecular-Dynamics Simulation of Thermal Conductivity of Silicon Crystals," *Phys. Rev. B*, vol. 61, pp. 2651-2656, 2000.
- [95] Y. H. Lee, R. Biswas, C. M. Soukoulis, C. Z. Wang, C. T. Chan, and K. M. Ho, "Molecular-Dynamics Simulation of Thermal Conductivity in Amorphous Silicon," *Phys. Rev. B*, vol. 43, pp. 6573–6580, 1991.
- [96] A. J. C. Ladd, B. Moran, and W. G. Hoover, "Lattice Thermal Conductivity: A Comparison of Molecular Dynamics and Anharmonic Lattice Dynamics," *Phys. Rev. B*, vol. 34, pp. 5058–5064, 1986.
- [97] R. Vogelsang, C. Hoheisel, and G. Ciccotti, "Thermal Conductivity of the Lennard-Jones Liquid by Molecular Dynamics Calculations," *J. Chem. Phys.*, vol. 86, pp. 6371-6375, 1987.

- [98] Stephen E Smith and R. C. Campbell, "Flash Diffusivity Method: A Survey of Capabilities," *Electronics Cooling*, May 2002.
- [99] P. K. Schelling, S. R. Phillpot, and P. Keblinski, "Comparison of Atomic-Level Simulation Methods for Computing Thermal Conductivity," *Phys. Rev. B*, vol. 65, pp. 144306, 2002.
- [100] A. G. Kalinichev, J. D. Bass, B. N. Sun, and D. A. Payne, "Elastic Properties of Tetragonal PbTiO_3 Single Crystals by Brillouin Scattering," *J. Mater. Res.*, vol. 12, pp. 2623-2627, 1997.
- [101] N. F. M. Henry and K. Lonsdale, *International Tables for X-Ray Crystallography*, Birmingham, Kynoch Press, 1952
- [102] F. Seitz, *The Modern Theory of Solids*, Dover, page 736, 1987
- [103] D. G. Isaak, R. E. Cohen, and M. J. Mehl, "Calculated Elastic and Thermal-Properties of MgO at High-Pressures and Temperatures," *Journal of Geophysical Research-Solid Earth and Planets*, vol. 95, pp. 7055-7067, 1990.
- [104] M. A. Subramanian, G. Aravamudan, and G. V. S. Rao, "Oxide Pyrochlores - a Review," *Progress in Solid State Chemistry*, vol. 15, pp. 55-143, 1983.
- [105] S. Lutique, R. J. M. Konings, V. V. Rondinella, J. Somers, and T. Wiss, "The Thermal Conductivity of $\text{Nd}_2\text{Zr}_2\text{O}_7$ Pyrochlore and the Thermal Behaviour of Pyrochlore-Based Inert Matrix Fuel," *J. Alloys Compd.*, vol. 352, pp. 1-5, 2003.
- [106] R. B. Greigor, F. W. Lytle, B. C. Chakoumakos, G. R. Lumpkin, and R. C. Ewing, "An Investigation of Uranium L-Edges of Metamict and Annealed Betafite," presented at Materials Research Society Symposium Proceedings, 1985 Fall.
- [107] P. Xu, "Potential Inert Matrix Materials: Materials Synthesis and Evaluation of in-Service Engineering Parameters," PhD, University of Florida, 2009, pp. 31.
- [108] W. H. Bragg, "The Structure of the Spinel Group of Crystals.," *Philos. Mag.*, vol. 30, pp. 305-315, 1915.
- [109] S. Nishikawa, "Structure of Some Crystals of the Spinel Group," *Proc. Math. Phys. Soc. Tokyo*, vol. 8, pp. 199-209, 1915.
- [110] K. E. Sickafus, J. M. Wills, and N. W. Grimes, "Structure of Spinel," *J. Am. Ceram. Soc.*, vol. 82, pp. 3279-3292, 1999.
- [111] R. M. Hazen and H. X. Yang, "Effects of Cation Substitution and Order-Disorder on P-V-T Equations of State of Cubic Spinel," *Am. Mineral.*, vol. 84, pp. 1956-1960, 1999.

- [112] T. F. W. Barth and E. Posnjak, "Spinel Structures with and without Variate Atom Equipoints," *Zeitschrift Fur Kristallographie*, vol. 82, pp. 325-341, 1932.
- [113] E. Posnjak and T. F. W. Barth, "A New Type of Crystal Fine-Structure: Lithium Ferrite ($\text{Li}_2 \cdot \text{Fe}_2\text{O}_3$)," *Phys. Rev.*, vol. 38, pp. 2234-2239, 1931.
- [114] E. J. W. Verwey and E. L. Heilmann, "Physical Properties and Cation Arrangement of Oxides with Spinel Structures.1. Cation Arrangement in Spinel," *J. Chem. Phys.*, vol. 15, pp. 174-180, 1947.
- [115] M. A. Carpenter and E. K. H. Salje, "Thermodynamics of Nonconvergent Cation Ordering in Minerals.2. Spinel and the Ortho-Pyroxene Solid-Solution," *Am. Mineral.*, vol. 79, pp. 1068-1083, 1994.
- [116] R. J. Harrison and A. Putnis, "The Magnetic Properties and Crystal Chemistry of Oxide Spinel Solid Solutions," *Surveys in Geophysics*, vol. 19, pp. 461-520, 1998.
- [117] B. Aurivillius, "Mixed Bismuth Oxides with Layer Lattices.II. Structure of $\text{Bi}_4\text{Ti}_3\text{O}_{12}$," *Arkiv for Kemi*, vol. 1, pp. 499-512, 1950.
- [118] A. D. Rae, J. G. Thompson, and R. L. Withers, "Structure Refinement of Commensurately Modulated Bismuth Tungstate, Bi_2WO_6 ," *Acta Crystallographica Section B-Structural Science*, vol. 47, pp. 870-881, 1991.
- [119] Ismunandar, B. J. Kennedy, Gunawan, and Marsongkohadi, "Structure of $\text{ABi}_2\text{Nb}_2\text{O}_9$ (A=Sr, Ba): Refinement of Powder Neutron Diffraction Data," *J. Solid State Chem.*, vol. 126, pp. 135-141, 1996.
- [120] Ismunandar and B. J. Kennedy, "Effect of Temperature on Cation Disorder in $\text{ABi}_2\text{Nb}_2\text{O}_9$ (A=Sr, Ba)," *J. Mater. Chem.*, vol. 9, pp. 541-544, 1999.
- [121] M. M. Kumar, A. Srinivas, G. S. Kumar, and S. V. Suryanarayana, "Synthesis and Physical Properties of $\text{Bi}_5\text{Ti}_3\text{MnO}_{15}$," *Solid State Commun.*, vol. 104, pp. 741-746, 1997.
- [122] B. Aurivillius and P. H. Fang, "Ferroelectricity in Compound $\text{Ba}_2\text{Bi}_4\text{Ti}_5\text{O}_{18}$," *Phys. Rev.*, vol. 126, pp. 893-896, 1962.
- [123] A. D. Rae, J. G. Thompson, R. L. Withers, and A. C. Willis, "Structure Refinement of Commensurately Modulated Bismuth Titanate, $\text{Bi}_4\text{Ti}_3\text{O}_{12}$," *Acta Crystallogr., Sect. B: Struct. Sci.*, vol. 46, pp. 474-487, 1990.
- [124] R. Machado, M. G. Stachiotti, R. L. Migoni, and A. H. Tera, "First-Principles Determination of Ferroelectric Instabilities in Aurivillius Compounds," *Phys. Rev. B*, vol. 70, pp. 214112, 2004.

- [125] Y. I. Kim and M. K. Jeon, "Combined Structural Refinement of $\text{Bi}_4\text{Ti}_3\text{O}_{12}$ Using X-Ray and Neutron Powder Diffraction Data," *Mater. Lett.*, vol. 58, pp. 1889-1893, 2004.
- [126] C. H. Hervoches and P. Lightfoot, "A Variable-Temperature Powder Neutron Diffraction Study of Ferroelectric $\text{Bi}_4\text{Ti}_3\text{O}_{12}$," *Chem. Mater.*, vol. 11, pp. 3359-3364, 1999.
- [127] J. F. Dorrian, R. E. Newnham, M. I. Kay, and D. K. Smith, "Crystal-Structure of $\text{Bi}_4\text{Ti}_3\text{O}_{12}$," *Ferroelectrics*, vol. 3, pp. 17-27, 1971.
- [128] Y. Shimakawa, Y. Kubo, Y. Tauchi, H. Asano, T. Kamiyama, F. Izumi, and Z. Hiroi, "Crystal and Electronic Structures of $\text{Bi}_{4-x}\text{La}_x\text{Ti}_3\text{O}_{12}$ Ferroelectric Materials," *Appl. Phys. Lett.*, vol. 79, pp. 2791-2793, 2001.
- [129] Y. I. Kim, M. K. Jeon, and S. I. Woo, "Structural Study of $\text{Bi}_4\text{Ti}_3\text{O}_{12}$ Using Neutron Powder Diffraction Data," *J. Mater. Sci. Lett.*, vol. 22, pp. 1655-1657, 2003.
- [130] K. R. Chakraborty, S. N. Achary, S. J. Patwe, P. S. R. Krishna, A. B. Shinde, and A. K. Tyagi, "Low Temperature Neutron Diffraction Studies on $\text{Bi}_4\text{Ti}_3\text{O}_{12}$," *Ceram. Int.*, vol. 33, pp. 601-604, 2007.
- [131] A. Shrinagar, A. Garg, R. Prasad, and S. Auluck, "Phase Stability in Ferroelectric Bismuth Titanate: A First-Principles Study," *Acta Crystallogr., Sect. A: Found. Crystallogr.*, vol. 64, pp. 368-375, 2008.
- [132] T. Jardiel, A. C. Caballero, and M. Villegas, "Aurivillius Ceramics: $\text{Bi}_4\text{Ti}_3\text{O}_{12}$ -Based Piezoelectrics," *J. Ceram. Soc. Jpn.*, vol. 116, pp. 511-518, 2008.
- [133] J. M. Perez-Mato, P. Blaha, K. Schwarz, M. Aroyo, D. Orobengoa, I. Etxebarria, and A. Garcia, "Multiple Instabilities in $\text{Bi}_4\text{Ti}_3\text{O}_{12}$: A Ferroelectric Beyond the Soft-Mode Paradigm," *Phys. Rev. B*, vol. 77, pp. 184104, 2008.
- [134] R. E. Newnham, R. W. Wolfe, and J. F. Dorrian, "Structural Basis of Ferroelectricity in Bismuth Titanate Family," *Mater. Res. Bull.*, vol. 6, pp. 1029-1039, 1971.
- [135] W. Zhong and D. Vanderbilt, "Competing Structural Instabilities in Cubic Perovskites," *Phys. Rev. Lett.*, vol. 74, pp. 2587-2590, 1995.
- [136] E. C. Subbarao, "Systematics of Bismuth Layer Compounds," *Integrated Ferroelectrics: An International Journal*, vol. 12, pp. 33-41, 1996.
- [137] H. D. Megaw, "Thermal Expansion of Interatomic Bonds Illustrated by Experimental Evidence from Certain Niobates," *Acta Crystallogr. Sec. A*, vol. A 24, pp. 589-604, 1968.

- [138] A. M. Glazer, "Classification of Tilted Octahedra in Perovskites," *Acta Crystallogr., Sect. B: Struct. Sci.*, vol. B 28, pp. 3384-3392, 1972.
- [139] H. Kleykamp, "Selection of Materials as Diluents for Burning of Plutonium Fuels in Nuclear Reactors," *J. Nucl. Mater.*, vol. 275, pp. 1-11, 1999.
- [140] E. A. C. Neeft, K. Bakker, R. L. Belvroy, W. J. Tams, R. P. C. Schram, R. Conrad, and A. van Veen, "Mechanical Behaviour of Macro-Dispersed Inert Matrix Fuels," *J. Nucl. Mater.*, vol. 317, pp. 217-225, 2003.
- [141] N. Chauvin, T. Albiol, R. Mazoyer, J. Noirot, D. Lespiaux, J. C. Dumas, C. Weinberg, J. C. Menard, and J. P. Ottaviani, "In-Pile Studies of Inert Matrices with Emphasis on Magnesia and Magnesium Aluminate Spinel," *J. Nucl. Mater.*, vol. 274, pp. 91-97, 1999.
- [142] K. E. Sickafus, L. Minervini, R. W. Grimes, J. A. Valdez, M. Ishimaru, F. Li, K. J. McClellan, and T. Hartmann, "Radiation Tolerance of Complex Oxides," *Science*, vol. 289, pp. 748-751, 2000.
- [143] P. K. Schelling, S. R. Phillpot, and R. W. Grimes, "Optimum Pyrochlore Compositions for Low Thermal Conductivity," *Philos. Mag. Lett.*, vol. 84, pp. 127-137, 2004.
- [144] L. S. Dubrovinsky and S. K. Saxena, "Thermal Expansion of Periclase (MgO) and Tungsten (W) to Melting Temperatures," *Phys Chem Minerals*, pp. 547-550, 1997.
- [145] H. Lehmann, D. Pitzer, G. Pracht, R. Vassen, and D. Stover, "Thermal Conductivity and Thermal Expansion Coefficients of the Lanthanum Rare-Earth-Element Zirconate System," *J. Am. Ceram. Soc.*, vol. 86, pp. 1338-1344, 2003.
- [146] C. B. Basak, "Classical Molecular Dynamics Simulation of Uranium Monocarbide (UC)," *Computational Materials Science*, vol. 40, pp. 562-568, 2007.
- [147] A. Senyshyn, L. Vasylechko, M. Knapp, U. Bismayer, M. Berkowski, and A. Matkovskii, "Thermal Expansion of the Perovskite-Type NdGaO₃," *J. Alloys Compd.*, vol. 382, pp. 84-91, 2004.
- [148] M. W. Barsoum, *Fundamentals of Ceramics*, 2nd ed, Philadelphia, Institute of Physics, page 96, 2003
- [149] G. Leibfried and E. Schloemann, *Math-Physik*, Goettingen, page 71, 1954
- [150] T. Watanabe, S. B. Sinnott, J. S. Tulenko, R. W. Grimes, P. K. Schelling, and S. R. Phillpot, "Thermal Transport Properties of Uranium Dioxide by Molecular Dynamics Simulations," *J. Nucl. Mater.*, vol. 375, pp. 388-396, 2008.

- [151] J. D. Gale and A. L. Rohl, "The General Utility Lattice Program (GULP)," *Mol. Simul.*, vol. 29, pp. 291-341, 2003.
- [152] J. D. Gale, "GULP: A Computer Program for the Symmetry-Adapted Simulation of Solids," *J. Chem. Soc., Faraday Trans.*, vol. 93, pp. 629-637, 1997.
- [153] T. H. K. Barron, W. T. Berg, and J. A. Morrison, "On the Heat Capacity of Crystalline Magnesium Oxide," *Proceedings of the Royal Society of London Series a-Mathematical and Physical Sciences*, vol. 250, pp. 70-83, 1959.
- [154] S. Lutique, P. Javorsky, R. J. M. Konings, A. C. G. van Genderen, J. C. van Miltenburg, and F. Wastin, "Low Temperature Heat Capacity of Nd₂Zr₂O₇ Pyrochlore," *Journal of Chemical Thermodynamics*, vol. 35, pp. 955-965, 2003.
- [155] M. P. Vandijk, K. J. Devries, and A. J. Burggraaf, "Oxygen Ion and Mixed Conductivity in Compounds with the Fluorite and Pyrochlore Structure," *Solid State Ionics*, vol. 9-10, pp. 913-919, 1983.
- [156] D. H. Chung, "Elastic Moduli of Single Crystal and Polycrystalline MgO," *Philos. Mag.*, vol. 8, pp. 833-841, 1963.
- [157] P. K. Schelling, S. R. Phillpot, and P. Keblinski, "Comparison of Atomic-Level Simulation Methods for Computing Thermal Conductivity," *Physical Review B*, vol. 65, pp. 144306 1-12, 2002.
- [158] D. G. Cahill, S. M. Lee, and T. I. Selinder, "Thermal Conductivity of Kappa-Al₂O₃ and Alpha-Al₂O₃ Wear-Resistant Coatings," *J. Appl. Phys.*, vol. 83, pp. 5783-5786, 1998.
- [159] C. Ronchi, J. P. Ottaviani, C. Degueldre, and R. Calabrese, "Thermophysical Properties of Inert Matrix Fuels for Actinide Transmutation," *J. Nucl. Mater.*, vol. 320, pp. 54-65, 2003.
- [160] J. Wu, X. Wei, N. P. Padture, P. G. Klemens, M. Gell, E. Garcia, P. Miranzo, and M. I. Osendi, "Low-Thermal-Conductivity Rare-Earth Zirconates for Potential Thermal-Barrier-Coating Applications," *J. Am. Ceram. Soc.*, vol. 85, pp. 3031-3035, 2002.
- [161] R. E. Newnham, D. P. Skinner, and L. E. Cross, "Connectivity and Piezoelectric-Pyroelectric Composites," *Mater. Res. Bull.*, vol. 13, pp. 525-536, 1978.
- [162] Samuel M. Allen and E. L. Thomas, *The Structure of Materials*, New York, John Wiley & Sons, Inc., page 377, 1998

- [163] D. G. Cahill, W. K. Ford, K. E. Goodson, G. D. Mahan, A. Majumdar, H. J. Maris, R. Merlin, and S. R. Phillpot, "Nanoscale Thermal Transport," *J. Appl. Phys.*, vol. 93, pp. 793-818, 2003.
- [164] M. A. Angadi, T. Watanabe, A. Bodapati, X. C. Xiao, O. Auciello, J. A. Carlisle, J. A. Eastman, P. Keblinski, P. K. Schelling, and S. R. Phillpot, "Thermal Transport and Grain Boundary Conductance in Ultrananocrystalline Diamond Thin Films," *J. Appl. Phys.*, vol. 99, pp. 114301, 2006.
- [165] K. E. Sickafus, A. C. Larson, N. Yu, M. Nastasi, G. W. Hollenberg, F. A. Garner, and R. C. Bradt, "Cation Disorder in High-Dose, Neutron-Irradiated Spinel," *J. Nucl. Mater.*, vol. 219, pp. 128-134, 1995.
- [166] R. C. Ewing, A. Meldrum, L. M. Wang, and S. X. Wang, "Radiation-Induced Amorphization," *Transformation Processes in Minerals*, vol. 39, pp. 319-361, 2000.
- [167] T. M. Soeda, S., C. Kinoshita, and N. L. Zaluzec, "Cation Disordering in Magnesium Aluminate Spinel Crystals Induced by Electron or Ion Irradiation," *J. Nucl. Mater.*, vol. 283, pp. 952-956, 2000.
- [168] I. N. S. Jackson, Lieberma.Rc, and A. E. Ringwood, "Disproportionation of Spinels to Mixed Oxides - Significance of Cation Configuration and Implications for Mantle," *Earth Planet. Sci. Lett.*, vol. 24, pp. 203-208, 1974.
- [169] R. C. Liebermann, I. Jackson, and A. E. Ringwood, "Elasticity and Phase-Equilibria of Spinel Disproportionation Reactions," *Geophys. J. Roy. Astron. Soc.*, vol. 50, pp. 553-586, 1977.
- [170] R. M. Hazen and H. X. Yang, "Increased Compressibility of Pseudobrookite-Type $MgTi_2O_5$ Caused by Cation Disorder," *Science*, vol. 277, pp. 1965-1967, 1997.
- [171] I. Suzuki and M. Kumazawa, "Anomalous Thermal-Expansion in Spinel $MgAl_2O_4$ - Possibility for a 2nd Order Phase-Transition," *Phys. Chem. Miner.*, vol. 5, pp. 279-284, 1980.
- [172] I. Suzuki, I. Ohno, and O. L. Anderson, "Harmonic and Anharmonic Properties of Spinel $MgAl_2O_4$," *Am. Mineral.*, vol. 85, pp. 304-311, 2000.
- [173] P. Thibaudeau, A. Debernardi, V. T. Phuoc, S. da Rocha, and F. Gervais, "Phonon Anharmonicity in Disordered $MgAl_2O_4$ Spinel," *Phys. Rev. B*, vol. 73, pp. 064305, 2006.
- [174] R. P. Gupta, "Radiation-Induced Cation Disorder in the Spinel $MgAl_2O_4$," *J. Nucl. Mater.*, vol. 358, pp. 35-39, 2006.

- [175] G. B. Andreozzi, F. Princivalle, H. Skogby, and A. D. Giusta, "Cation Ordering and Structural Variations with Temperature in MgAl₂O₄ Spinel: An X-Ray Single-Crystal Study," *Am. Mineral.*, vol. 85, pp. 1164-1171, 2000.
- [176] G. B. Andreozzi, F. Princivalle, H. Skogby, and A. Della Giusta, "Cation Ordering and Structural Variations with Temperature in MgAl₂O₄ Spinel: An X-Ray Single-Crystal Study," *Am. Mineral.*, vol. 85, pp. 1164-1171, 2000.
- [177] G. B. Andreozzi and F. Princivalle, "Kinetics of Cation Ordering in Synthetic MgAl₂O₄ Spinel," *Am. Mineral.*, vol. 87, pp. 838-844, 2002.
- [178] R. F. Mueller, "Model for Order-Disorder Kinetics in Certain Quasi-Binary Crystals of Continuously Variable Composition," *J. Phys. Chem. Solids*, vol. 28, pp. 2239-&, 1967.
- [179] H. S. C. Oneill and A. Navrotsky, "Simple Spinel - Crystallographic Parameters, Cation Radii, Lattice Energies, and Cation Distribution," *American Mineralogist*, vol. 68, pp. 181-194, 1983.
- [180] A. Chartier, T. Yamamoto, K. Yasuda, C. Meis, and S. Matsumura, "Frenkel Pair Accumulation Induced Crystallization of Amorphous MgAl₂O₄," *J. Nucl. Mater.*, vol. 378, pp. 188-192, 2008.
- [181] S. Morooka, S. W. Zhang, T. Nishikawa, and H. Awaji, "Potential Model Parameters for Molecular Dynamics Simulation of Alumina-Magnesia Systems," *J. Ceram. Soc. Jpn.*, vol. 107, pp. 1225-1228, 1999.
- [182] A. Chopelas and A. M. Hofmeister, "Vibrational Spectroscopy of Aluminate Spinel at 1 Atm and of MgAl₂O₄ to over 200-Kbar," *Phys. Chem. Miner.*, vol. 18, pp. 279-293, 1991.
- [183] S. Burghartz and B. Schulz, "Thermophysical Properties of Sapphire, Aln and MgAl₂O₄ Down to 70k," *J. Nucl. Mater.*, vol. 215, pp. 1065-1068, 1994.
- [184] G. Fiquet, P. Richet, and G. Montagnac, "High-Temperature Thermal Expansion of Lime, Periclase, Corundum and Spinel," *Phys. Chem. Miner.*, vol. 27, pp. 103-111, 1999.
- [185] T. Watanabe, S. G. Srivilliputhur, P. K. Schelling, J. S. Tulenko, S. B. Sinnott, and S. R. Phillpot, "Thermal Transport in Off-Stoichiometric Uranium Dioxide by Atomic Level Simulation," *J. Am. Ceram. Soc.*, vol. 92, pp. 850-856, 2009.
- [186] J. F. Bisson, D. Fournier, M. Poulain, O. Lavigne, and R. Mevrel, "Thermal Conductivity of Ytria-Zirconia Single Crystals, Determined with Spatially Resolved Infrared Thermography," *J. Am. Ceram. Soc.*, vol. 83, pp. 1993-1998, 2000.

- [187] B. Leclercq, R. Mevrel, V. Liedtke, and W. Hohenauer, "Thermal Conductivity of Zirconia-Based Ceramics for Thermal Barrier Coating," *Mat-wiss. u. Werkstofftech.*, vol. 34, pp. 406-409, 2003.
- [188] S. Raghavan, H. Wang, R. B. Dinwiddie, W. D. Porter, and M. J. Mayo, "The Effect of Grain Size, Porosity and Yttria Content on the Thermal Conductivity of Nanocrystalline Zirconia," *Scr. Mater.*, vol. 39, pp. 1119-1125, 1998.
- [189] Wikipedia, "Gas Turbine Engine," http://en.wikipedia.org/wiki/Gas_turbine, 2010.
- [190] UTPB, "Brayton Cycle: <http://www.Utpb.Edu/Research-Grants/Ht3r/Description/Components/Brayton-Cycle-Lab/>," 2009.
- [191] W. Beele, G. Marijnissen, and A. v. Lieshout, "The Evolution of Thermal Barrier Coatings - Status and Upcoming Solutions for Today's Key Issues," *Surf. Coat. Technol.*, vol. 121, pp. 61-67, 1999.
- [192] D. R. Clarke and C. G. Levi, "Materials Design for the Next Generation Thermal Barrier Coatings," *Annu. Rev. Mater. Res.*, vol. 33, pp. 383-417, 2003.
- [193] David R. Clarke and S. R. Phillpot, "Thermal Barrier Coating Materials," in *Materials Today*, 8, June 2005, pp. 22-29.
- [194] D. R. Clarke, "Materials Selection Guidelines for Low Thermal Conductivity Thermal Barrier Coatings," *Surf. Coat. Technol.*, vol. 163-164, pp. 67-74, 2003.
- [195] T. Hirata and T. Yokokawa, "Variable-Temperature X-Ray Diffraction of the Ferroelectric Transition in $\text{Bi}_4\text{Ti}_3\text{O}_{12}$," *Solid State Commun.*, vol. 104, pp. 673-677, 1997.
- [196] Q. D. Zhou, B. J. Kennedy, and C. J. Howard, "Structural Studies of the Ferroelectric Phase Transition in $\text{Bi}_4\text{Ti}_3\text{O}_{12}$," *Chem. Mater.*, vol. 15, pp. 5025-5028, 2003.
- [197] E. C. Subbarao, "Ferroelectricity in $\text{Bi}_4\text{Ti}_3\text{O}_{12}$ and Its Solid Solutions," *Phys. Rev.*, vol. 122, pp. 804-808, 1961.
- [198] B. H. Park, B. S. Kang, S. D. Bu, T. W. Noh, J. Lee, and W. Jo, "Lanthanum-Substituted Bismuth Titanate for Use in Non-Volatile Memories," *Nature*, vol. 401, pp. 682-684, 1999.

BIOGRAPHICAL SKETCH

Priyank Shukla was born in Kanpur, UP, India. He received his Integrated Masters of Science in physics from Indian Institute of Technology (commonly known as IIT), Kanpur, India in 2002. It is a 5-year degree program that combines the basic training of both engineering and physical sciences. He came to the United States for his higher studies and joined the graduate program in Physics Department at University of Florida (UF), Gainesville, in Fall 2002. He received his Master of Science in Physics from UF in May 2005. After completion, he joined the doctoral degree under Prof. Simon R. Phillpot at UF, Gainesville. He received his Ph.D. in materials science and engineering from the University of Florida in the summer of 2010.